

12

HR-81-269-16-59

AD A113845

## ALKALI HALIDE FLIR LENS DEVELOPMENT

R.H. Anderson, Principal Investigator (612/887-4533)  
R.J. Stokes, Department Manager (612/887-4525)  
T.J. Moravec, Project Scientist (612/887-4309)  
J.W. Lin, Project Scientist (612/887-4463)  
F.M. Schmit, Project Scientist (612/887-4435)  
J.F. Ready, Group Leader (612/887-4430)  
D.K. Greenlaw, Consultant (612/378-5719)  
D. Stoltzmann, Consultant (612/378-5255)

Honeywell Inc.  
Corporate Physical Sciences Center  
10701 Lyndale Ave. So.  
Bloomington, MN 55420

### Final Technical Report

1 October 1979 to 31 July 1981

Contract No. MDA 903-80-C-0098

Effective Date 11 December 1979  
Expiration Date 31 July 1981

Research was sponsored by  
the Defense Advanced Research Projects Agency  
under DARPA Order No. 3833,  
Contract No. MDA 903-80-C-0098  
monitored by USAECOM Night Vision and  
Electro Optics Laboratory

DTIC  
SELECTED  
APR 21 1982  
E

The views and conclusions contained in this document are those of the authors and should not be interpreted as necessarily representing the official policies, either expressed or implied, of the Defense Advanced Research Projects Agency or the U.S. Government.

This document has been approved  
for public release and sale; its  
distribution is unlimited.

82 04 21 051

DTIC FILE COPY

UNCLASSIFIED

SECURITY CLASSIFICATION OF THIS PAGE (WHEN DATA ENTERED)

REPORT DOCUMENTATION PAGE		READ INSTRUCTIONS BEFORE COMPLETING FORM
1. REPORT NUMBER HR-81-269-16-59	2. GOV'T ACCESSION NUMBER AD-A113 845	3. RECIPIENT'S CATALOG NUMBER
4. TITLE (AND SUBTITLE)  ALKALI HALIDE FLIR LENS DEVELOPMENT		5. TYPE OF REPORT/PERIOD COVERED FINAL TECHNICAL 1 October 1979 to 31 July 1981
		6. PERFORMING ORG. REPORT NUMBER 47849
7. AUTHOR(S) R. W. Anderson, R. J. Stokes, T. J. Moravec, J. W. Lin, F. M. Schmit, J. F. Ready, D. K. Greenlaw, and D. Stoltzmann		8. CONTRACT OR GRANT NUMBER(S) MDA-903-80-C-0098
9. PERFORMING ORGANIZATIONS NAME/ADDRESS Honeywell Corporate Physical Sciences Center 10701 Lyndale Avenue S. Bloomington, MN 55420		10. PROGRAM ELEMENT PROJECT, TASK AREA & WORK UNIT NUMBERS
11. CONTROLLING OFFICE NAME/ADDRESS Defense Advanced Research Projects Agency 1400 Wilson Blvd. Arlington, VA 22209		12. REPORT DATE October 1980
14. MONITORING AGENCY NAME/ADDRESS (IF DIFFERENT FROM CONT. OFF.) USAECOM Night Vision and Electro-Optics Laboratory Fort Belvoir, VA 22060		13. NUMBER OF PAGES
		15. SECURITY CLASSIFICATION (OF THIS REPORT) UNCLASSIFIED
		15a. DECLASSIFICATION DOWNGRADING SCHEDULE
16. DISTRIBUTION STATEMENT (OF THIS REPORT)  APPROVED FOR PUBLIC RELEASE; DISTRIBUTION UNLIMITED		
17. DISTRIBUTION STATEMENT (OF THE ABSTRACT ENTERED IN BLOCK 20, IF DIFFERENT FROM REPORT)		
18. SUPPLEMENTARY NOTES		
19. KEY WORDS (CONTINUE ON REVERSE SIDE IF NECESSARY AND IDENTIFY BY BLOCK NUMBER)		
Infrared Alkali halides Forging Coatings	FLIR Potassium Bromide Potassium Chloride Plasma Polymerization Polyethane	Polyethylene KRS-5 Lens Forging Interferometry
20. ABSTRACT (CONTINUE ON REVERSE SIDE IF NECESSARY AND IDENTIFY BY BLOCK NUMBER)		
<p>(U) This report describes development of materials and processes for environmental protection of alkali halide lenses. The alkali halide lenses are fabricated by direct hot forging, which yields a finished lens without need for polishing. These lenses are intended for potential application in FLIR thermal imaging systems. The lenses require coatings to protect them against water vapor in the atmosphere. The main emphasis in this report has been development of protective coatings for potassium bromide lenses. The most favorable coating developed consisted of a multilayer structure of arsenic triselenide, polyethylene and plasma - polymerized ethanes. This coating provides antireflective properties and minimal protection against water vapor. It does</p>		

HD-168 REV 11/74

UNCLASSIFIED

SECURITY CLASSIFICATION OF THIS PAGE (WHEN DATA ENTERED)

20. Abstract (U) not meet the severe humidity specifications of Mil-Std-810B. In addition forging methods to fabricate lenses from KRS-5 were investigated. Optical testing methods were developed to determine the performance of the forged lenses.

Accession For	
NTIS GRA&I	<input checked="checked" type="checkbox"/>
DTIC TAB	<input type="checkbox"/>
Unannounced	<input type="checkbox"/>
Justification	
By	
Distribution/	
Availability Codes	
Dist	Avail and/or Special
A	



UNCLASSIFIED

SECURITY CLASSIFICATION OF THIS PAGE (WHEN DATA ENTERED)

## Summary

This program deals with the development of halide materials for potential application as optical elements (lenses) in thermal imaging systems. The lenses are produced by hot press forging of starting single crystals. The lenses are forged between curved dies, and are produced with a final shape and surface figure without the need for polishing. Thus, they can provide low-cost optics for use in infrared imaging systems.

Halide materials are moisture sensitive and are degraded by exposure to water vapor. Developing protective coatings is of prime importance if halide materials are to become practical optical elements and achieve wide use. The main emphasis in this contract was the development of materials and processes for moisture protection of KBr lenses which had been developed previously. The KBr lenses were intended to serve as a replacement for the ZnSe color corrector lens in the imager module of the common modular FLIR.

Organic materials such as plasma-polymerized ethane had been identified previously as promising candidates for moisture protection. During this work, measurement of the properties of materials suitable for moisture protection of KBr was continued. The rate of moisture penetration through ten specified coating materials was determined, and a combined antireflective and moisture protective coating, based on a three-layer structure of arsenic selenide, polyethylene and plasma-polymerized ethane was developed. The procedure for deposition of the coating layers was optimized. This coating structure provides minimal moisture protection, but does not meet the specifications of the relevant severe humidity test of Mil-Std-810B.

It is necessary to evaluate the optical characteristics of the forged lenses. In this program, test procedures for KBr lens evaluation including double-pass two-wavelength holography (TWH) and lateral shearing interferometry were developed. Forged KBr lenses were evaluated using lateral shearing interferometry, and the results were correlated with the modulation transfer function (MTF) of the imager module with the KBr lenses in place of the ZnSe lens. Results indicate that a correlation exists and that lateral shearing interferometry may be suitable for evaluation of forged optical elements in production.

In addition, procedure were investigated for forging KRS-5 (thallium bromoiodide). Aspheric KRS-5 lenses could potentially serve as replacement for expensive germanium lenses. Procedures for forging aspheric KRS-5 lenses were established, but the lenses did not meet the MTF specifications of the common modular FLIR.



## Table of Contents

Section	Page
1 INTRODUCTION	1
Background	1
Contract Tasks	3
2 DEVELOPMENT OF MATERIALS AND PROCESSES FOR PROTECTIVE COATINGS	6
Polyethane	6
Polyethylene	10
Acrylic Acid-Ethylene Copolymer	11
Poly(Vinylidene Chloride)	11
Humidity Screening	12
Plasma-Polymerized Ethane	12
TiI/PPE Coating	14
PAA/TiI/PPE Coating	14
As <sub>2</sub> Se <sub>3</sub> /PPE	15
Ge/PPE and Ge/TiI/PPE	15
As <sub>2</sub> Se <sub>3</sub> /PE/PPE	17
Other Coatings	25
Conclusion	25
3 SURFACE PREPARATION	26
Surface Cleaning	26
Ion Barriers	27
4 SURFACE PASSIVATION	28
Surfactants	28
Complex Formation	29
Polar Organic Compounds	29
Surface-Active Macromolecules	29
Conclusion	29
5 MOISTURE PERMEABILITY MEASUREMENT	31
Film Preparation	31
Permeability Measurement	32
6 CHARACTERIZATION OF COATINGS	36
Infrared Transmission Measurement	36
Surface Texture Analysis	40
Surface Composition Analysis	40
Kinetics of Moisture Attack	44
Heat of Moisture-Halide Interaction	49

## Table of Contents (Continued)

Section		Page
7	DEVELOPMENT OF COMBINED PROTECTIVE AND ANTI-REFLECTIVE COATINGS: EXPLORATION AND DEVELOPMENT	50
8	ADVANCED TESTING METHODS	52
	Testing Lenses in Transmission	52
	Double-Pass Transmission Using Two-Wavelength Holography (TWH) ;	53
	Lateral Shearing Interferometer	54
	Conclusions	60
9	OPTICAL TESTING	61
	Correlation Between MTF and Interferometry	61
10	DEVELOPMENT OF PROTECTIVE COATINGS FOR KBr	70
11	DEVELOPMENT OF COMBINED PROTECTIVE AND ANTIREFLECTIVE COATINGS: MEASUREMENT	76
12	ENVIRONMENTAL TESTING ON COATED KBr	80
	Sample Preparation	80
	Humidity Testing	81
	Secure Humidity Testing	82
	Environmental Testing — Fungus	87
	Summary of Environmental Test Results	88
13	KRS-5 LENS DEVELOPMENT	89
	Background	89
	Technical Approach	90
	Optical Centering	93
	Evaluation of the Aspheric Lens	94
	Aspheric Forging Die	115
	Improved Replication	118
	Forging Accomplishments	119
14	CONCLUSIONS AND RECOMMENDATIONS	120
	Accomplishments	120
	Recommendations for Future Work	121

## Table of Contents (Concluded)

Section	Page
REFERENCES	122
APPENDIX A — ION BARRIER MATERIALS	123
APPENDIX B — ANTIREFLECTIVE COATING	128
APPENDIX C — FUNGUS TEST	130
APPENDIX D — PAPERS RESULTING FROM WORK ON LENS DEVELOPMENT	134
APPENDIX E — ASPHERIC PROFILE MEASUREMENTS	136

## Section 1 Introduction

### BACKGROUND

The increasing application of optics to military systems has created a need for new materials and/or component fabrication approaches that can best produce optical elements having unusual performance characteristics. In passive systems, such as FLIR, a need exists for optical systems capable of diffraction-limited performance that are compact, lightweight and have potential for low cost production. These requirements can be more readily met by using aspheric optical elements. Because of the strategic value of the systems, it is highly desirable to use materials available in plentiful supply domestically to fabricate such components.

This program has dealt with a new approach to the fabrication of optical components by high-temperature forging between polished dies to obtain a finished element ready for coating, and possessing the shape and surface finish of the die used for forging. The combination of halide materials and this approach to optical fabrication is ideally suited to the development of lens elements for FLIR optical systems because:

- The outstanding transparency ranges of halides makes them excellent candidates for optical elements in advanced imaging systems involving multispectral capabilities.
- The focal length of halide lenses is nearly temperature independent because of the excellent compensation of thermal expansion and change in refractive index. The small residual temperature dependence is of a sign opposite that of germanium and should therefore help make the optical system's performance temperature independent.
- The forging approach is ideally suited for fabricating aspheric elements. This can result in a significant reduction in the number of lenses required to achieve a given level of optical performance.
- The halide raw materials used in the process are readily available in this country and are basically inexpensive; by comparison, germanium comes partly from foreign sources and is relatively expensive.
- The dispersion of the refractive index of KBr is an excellent match to that of zinc selenide, a commonly used but expensive color corrector element in FLIR optics. This good match should make for ready replacement of such elements at considerable savings with minimal redesign costs.

The approach to developing this new method of optical element fabrication is based on experience in developing alkali halide forging techniques: first, for the strengthening of those materials for use in high-power infrared laser windows, and more recently in developing methods for producing finished optical surfaces. The latter approach has been pursued under both internal contractor efforts and DARPA sponsored programs at the contractor's Corporate Physical Sciences Center where this approach was developed.

In 1976, as part of an ongoing DARPA program to develop HEL windows, a significant breakthrough was made in the ability to reproduce the surface finish of the dies used in the forging operation. A process was developed in which the forging of the halide optical element is performed in a chamber pressurized with helium to several thousand pounds per square inch. The pressurized helium provides: a hoop stress on the deforming halide crystal preventing the formation of peripheral cracks; heat transfer between the walls of the heated pressure vessel and the crystal; and lubrication between the crystal and the die. It should be noted that employing alkali halides in optical systems for field use has been impracticable in the past because of their very low strength in single-crystal form, the difficulty of polishing these soft materials, and their susceptibility to moisture attack. These handicaps have been partly removed by increasing the strength of the forged polycrystalline material—and by forging the finished lens elements between polished die surfaces. The necessity of providing environmental protection, however, has continued to be a critical issue in the practical utilization of halide optical elements.

To evaluate the quality of alkali halide lenses designed to replace existing materials, the color corrector lens in the imager module of the common modular FLIR was chosen as a test vehicle. The imager module contains three elements—two Ge lenses and one ZnSe color corrector lens. Because the dispersion of KBr is close to that of ZnSe, a switch in material from one to the other could be made without any changes in the other two elements. Under contract from DARPA in 1977<sup>(1)</sup>, a KBr lens of suitable shape was designed, and work begun to develop the forged KBr lens.

The goal of this DARPA program was to demonstrate that alkali halide lenses of adequate quality could be fabricated in the laboratory by isostatic forging between two suitably finished dies. Emphasis was on understanding the materials and process parameters that affect the surface figure and optical performance of these halide lenses intended for use in FLIR optics.

The original 12-month program<sup>(1)</sup> produced the following significant results in four areas:

- Materials and Processing Studies—:
  - The capabilities of the isostatic forging process to fabricate a KBr lens for substitution of the ZnSe color corrector in the IR imager of the FLIR system were demonstrated.
  - Several forging parameters were identified to gain an understanding of their effects on the optical performance of the finished lens.
  - New approaches to obtaining the required lens shape and optical figures, including iterations with modified die shapes, the feasibility of using diamond-turned dies, pressure bending to improve the lens optical figure, and reproducibility were introduced and demonstrated.



- Lens Design—:
  - Selected FLIR optical trains were successfully redesigned to incorporate both spheric and aspheric halide elements in the NVL common modular FLIR including the narrow-angle mode afocal telescope and the IR imager.
- For Optical Characterization—:
  - Development of a state-of-the-art holographic and shearing interferometer was completed under contractor internal funding to routinely characterize the forged KBr lens interferometrically.
  - Procedures for aspheric testing were formulated.
  - The optical performance of an IR imager using a forged KBr lens in place of the ZnSe lens by means of MTF measurement was evaluated.
- AR Coating Studies—:
  - Coatings on forged KBr lenses were designed and fabricated to provide anti-reflective (AR) characteristics at  $10\mu\text{m}$  and minimal protection against humidity and abrasion.

Following this work, a Manufacturing Methods and Technology (MM&T) contract to produce hot forged alkali halide lenses was awarded to the contractor's Ceramics Center. The goal of this effort was to reduce the costs of hot forging of KBr into finished optical elements, and to optimize procedures for volume production of the lenses.

### CONTRACT TASKS

The present contract continues research tasks needed to exploit the technology of forged optics. The research described in this report emphasizes three main areas:

- Development of environmental protective coatings for KBr. This is perhaps the most crucial of the tasks. Suitable moisture protective coatings must be available if forged halide optical elements are to achieve broad practical use. The coating development is thus the main thrust of the current program. The program has emphasized selection of coating materials and development of optimized methods of coating deposition.
- Optical testing. The program also includes tasks involving optical testing, such as developing advanced optical testing methods, and developing testing procedures compatible with production testing. Such testing is needed to characterize the forged optical elements.
- Development of methods for forging of KRS-5. KRS-5, as a high-index material, could be considered as a substitute for germanium lenses in a FLIR system.

During the course of the work, perceptions changed about the potential role of forged halide optics in infrared optical systems. It now appears that forged halide optics will not be qualified and brought into procurement cycles until later than was believed at the beginning of the contract period. In accordance with these changing views, the list of tasks to be performed was modified twice during the contract period, according to agreement with the government. The final list of contract tasks reflects a material-oriented effort emphasizing development of coating materials and processes and deemphasizing tasks aimed at early qualification of halide materials for infrared optics. The final modified list of tasks is given below. The remaining sections of the report describe the work done on each of these tasks.

Portions of this work have been reported earlier in a semiannual report.<sup>(2)</sup> In this report, for completeness, brief descriptions of work already discussed in the semiannual report are included. The main emphasis is on work performed after the semiannual report.

- **Task 1. Development of Materials and Processes for Protective Coatings** — Develop organic coating materials for environmental protection of alkali halides and optimize the coating procedures and process variables so as to achieve uniformity, good adhesion and high mechanical strength. The coating materials to be investigated shall include:
  - 1. Polyethane
  - 2. Polyethylene
  - 3. Acrylic acid-ethylene copolymer
  - 4. Poly (vinylidene chloride)
- **Task 2. Surface Preparation** — Develop and evaluate cleaning procedures, including stripping procedures, necessary to produce clean, dust-free surfaces, suitable for deposition of coatings.
- **Task 3. Surface Passivation** — Develop an effective passivation process by surface treatment and/or the addition of materials, such as:
  - 1. Surfactants
  - 2. Complex formation
  - 3. Polar organic compounds and polymers
  - 4. Surface-active macromolecules
- **Task 4. Moisture Permeability Measurement** — Determine moisture permeability for 8 selected materials: polyethane, polyethylene, acrylic acid-ethylene co-polymer, poly (vinylidene chloride), thallium iodide (TII), lead fluoride ( $\text{PbF}_2$ ), zinc sulfide ( $\text{ZnS}$ ), and arsenic selenide ( $\text{As}_2\text{Se}_3$ ) by depositing different thicknesses of each material on a permeability measurement cup and determining the weight loss of a water solution at different temperatures.
- **Task 5. Characterization of Coatings** — Perform the following experiments and studies on the coating materials:

1. Measure infrared transmission—Fourier transform spectrometer (FTS)
  2. Surface texture analysis—Scanning electron microscopy (SEM)
  3. Surface composition analysis—X-ray photoelectron spectroscopy (ESCA) and Auger spectroscopy
  4. Kinetics of moisture attack—Thermogravimetric analysis (TGA)
  5. Heat of moisture-halide interaction—Differential scanning calorimetry (DSC)
- **Task 6. Development of Combined Protective and Antireflective Coatings** — Explore and develop an advanced total coating system for alkali halides for FLIR applications to perform the functions of both environmental protection and reduction of reflection loss.
  - **Task 7. Advanced Testing Methods** — Develop advanced testing methods such as two-wavelength holographic interferometry in single- or double-pass transmission configurations and lateral shearing in single-pass transmission.
  - **Task 8. Optical Testing** — Perform optical tests on forged lenses using the Honeywell-Tropel holographic interferometer. Develop correlations between results of interferometric testing and performance of the lens as an optical element.
  - **Task 9. Development of Protective Coatings for KBr.** — Optimize coating procedures for the coating systems ( $\text{As}_2\text{Se}_3$ /polyethylene (PE)/plasma polymerized ethane (PPE) and Ge/Ti/PE/PPE to produce defect-free coatings and to demonstrate the maximum capabilities of these systems for the protection of polycrystalline KBr.
  - **Task 10. Development of Combined Protective and Antireflective Coatings** — By varying the thicknesses of the layers in the coating systems and measuring the IR transmission, develop a coating which has both protective and antireflection functions for KBr.
  - **Task 11. Environmental Testing on Coated KBr** — Perform environmental tests on coated polycrystalline KBr, including tests for resistance to humidity, severe humidity and fungus, according to the methods of Mil-Std-810B. Determine the extent to which the coating systems can provide environmental protection for KBr.
  - **Task 12. KRS-5 Lens Development** — Improve the reproducibility of forged KRS-5 lenses by developing unconstrained forging procedures to replicate the die surface closely, using spherical dies.

## **Section 2**

### **Development of Materials and Processes for Protective Coatings**

**Task: Develop organic coating materials for environmental protection of alkali halides and optimize the coating procedures and process variables so as to achieve uniformity, good adhesion and high mechanical strength. The coating materials to be investigated shall include:**

- 1. Polyethane**
- 2. Polyethylene**
- 3. Acrylic acid-ethylene copolymer**
- 4. Poly (vinylidene chloride)**

The main emphasis in this task was to determine suitable protective organic polymer materials and to develop processes for depositing films of these materials on alkali halide substrates.

Previous work<sup>(1),(3)</sup>, had examined the potential applicability of inorganic materials for protection of alkali halides with the conclusion that it was unlikely that a protective coating based on inorganic materials alone could provide moisture protection at the required level. Accordingly, emphasis shifted toward investigation of the moisture protection afforded by thin layers of organic materials.

Because organic materials often have absorption in the 8 to 12 $\mu$ m region, the absorption spectra are of paramount importance. Earlier work<sup>(3)</sup> surveyed hundreds of polymer IR spectra. A number of polymers were selected for further investigation to determine their applicability as a protective coating for alkali halide crystals. IR spectra of the candidate polymers were studied. Spectroscopic absorption characteristics were extracted from these spectra. It was clear from this evaluation that plasma-polymerized ethane, plasma-polymerized ethylene and commercial polyethylene are excellent candidate materials for 8 to 12 $\mu$ m application, the operating range of present day FLIR systems. Other polymers such as acrylic acid-ethylene copolymer, and polyvinylidene chloride may be useful for other wavelengths or in very thin form such that the absorption in the 8 to 12 $\mu$ m region is reduced to an acceptable level.

This section describes the work done to develop these materials as components of an organic-based moisture protective coating.

#### **POLYETHANE**

Deposition of plasma polymerized ethane (PPE) was begun before the present contract period<sup>(3)</sup>, and PPE was identified as a promising candidate material for moisture protection of alkali halides. The following briefly reviews some of the earlier results.

Plasma-polymerized ethane polymer has low absorption except in a narrow band, i.e., 3.2 to 3.5  $\mu\text{m}$ , and two peaks, i.e., 6.9 and 7.4  $\mu\text{m}$ . The narrow band is attributable to C-H bond stretching. The two peaks are identified as C-H asymmetrical bending and C-H symmetrical bending, respectively. In addition, plasma-polymerized ethane has good adhesion to halide substrates and is highly hydrophobic. The early work<sup>(3)</sup> used a barrel reactor without electrodes. This reactor was also used in the early stages of the present contract.

This reactor uses an inductively coupled electrodeless plasma system (Figure 1). The rf power supply operates at 13.56 MHz and provides a variable output power from 0 to 350 watts. The impedance match between the rf generator and load is optimized by an automatic turning mechanism which maintains the reflected power at a minimum.

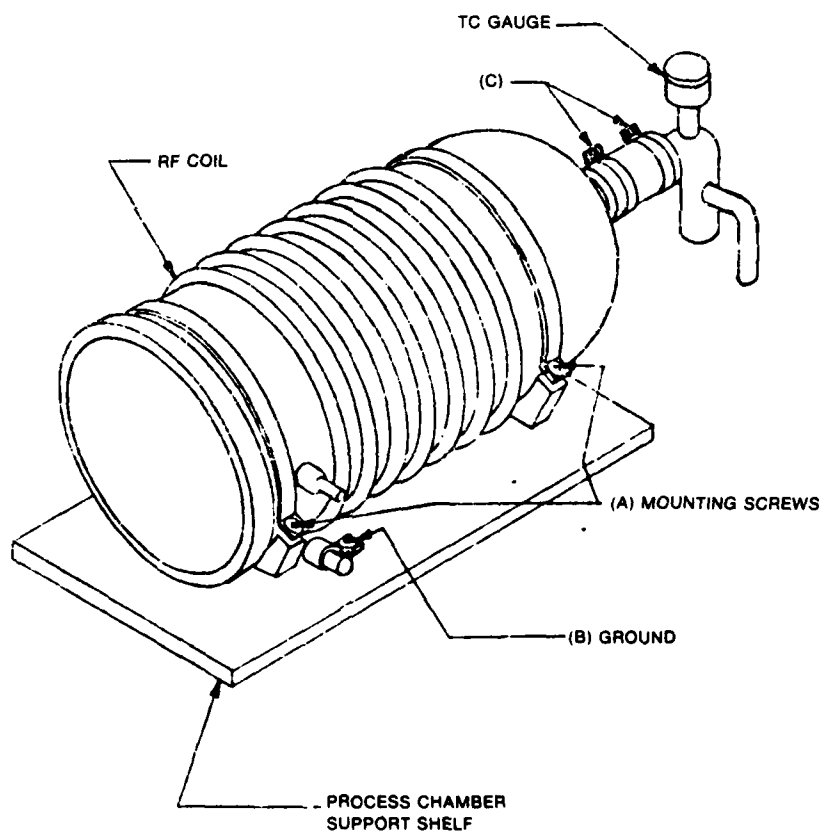


Figure 1. Schematic diagram of barrel reactor for deposition of plasma-polymerized ethane.



Prior to introduction of the monomer, the reaction chamber is pumped down to  $10^{-2}$  torr with a mechanical pump. A needle valve on the inlet is used to control the pressure of the monomer as measured by a flowmeter. To allow the system to attain a steady pressure, the plasma chamber is purged for 10 minutes before initiation of the plasma.

Film quality varied from oily to powdery, with hard dense coatings obtained at optimum conditions. Film quality obtained using various power-pressure combinations at a flow rate of 10 cc/min is shown in Figure 2.

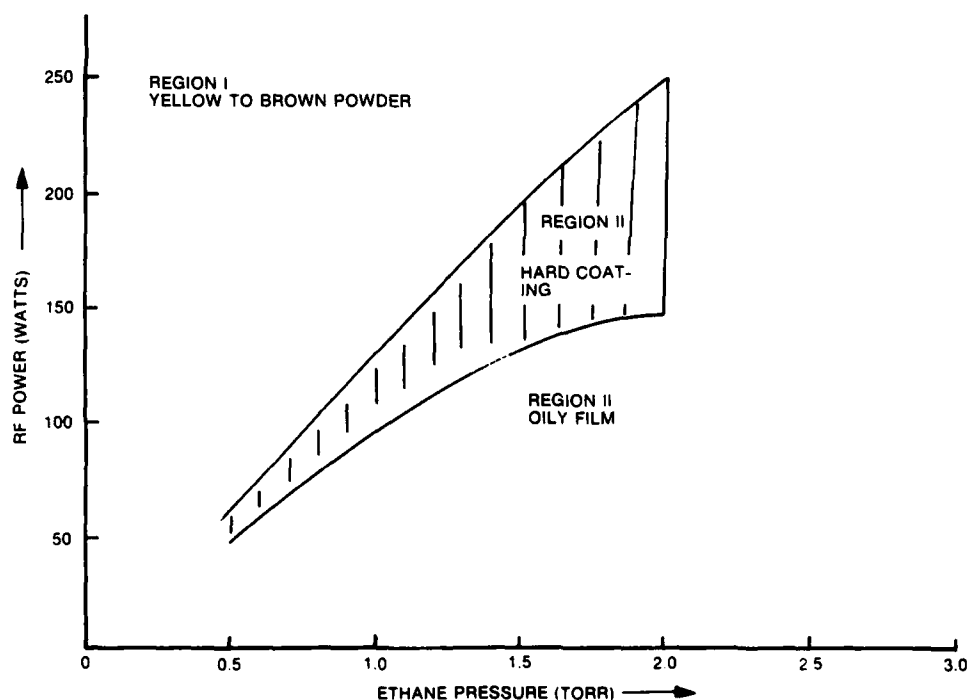


Figure 2. Results of plasma-polymerization of ethane for varying conditions of rf power and ethane pressure.

Chemically pure ethane used as monomer for the film deposition was obtained from the Matheson Gas Co. and was used without additional purification. Commercial-grade oxygen for system plasma cleaning and hydrogen obtained from Air Products Corp. were used as received.

The PE coating was improved by changing to a parallel-plate system with water-cooled electrodes (Figure 3). Deposition of films in this system can be carried out at a reduced temperature with higher growth rate and less power. Hard and dense films with good uniformity are obtained reproducibly.

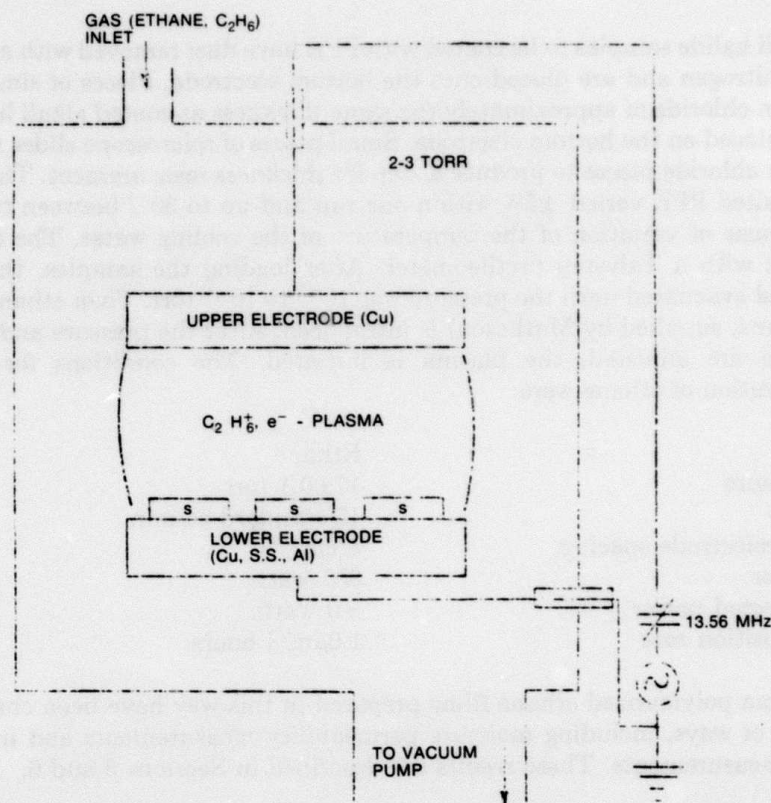


Figure 3. Schematic diagram of parallel-plate reactor for deposition of plasma-polymerized ethane.

In the initial configuration, the electrodes were of 6-inch diameter. Although film quality in the center of the deposition region was good, the film thickness varied over a horizontal distance of a few inches. To eliminate this nonuniformity, the system was again modified, and 15-inch-diameter electrodes were installed. (This second modification was carried out using contractor funds).

Both 15-inch copper-lined aluminum electrodes are water-cooled. The top electrode can be raised or lowered to adjust the interelectrode spacing. The ethane is introduced into the chamber through a gas manifold which branches into five tubes of the same length, i.e., with the same impedance (resistance). Therefore each tube provides the same gas flow rate. The outlets of these five tubes are located close to the chamber bottom, and are approximately 72 degrees apart. The gas, distributed uniformly, passes between the wall of the chamber and the bottom electrode and is directed by a baffle into the interelectrode space where the flow discharge and the deposition occur. The unused gas and gaseous products are pumped out through a 4.5-inch hole in the bottom electrode and a 5-inch glass tube by the diffusion pump.

The alkali halide samples to be coated with PPE have dust removed with a stream of dry gaseous nitrogen and are placed onto the bottom electrode. Pieces of single-crystalline potassium chloride of approximately the same thickness as coated alkali halide samples are also placed on the bottom electrode. Small pieces of microscope slides are put on the potassium chloride pieces to produce a step for thickness measurement. The thickness of the deposited PPE varied  $\pm 5\%$  within one run and up to 30% between two successive runs because of variation of the temperature of the cooling water. The thickness was measured with a Talystep profileometer. After loading the samples, the chamber is closed and evacuated until the pressure was  $10^{-5}$  to  $10^{-6}$  torr. Then ethane (chemically pure ethane, supplied by Matheson) is introduced. After the pressure and the flow rate of ethane are adjusted, the plasma is initiated. The conditions for this plasma polymerization of ethane were:

Gas	Ethane
Pressure	$17 \pm 0.1$ torr
Flow	15 standard cc/min
Interelectrode spacing	4 cm
Power	350 watts
Reflected power	$\sim 0$ watts
Deposition rate	$1.0 \mu\text{m}/3$ hours

The plasma polymerized ethane films prepared in this way have been characterized in a variety of ways, including moisture permeability measurements and infrared transmission measurements. These results are described in Sections 5 and 6.

## POLYETHYLENE

It was determined earlier<sup>(3)</sup> that polyethylene (PE) has no significant absorption in the wave length range of 8 to  $12 \mu\text{m}$ . It is a highly crystalline material with very low moisture permeability. These properties make it a suitable candidate for protective coating. Also it has a refractive index of 1.5, comparable to that of PPE, and is highly compatible with a PPE coating. Thus, polyethylene coatings have been used together with PPE.

To deposit PE in thin layers requires that PE be dissolved in some liquid. A suitable substrate is then covered with this liquid combination or solution. During evaporation a film is deposited on the substrate surface. Because of the inertness of PE, the only suitable solvent appears to be heated xylene. If xylene is heated to  $80^\circ\text{C}$  or above, it provides limited solubility for PE. For coating, the substrate can be immersed in the heated xylene and PE solution and slowly withdrawn (dip coating) providing a thin film. Or the substrate can be withdrawn and rapidly rotated to remove the excess solution, leaving a thin film. This later method is called spin coating and has been found to produce a more adherent coating than dip coating. Both methods have the potential of coating optical shapes. Spin coating appears to offer the potential of building up the PE thickness by multiple dipping and spinning steps. In dip coating, redissolution of the applied PE occurs, probably because of the longer contact time with the solution during withdrawal.

The boiling point of xylene is 135°C. Since PE does not dissolve in xylene at temperatures below 80°C, the coating operation must take place in this temperature interval (80° to 135°C). It was determined empirically that the deposited PE is cloudy below 95°C; consequently, all coating is done at 100°C or slightly above. At 100°C the vapor pressure of xylene is very high, and rapid loss of xylene from the solution is a continuous problem. To minimize this loss, the vessel which holds the heated solution is covered except during those times when depositions are made. The system used for the depositions is operated within a fume hood to minimize xylene exposure by the operator.

In the initial experiments on PE, a dip coating technique was used. Room-temperature substrates are suspended above the solution for 30 minutes to preheat them. Then the substrate is dipped into the solution and kept immersed for 15 minutes to ensure complete wetting of the surface. Then the substrate is pulled out of the solution at a controlled rate. The pulling rate determines the thickness of the coating. Finally the samples are annealed in an oven (typically at 115°C for 2 hours). The resulting PE is highly dense and crystalline. The development of such crystalline PE coatings provided a definite advance in capability for moisture protection of alkali halides. This is described later in this section. The later improvement of the deposition of PE by spin coating techniques is discussed in Section 10.

Other properties of the polyethylene have been measured, including moisture permeability and infrared transmission. These measurements are described in Sections 5 and 6.

#### **ACRYLIC ACID-ETHYLENE COPOLYMER**

Acrylic acid-ethylene copolymer had been identified in an effort to explore alternate materials for protective coatings. Films were produced by simple dip coating of substrates in a solvent containing acrylic acid-ethylene. Infrared absorption spectra were obtained from a sample with thickness around 0.5 $\mu$ m. An absorption band was observed in the 9 $\mu$ m region. Because of this absorption, relatively little effort was devoted to development of this material. Efforts were concentrated on the materials PE and PPE, which exhibit better transmission in the wavelength region of interest.

#### **POLY (VINYLIDENE CHLORIDE)**

Plasma polymerization of vinylidene chloride monomer was carried out in the same reactor in which plasma polymerization of ethane was studied. Poly (vinylidene chloride) also showed absorption lines in the 8 to 9 $\mu$ m wavelength range and was judged to be unsuitable for further development.

## HUMIDITY SCREENING

Candidate materials for humidity resistance were screened by a series of humidity exposures. This method evaluated numerous coating systems as potential protective coatings for alkali halide FLIR optical elements. The tests involved exposure of coated KCl substrates to high temperature at high relative humidity and evaluation of the effects.

The samples used in these humidity tests consisted of a coating deposited on one face of a 1-inch-diameter KCl substrate. If these samples are subjected to heat and humidity without further protection, two problems occur: First, damage originating in an uncoated area may spread to the coated area (e.g., crystal formation at the edge of the coating may pry up the coating and cause damage in the area to be observed). Thus the extent of the damage may be a poor indicator of the coating's actual effectiveness. Second, if one looks at a sample through a microscope or a camera lens, the depth of field is such that both faces of the substrate are visible simultaneously. This creates confusion as to which face is actually damaged. To solve these problems, the uncoated areas of the samples are sealed and prepared in the following manner.

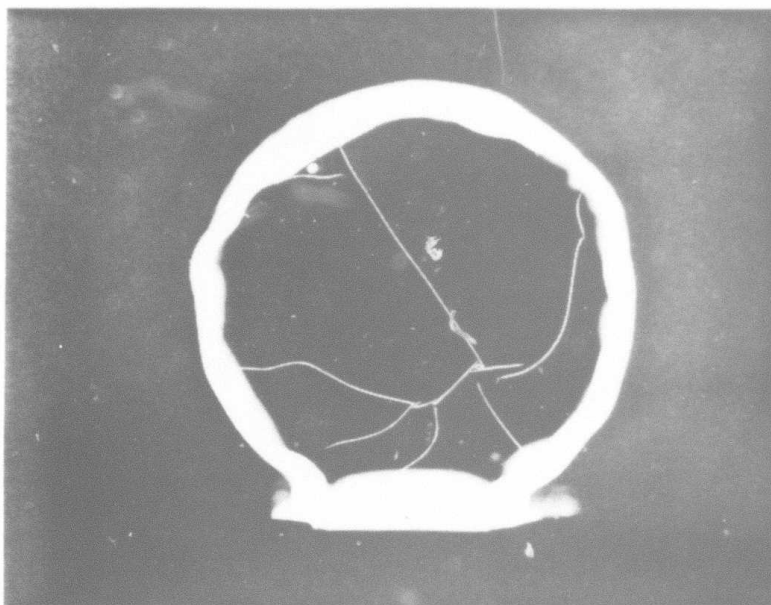
A strip of paraffin film is stretched around the circumference of the sample, so that one edge of the strip is flush with the uncoated face and the other edge hangs out beyond the coated face. After the samples have been masked in this manner, they are placed coated-side down on a sheet of paper so that the sample is supported by the overhanging paraffin film and contact between coating and paper is avoided. Then the (exposed) uncoated face is sprayed with black acrylic paint to make defects in the uncoated side invisible when viewed from the coated side and to enhance the visibility of the defects on the coated side by providing a contrasting background. After the paint is dry, the paraffin is removed, leaving the substrate with one face painted black, the other coated, and the edge clean. Then the edge and painted face are spread with low-vapor pressure resin sealant (Torr-Seal), to prevent moist air from contacting the uncoated areas. Before the sealant dries, a small piece of glass is attached to the edge to allow the sample to stand vertically during testing. Also, an identification number is written on the edge. Then the sealant is cured at 70 to 80°C for 15 minutes. Only the coated area is exposed to the humid air. More accurate evaluations of a coating's actual effectiveness are possible.

### Plasma-Polymerized Ethane

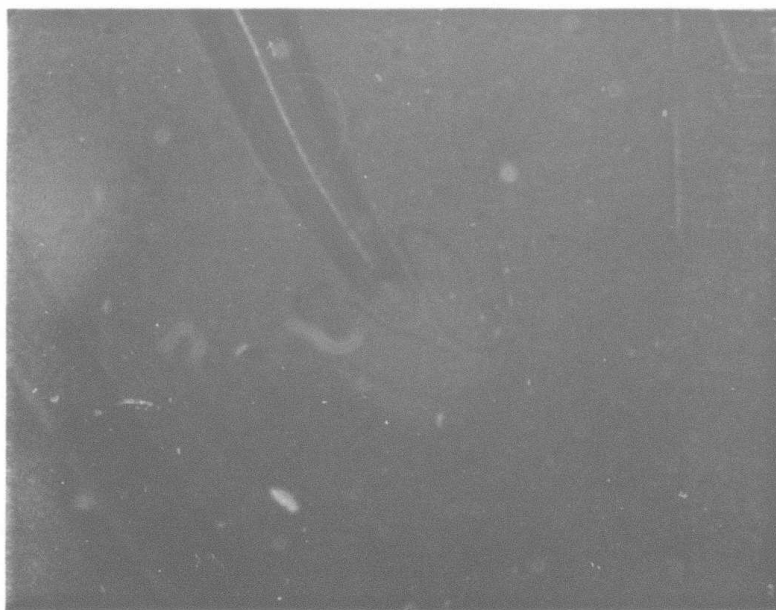
A typical failure in ethane polymer (PPE) coating is wrinkling of the coating. This problem appears to result from the absorption of water vapor by coating and substrate. This separates the coating and substrate and causes the coating to swell. A typical film wrinkled by this mechanism is shown in Figure 4. With early PPE coatings, damage normally occurred after 5 hours at 40°C and 81% relative humidity. As the testing temperature was raised, the damage occurred more rapidly.

Substantial progress was made with the later ethane polymer coatings. Figure 5 shows an ethane polymer coating that withstood 4 hours at 50°C and 6 hours at 70°C, both at 81% relative humidity (RH). The favorable results are related to two factors:





(a)



(b)

Figure 4. Ethane polymer coated on KCl substrate damaged by moisture; (a) 2.5X (b) 100X.

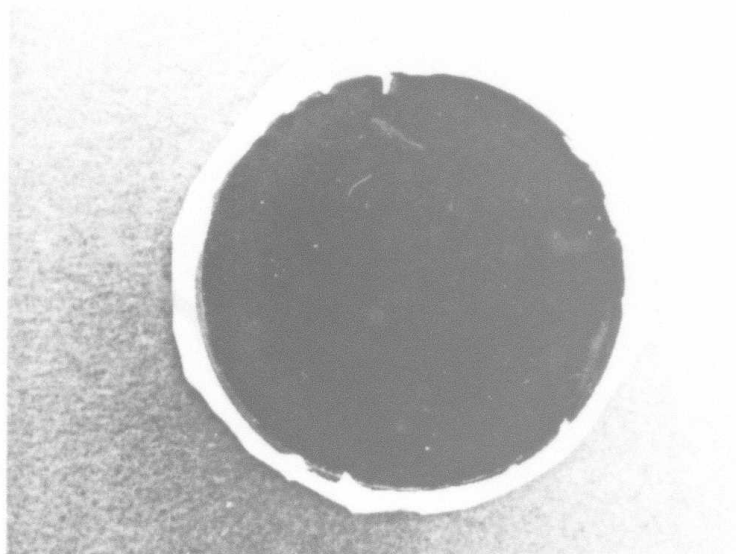


Figure 5. Improved ethane polymer coating. It withstood a humidity test at 81% relative humidity for 4 hours at 50°C and 6 hours at 70°C.

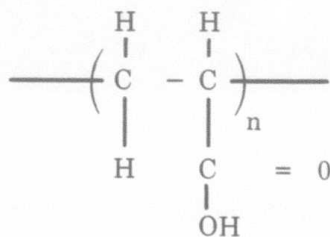
(1) reduction of surface moisture present on the substrate and reactor wall prior to coating and (2) the prevention of exposure to moisture immediately after coating.

#### TII/PPE Coating

TII is rigid and has excellent adhesion to the ethane polymer coating. This characteristic prevents the ethane polymer from wrinkling even if moisture permeates the coating. The TII/PPE coating remains intact even after allowing moisture to condense on the coating surface for 1 hour at 70°C. However TII is relatively ion permeable, and spots of crystal growth appear between the TII and ethane polymer coatings. The small crystals eventually push hard enough to break through the ethane polymer coating and form mounds on the surface. Figure 6 shows a typical sample tested 1 hour at 60°C/81% RH and 1 hour at 70°C/81% RH.

#### PAA/TII/PPE Coating

Poly (acrylic acid), PAA, has the molecular structure



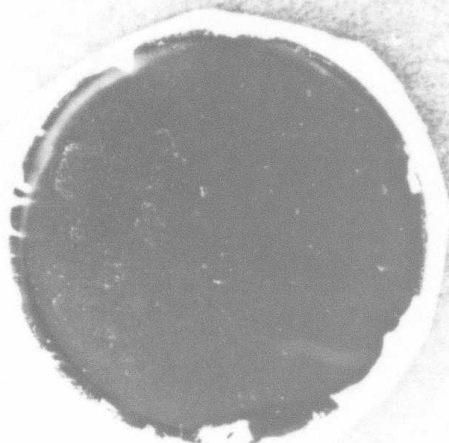


Figure 6. Minor crystal growth of KCl through TII/PPE coating. This sample had been exposed to 60°C/81% RH for 1 hour and then 70°C/81% RH for another hour. Almost all of the coating is still in good condition.

It is a good film-forming polymer surfactant with a hydrophilic group to adhere to inorganic materials. This material was used as an inner coating to reduce the hygroscopicity of the KCl surface and to prevent ions from permeating through the TII layer. The result was encouraging. A sample coated with PAA/TII/PPE showed good protection over most of the surface. Further descriptions of PAA results appear in Section 4.

#### **As<sub>2</sub>Se<sub>3</sub>/PPE**

This was a promising coating system. Figure 7 shows an As<sub>2</sub>Se<sub>3</sub>/PPE coating on a KCl substrate which withstood 1.5 hours at 50°C and 1 hour at 60°C at 81% RH. No crystal growth was noticed except at a few detect sites. The adherence of ethane film to the As<sub>2</sub>Se<sub>3</sub> coating was excellent.

#### **Ge/PPE and Ge/TII/PPE**

The Ge/PPE coating exhibited wrinkling after brief exposure to humidity. This failure is due to buckling of the Ge layer after humidity exposure. The damage occurs even under relatively mild testing conditions, e.g., 1 hour at 50°C/81% RH. However, the Ge/TII/PPE coating gives totally different results. As shown in Figure 8, a specimen of this coating survived 3.5 hours at 50°C/81% RH plus 3 hours at 60°C/81% RH plus 2 hours at 70°C/81% RH. Thus Ge/TII/PPE appeared to be a promising coating system.

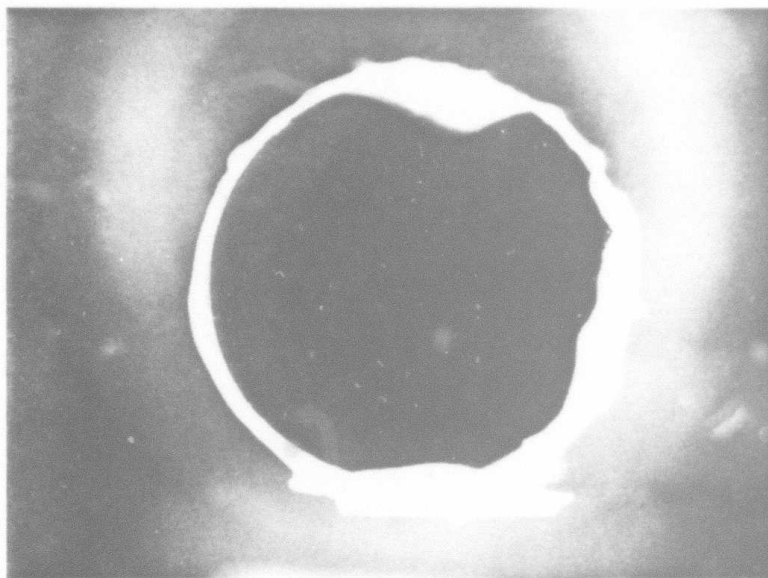


Figure 7.  $\text{As}_2\text{Se}_3/\text{PPE}$  coating, which remained intact after a humidity test for 1.5 hours at  $50^\circ\text{C}$  and 1 hour at  $60^\circ\text{C}$ .

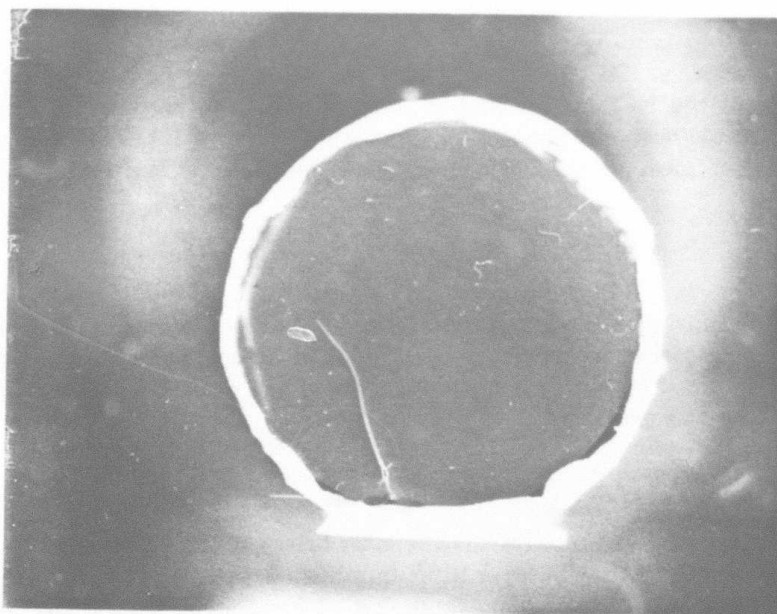


Figure 8.  $\text{Ge}/\text{TiI}/\text{PPE}$  coating remained in good condition after 3.5 hours at  $50^\circ\text{C}/81\% \text{ RH}$ , 3 hours at  $60^\circ\text{C}/81\% \text{ RH}$  and 2 hours at  $70^\circ\text{C}/81\% \text{ RH}$ .

### $\text{As}_2\text{Se}_3/\text{PE}/\text{PPE}$

A coating design consisting of  $\text{As}_2\text{Se}_3$ , crystalline polyethylene and hard plasma polymerized ethane showed the most promise. This coating was tested on KBr substrates for a 10-day humidity test cycle. Included in each test cycle was a severe condition for 8 hours at  $71^\circ\text{C}$  and 90% RH. Some coating defects were noted after the fourth cycle, but no significant overall damage was noted at the substrate surface. The defects were sealed with Torr-Seal,® and the samples continued the humidity cycle test. At the end of the 12th cycle, the coating starts to become rough. The polished line on the substrate surface under the coating starts to become wider, indicating moisture damage of the KBr surface. The wrinkling that is common with single organic layers of PPE also was eliminated.

The sequence of results is shown in Figures 9 through 16. Figure 9 shows the surface of an as-received KBr disc from Harshaw at a magnification of 80x. The polish lines on the surface are an effective way to evaluate the performance of the coating. Under environmental testing, the polish lines are more readily attacked by moisture. The lines tend to become wider as shown in Figure 10.

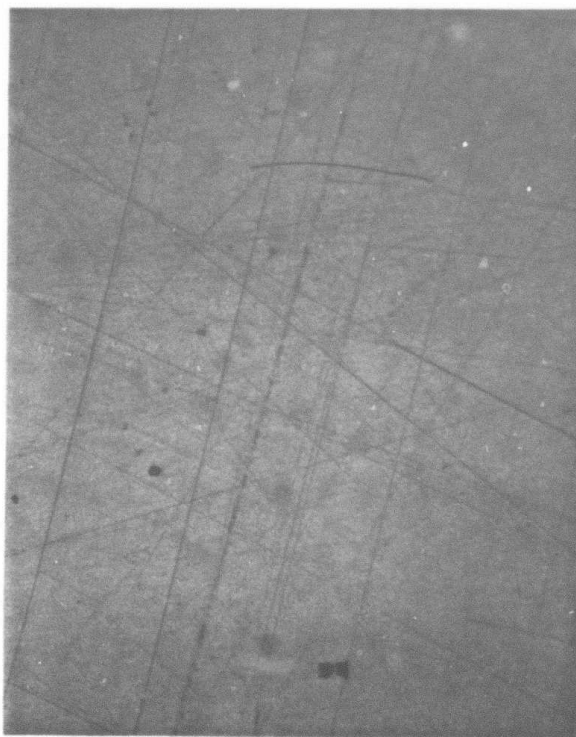


Figure 9. Surface of as-received KBr disc from Harshaw (80X).



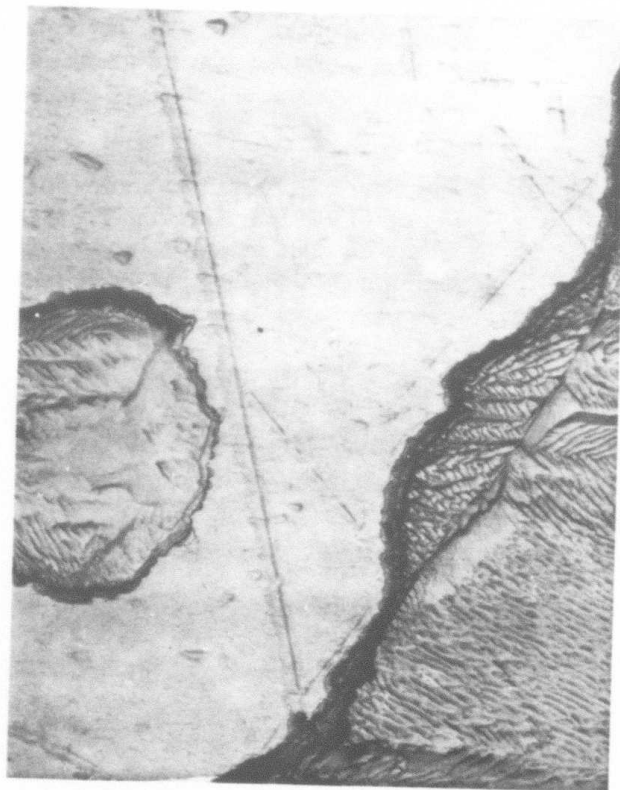
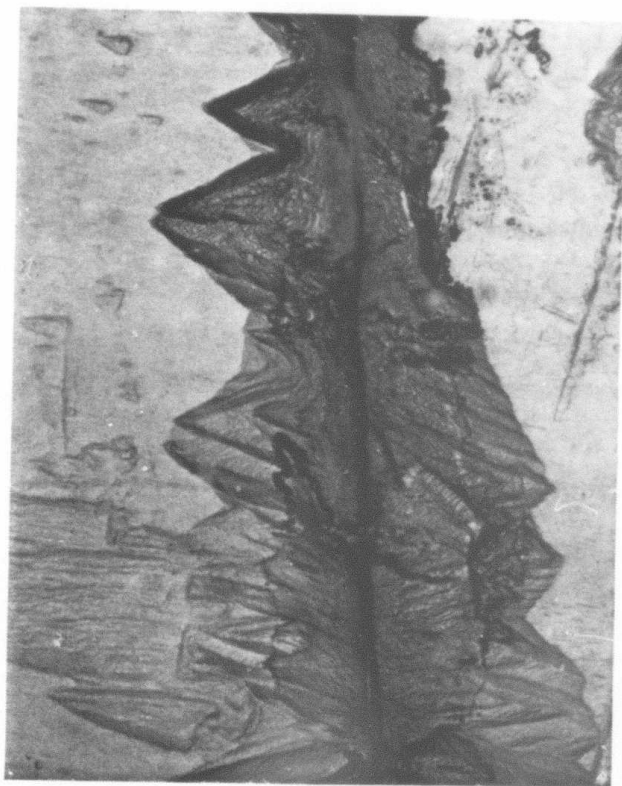


Figure 10. Two views of uncoated KBr exposed to 81% RH at 70°C for 3 hours (80X).

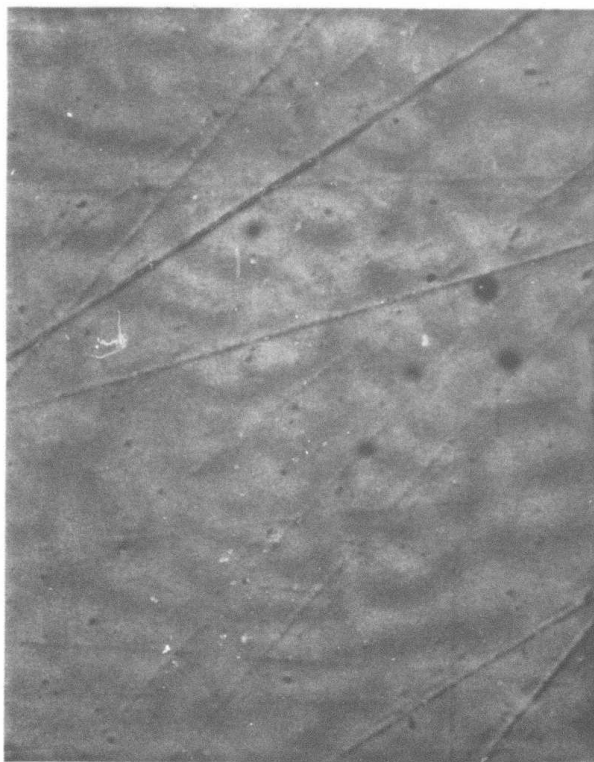


Figure 11. KBr coated with a  $2.5\mu\text{m}$  polyethylene single-layer coating after 2.5 hours at  $71^{\circ}\text{C}$  and 90% RH (80X).

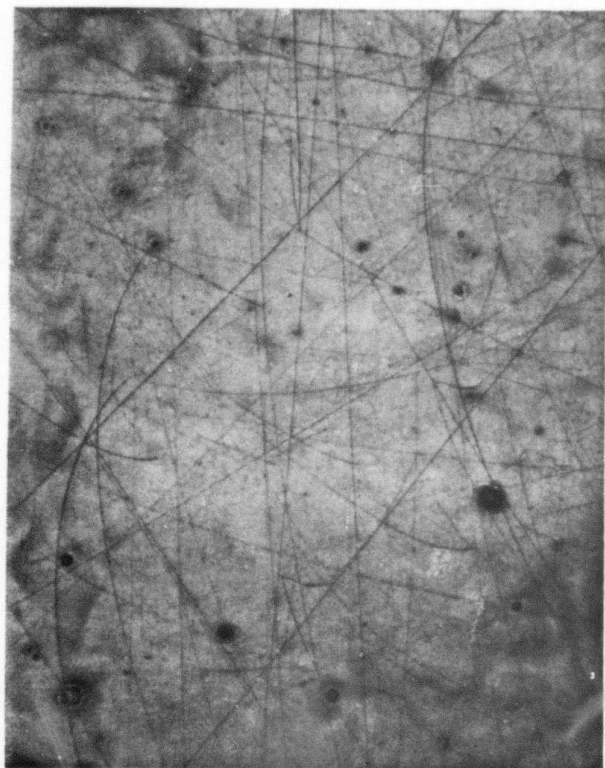


(a)

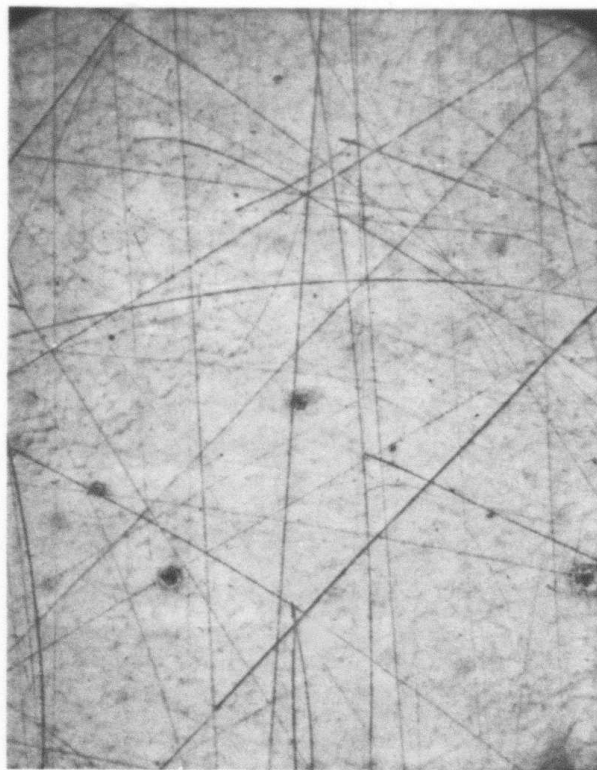


(b)

Figure 12. KBr coated with  $0.1\mu\text{m}$  KCl,  $0.88\mu\text{m}$   $\text{As}_2\text{Se}_3$ ,  $2.0\mu\text{m}$  polyethylene, and  $0.9\mu\text{m}$  plasma polymerized ethane, before testing; (a) 80X, (b) 160X.

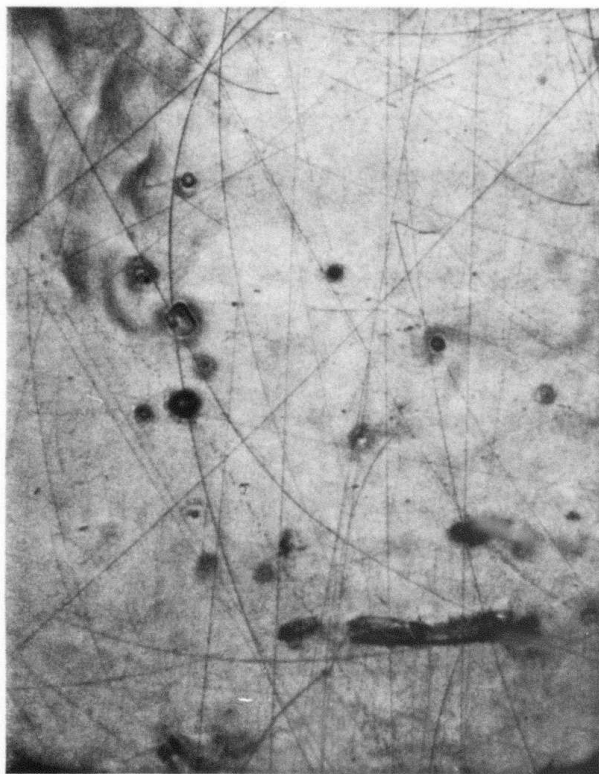


(a)

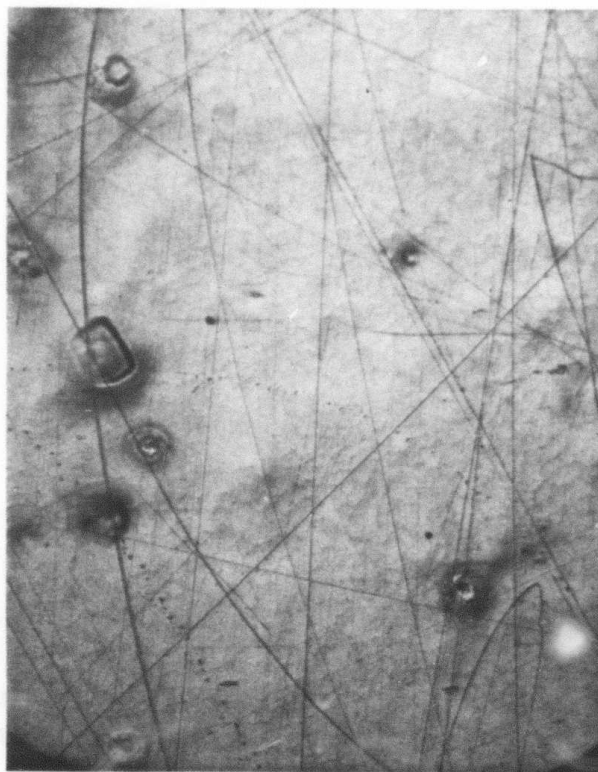


(b)

Figure 13. KBr coated with  $0.1\mu\text{m}$  KCl,  $0.88\mu\text{m}$   $\text{As}_2\text{Se}_3$ ,  $2.0\mu\text{m}$  polyethylene, and  $0.9\mu\text{m}$  plasma polymerized ethane, after six cycles; (a) 80X, (b) 160X.



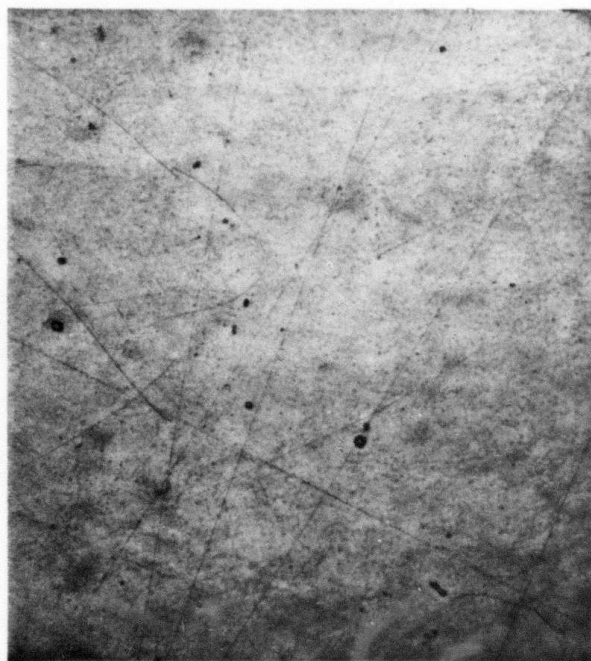
(a)



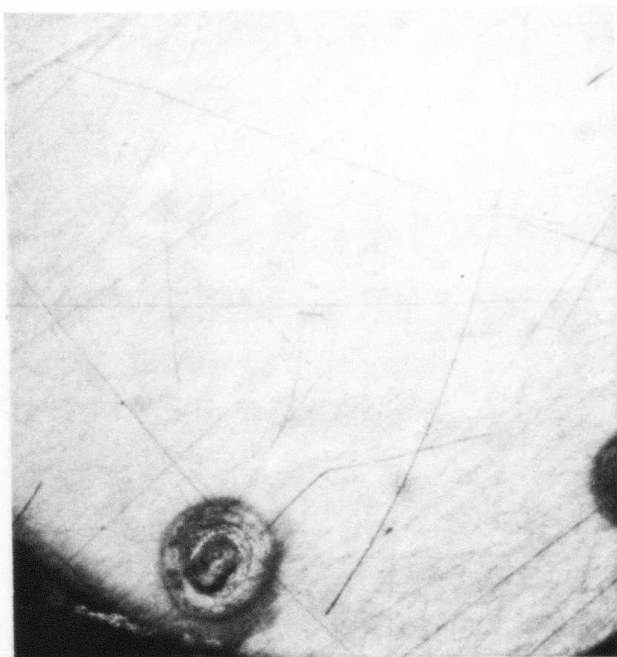
(b)

Figure 14. KBr coated with  $0.1\mu\text{m}$  KCl,  $0.88\mu\text{m}$   $\text{As}_2\text{Se}_3$ ,  $2.0\mu\text{m}$  polyethylene, and  $0.9\mu\text{m}$  plasma polymerized ethane, after 7 cycles; (a) 80X, (b) 160X.

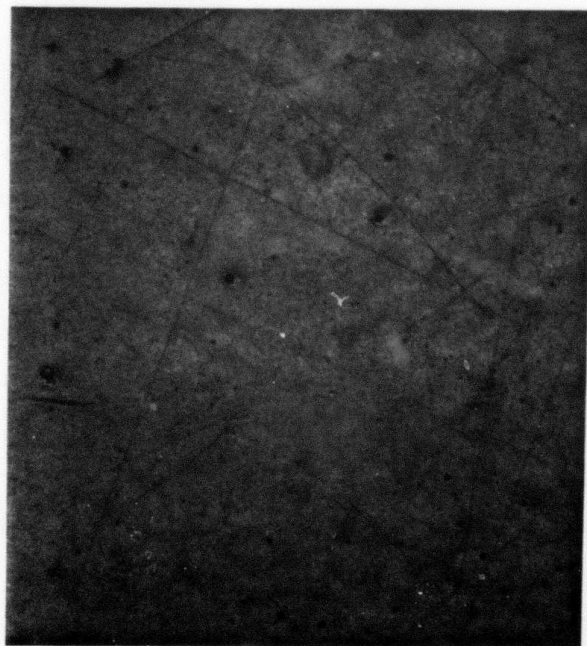




(a)

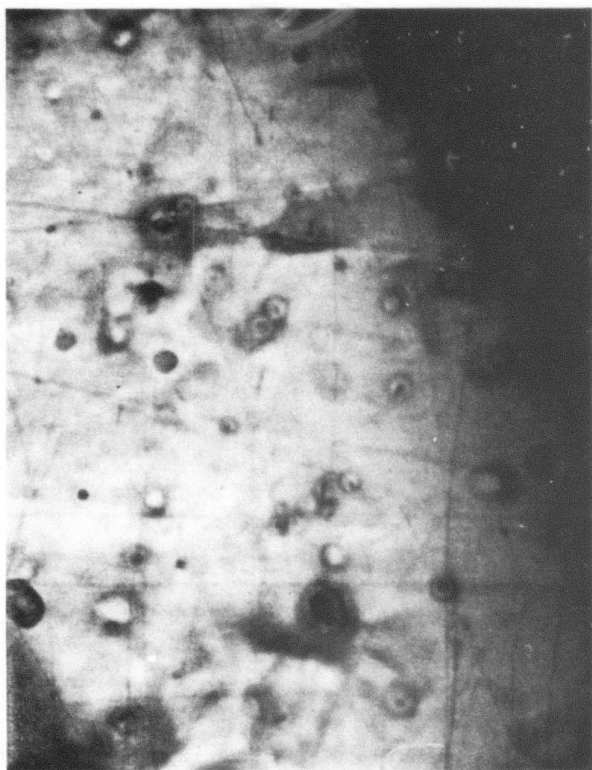


(b)

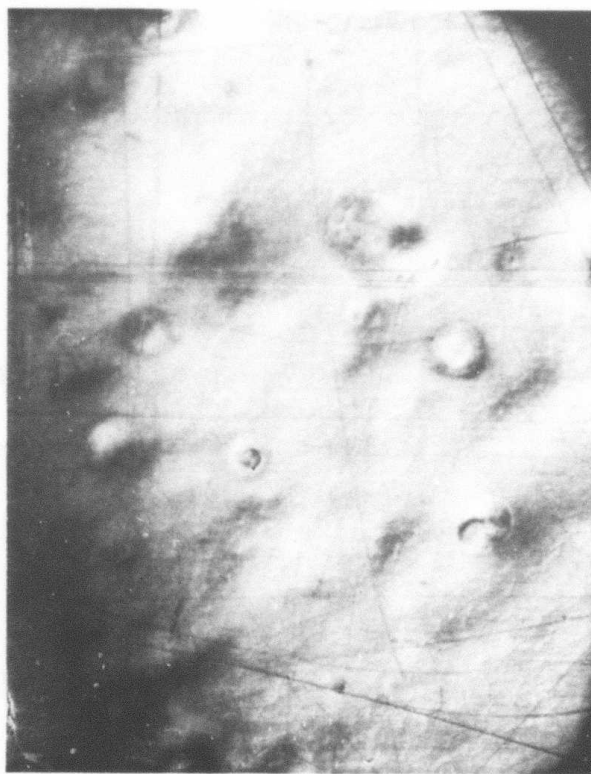


(c)

Figure 15. KBr coated with  $0.1\mu\text{m}$  KCl,  $0.88\mu\text{m}$   $\text{As}_2\text{Se}_3$ ,  $2.0\mu\text{m}$  polyethylene, and  $0.9\mu\text{m}$  plasma polymerized ethane; (a) after seven cycles (80X), (b) after eight cycles (160X), (c) after nine cycles (80X).



(a)



(b)

Figure 16. KBr coated with  $0.1\mu\text{m}$   $\text{As}_2\text{Se}_3$ ,  $2.0\mu\text{m}$  polyethylene, and  $0.9\mu\text{m}$  plasma polymerized ethane, after twelve cycles; (a) 80X, (b) 160X.

A KBr disc coated with a 2.5 $\mu$ m polyethylene single-layer coating after 2.5 hours at 71°C and 90% RH is shown in Figure 11. A 2.5 $\mu$ m polyethylene single-layer coating did not provide adequate protection. One can see that the width of the lines is significantly greater than that on the as-received surface. Figure 12 shows a KBr disc coated with 0.1 $\mu$ m KCl, then coated with 0.88 $\mu$ m As<sub>2</sub>Se<sub>3</sub>, 2.0 $\mu$ m polyethylene, and finally with 0.9 $\mu$ m plasma polymerized ethane before testing. Results after 6, 7, 8, 9 and 12 cycles are shown in Figures 13 through 16. These results were very encouraging. They indicated that the coating system As<sub>2</sub>Se<sub>3</sub>/PE/PPE failed beginning at isolated points, which presumably were due to imperfections in the coating. Thus, it was inferred that this coating system could withstand the desired environmental conditions if it could be prepared such that no defects were present.

As a result, most of the effort was concentrated on this coating system.

#### Other Coatings

Other coatings such as PbI<sub>2</sub>/PPE, BiF<sub>3</sub>/PE, NaF/PE, PbF<sub>2</sub>/PPE, BiI<sub>3</sub>/PPE and Bi<sub>3</sub>RbF<sub>4</sub>/PPE were tested under similar conditions. These coatings were less promising than the six coating systems described above, and no additional work was done on them.

#### CONCLUSION

Plasma-polymerized ethane (PPE), TiI/PPE, poly (acrylic acid)/TiI/PPE, As<sub>2</sub>Se<sub>3</sub>/PPE, and Ge/TiI/PPE are promising coating systems. All withstood a series of humidity tests (e.g., a few hours at 70°C and 81% RH) with minimal degradation.

The most promising coating system was As<sub>2</sub>Se<sub>3</sub>/PE/PPE, which indicated potential capabilities for withstanding the specified environmental conditions. Most of the work in the later stages of the contract was devoted to development and improvement of this system.



### **Section 3**

## **Surface Preparation**

**Task: Develop and evaluate cleaning procedures including stripping procedures, necessary to produce clean, dust-free surfaces, suitable for deposition of coatings.**

The main function of surface pretreatment of a coating substrate is to activate the surface for adhesion of the coating by modification of the surface or removal of surface contaminants such as dust, hydroxide, and fingerprints. Surface treatment techniques are many and can involve such things as cleaning the surface with a solvent to ensure good wetting, with a high voltage spark discharge, or by plasma treatment with inert gases. Primer coatings such as surfactants rich in polar functionality represent another surface pretreatment method.

### **SURFACE CLEANING**

The effect of surface cleaning on the performance of protective coatings was studied. Polished KBr discs from Harshaw were cleaned with various cleaning methods such as chemical etching, Ar plasma treatment and strip coating.

The procedure for chemically polishing the KBr crystal involved using HBr as the polishing agent and isopropyl alcohol as the washing agent. This procedure produced a smooth but uneven surface. The sample was then immersed in a diluted 50% HBr solution for a few seconds, but this still did not produce a smooth and even surface. More effort would be required to perfect the chemical polishing procedure for KBr discs.

A few KBr discs were cleaned by strip coating in a vacuum system. These samples together with as-received samples were coated with TII/PPE and subjected to a humidity test at 81% RH and 60° until they failed. The results obtained were not conclusive and did not indicate an advantage for this type of cleaning.

A strip-coat material with the brand name Durepoly® which has been used to remove dust on silicone wafers was also evaluated. This material clouded the surface of the KCl substrates and was very difficult to strip off. It was found to be an unsatisfactory strip-coat material for halide substrates.

## ION BARRIERS

When an alkali halide substrate such as KCl coated with inorganic film is submitted to humidity testing, small square crystals often grow on the outer surface. The growth of crystals on the surface of TlI coated on a KCl disc had been studied extensively<sup>(3)</sup>. A more detailed study comparing the effectiveness of ion barrier of materials such as ZnS, SiO, CeF<sub>3</sub>, CaF<sub>2</sub>, Tl and As<sub>2</sub>Se<sub>3</sub> was carried out at another contractor facility with internal funding in an effort complementary to the contract work. The results are described in Appendix A. The ratios of the transmittance of six coated substrates after and before humidity testing were obtained. These substrates show a post-humidity-test decrease in transmission which, when one considers the damage visible under a microscope, appears to be caused by scattering. The most favorable material for use as an ion barrier appeared to be As<sub>2</sub>Se<sub>3</sub>.

It was found that deposition of a material which acts as an ion barrier as the first layer in a coating structure is very effective for inhibiting growth of small crystallites through the coating. Crystallite growth had been a common mechanism for coating failure.

Because of the negative or inconclusive results of other possible surface preparation procedures, deposition of an ion barrier material became the main thrust for surface preparation. The surface preparation thus becomes an integral part of the fabrication of the entire coating structure.

## Section 4

### Surface Passivation

**Task:** Develop an effective passivation process by surface treatment and/or the addition of materials, such as:

1. Surfactants
2. Complex formation
3. Polar organic compounds and polymers
4. Surface-active macromolecules

The main purpose of a surface passivation coating is to convert the hygroscopic surface of an alkali halide to a hydrophobic surface by applying a near monolayer of an organic material with high polar functionality. Potentially useful classes of materials include surfactants, complex-forming and polar organic compounds, and surface-active macromolecules.

#### SURFACTANTS

A number of surfactants were evaluated. Results varied from unsuccessful to promising. Among those tested, poly(acrylic acid), PAA, was the most encouraging. It forms a smooth and uniform film that adheres strongly to alkali halides when a trace of FC-430® (obtained from the 3M company) is mixed with the coating solution. Although poly(acrylic acid) shows significant absorption in the wavelength range of 8 to 12 $\mu$ m, the thickness of a monolayer coating does not affect the transmission of substrate. This material was used as the inner coating layer to form PAA/TII/PPE.

Failures such as crystal formation on TII and wrinkling of the PPE were not observed for a KCl disc coated with PAA/TII/PPE after environmental testing for 1 hour at 60°C/81% RH and 1 hour at 70°C/81% RH. Such failures were typical when a coating system without PAA was subjected to similar testing conditions.

Other surfactants investigated were (a) octadecyl-dichloro-silane, (b) stearamidomethylpyridinium chloride, (c) N-carbomethoxyheptadecyl aminomethylpyridinium chloride and (d) quaternary ammonium chloride. Surfactant (a) forms a powderish deposit. Its presence as an inner coating does not affect the performance of the subsequent coating. Both surfactants (b) and (c) form spotty coatings, and their effectiveness as inner coatings was not evaluated. Surfactant (d) fails to form a dry film, and no significant effect was observed when it was used as an inner coating.

## **COMPLEX FORMATION**

This approach involves selection of chemicals which will react with the alkali halide to form a complex. Both methylene dianiline and ethylenediamine tetracetate were found to be ineffective. The surface of each treated halide was examined by electron spectroscopy for chemical analysis (ESCA).

The element nitrogen was not found on the treated surface. This indicates that the interaction between the above chemicals and the alkali halide is not strong enough to form a complex. Thus, these compounds showed no promise.

## **POLAR ORGANIC COMPOUNDS**

To study how polar organic compounds affect the surface of alkali halide, various long-chain saturated fatty acids were investigated. The problem with this class of chemicals is that they do not form dry films and thus cannot be successfully applied.

## **SURFACE-ACTIVE MACROMOLECULES**

Multifunctional prepolymers such as silicon and epoxy cure with a crosslinking agent to form a good film. These materials possess polar functionality and readily form a strong bond to alkali halides. GE SR-80® and Amicon epoxy yielded promising results. KBr discs treated with these materials and then coated with TII/PE/PPE significantly reduced water uptake.

## **CONCLUSION**

The results of the studies on materials for surface passivation are summarized in Table 1. Poly(acrylic acid) and silicone compound (SR-80®) are two of the most promising surface passivation coatings.

In summary, although some surface passivating compounds studied here appear to offer some promise, they do not lead to significant additional benefits when compared with use of an ion barrier  $\text{As}_2\text{Se}_3$  film applied directly to the alkali halide. Accordingly, most of the effort was devoted to optimization of the  $\text{As}_2\text{Se}_3$  organic coating system.

Table 1. Development of a Passivation Process

Materials	Test Results	Comments
<b><u>Surfactant</u></b>		
Octadecyl-dichloro-silane $\begin{array}{c} \text{H} \\   \\ \text{Cl}-\text{Si}-\text{Cl} \\   \\ \text{C}_{18}\text{H}_{27} \end{array}$	Unsuccessful	Does not form a film
Stearamidomethylpyridinium chloride $\text{C}_{17}\text{H}_{35}\text{CONHCH}_2\text{N}^+\text{C}_5\text{H}_5, \text{Cl}^-$	NT*	Forms a poor film
N-carbomethoxyheptadecyl aminomethylpyridinium chloride $\text{C}_{17}\text{H}_{35}\text{N}^+\text{CH}_2\text{N}^+\text{C}_5\text{H}_5, \text{Cl}^-$ $\text{COOCH}_3$	NT*	Forms a poor film
Poly (acrylic acid)	Promising	Good adhesion to halides
Quaternary ammonium chloride	Unsuccessful	Does not form a dry film
<b><u>Complex Formation</u></b>		
Methylene dianiline	Unsuccessful	Does not form a film
Ethylenediamine tetraacetate	NT*	Does not form a film
<b><u>Polar Organic Compounds</u></b>		
Long-chain saturated fatty acids	Unsuccessful	Does not form a dry film
<b><u>Surface Active Macromolecules</u></b>		
Silicone compound (SR-80®)	Promising	These compounds cure to form good films and have excellent bond strength
Epoxy compound (Amicon®)	Promising	

\*NT=Not Tested

## Section 5

### Moisture Permeability Measurement

**Task:** Determine moisture permeability for eight selected materials: polyethane, polyethylene, acrylic acid-ethylene copolymer, poly(vinylidene chloride), thallium iodide (TII), lead fluoride ( $\text{PbF}_2$ ), zinc sulfide (ZnS) and arsenic selenide ( $\text{As}_2\text{Se}_3$ ) by depositing different thicknesses of each material on a permeability measurement cup and determining the weight loss of a water solution at different temperatures.

A study of the movement of moisture through films is very important to the selection of coating materials for material protection. This study was carried out on 10 coating materials which are potentially useful for coating applications. They include the eight materials listed in the task statement: polyethylene (PE), plasma polymerized ethane (PPE), polyethylene-acrylic acid copolymer (PEAC), and polyvinylidene chloride ( $\text{PVCl}_2$ ), thallium iodide (TII), lead fluoride ( $\text{PbF}_2$ ), zinc sulfide (ZnS) and arsenic selenide ( $\text{As}_2\text{Se}_3$ ), plus two additional materials of potential interest: polyvinylidene fluoride ( $\text{PVF}_2$ ) and calcium fluoride ( $\text{CaF}_2$ ).

Permeability measurements on all polymeric coatings except PPE were taken by using a single-layer film of the material being measured. Measurement of the permeability for PPE used a polyimide (PI) film as the substrate. In other words, a PPE film was plasma polymerized on a PI film, and the moisture permeability of PPE was determined by measuring the permeability of composite layers and that of the PI substrate layer. Further, the permeability of the inorganic materials was determined by the same technique as for PPE.

#### FILM PREPARATION

Films of PE, PEAC,  $\text{PVF}_2$  and  $\text{PVCl}_2$  were prepared by solvent coating onto a 35×35mm microscope cover glass. This was followed by baking at 130°C in a vacuum oven for 2 hours. The coated glass was sealed to a permeability cup which had 10-ml capacity, 4.5-cm<sup>2</sup> circular cross-sectional area, and a side arm through which saturated salt solutions or water could be introduced. The glass substrates can be separated from the sealed films after prolonged immersion in water. The finished cup with the film is shown in Figure 17.

Films of PPE, TII,  $\text{PbF}_2$ , ZnS,  $\text{As}_2\text{Se}_3$  and  $\text{CaF}_2$  were prepared by first preparing a permeability cup with polyimide (PI) film using the technique described above. The coating to be measured was then deposited onto the PI film. PPE films were deposited by plasma polymerization. The five inorganic coatings were deposited by thermal evaporation.

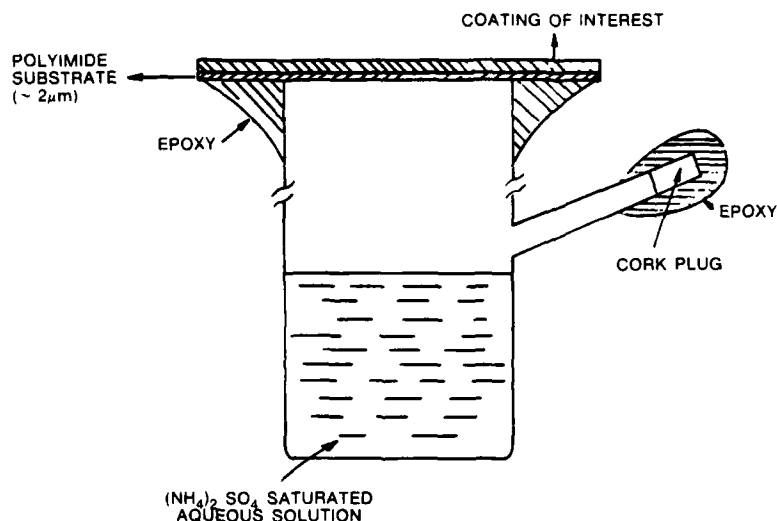


Figure 17. Moisture permeability measurement cup.

## PERMEABILITY MEASUREMENT

A gravimetric technique was used to determine water vapor permeability. Permeability cups filled with saturated ammonium sulfate solution were placed in a desiccator containing an indicating desiccant (anhydrous  $\text{CaSO}_4$ ). The desiccator in turn was placed in an oven controlled to within  $\pm 1^\circ\text{C}$ . The pressure difference is given by the equation

$$\Delta p \cong RH \cdot p_t$$

where RH is the relative humidity inside the cup and  $p_t$  is the vapor pressure of water at temperature  $t$ . The relative humidity outside the cup was practically zero. All data reported here were obtained at 81% RH, which was controlled by the saturated ammonium sulfate solution. The water loss rate at each temperature was determined by periodic weighing of the cup on a balance accurate to  $\pm 0.1$  mg, usually every 24 hours in the case of steady-state experiments. The reported data are the averages of the values from several cups and were reproducible to better than  $\pm 10\%$ .

In determining the permeability ( $P$ ) of single-layer coatings such as PE, PEAC,  $\text{PVF}_2$  and  $\text{PVC}_2$ , the permeability  $P$  was calculated by

$$P = \frac{Q\ell}{\Delta p}$$

where  $Q$  is the rate weight loss of the cup at steady-state,  $\ell$  is the thickness of the film and  $\Delta p$  is the water vapor pressure difference across the film.

Films such as PPE, TlI, PbF<sub>2</sub>, ZnS, As<sub>2</sub>Se<sub>3</sub> and CaF<sub>2</sub> were deposited on a substrate film PI. To determine the permeability of each film from the composite films, the permeability of the PI film was first determined according to the equation above. The permeability of each deposited film was then calculated by

$$\frac{1}{P_c} = \frac{\nu_1}{P_1} + \frac{\nu_2}{P_2}$$

where  $P_c$  is the permeability of the composite film,  $P_1$  and  $P_2$  are the permeabilities of PI and the film of interest, respectively, and

$$\nu_i = \frac{\ell_i}{\ell}$$

is the volume fraction of layer  $i$  with  $\ell_i$  the thickness of layer  $i$  and  $\ell$  is the total thickness, i.e.,  $\ell = \ell_1 + \ell_2$ .

The permeabilities of organic coatings, PE, PPE, PEAC, PVF<sub>2</sub> and PVCl<sub>2</sub> along with that of PI in units of cm<sup>3</sup> (STP) sec<sup>-1</sup> cm cm<sup>-2</sup> (cmHg)<sup>-1</sup> as a function of inverse absolute temperature are plotted in Figure 18. The permeabilities of the inorganic films TlI, PbF<sub>2</sub>, ZnS, As<sub>2</sub>Se<sub>3</sub> and CaF<sub>2</sub> are plotted in Figure 19. As can be seen, inorganic coatings are generally less permeable to moisture than organic films. This is because the inorganic coatings are crystalline and dense, whereas organic films are amorphous and porous. However, inorganic coatings deposited by thermal evaporation usually contain defects such as pinholes and nonuniformities. Thus, moisture can reach the substrate material surface locally. The presence of water assists ionic mobility and dissolution. Also some inorganic coatings are poor ion barriers, and ions will diffuse and recrystallize on the coating surface. This may well be the mechanism that is responsible for the crystal growth on an inorganic coating surface when a halide substrate coated with an inorganic film is exposed to humidity. On the other hand, although most of the organic films except PVCl<sub>2</sub> show more permeability to moisture because of their amorphous and relatively porous nature, they are good ion barriers. Ions which become mobile because of the presence of an aqueous phase are blocked by the organic coating barrier. These ions tend to grow back on the original surface, and, therefore, there is no recrystallization on the coating surface.

Of the organic materials tested, only PE and PPE have low enough absorption in the infrared portion of the spectrum to be useful as coating materials. PE, which is partially crystalline, has lower moisture permeability than PPE. However, because PPE is deposited by vacuum processes, the thickness can be controlled more accurately for fabrication of an antireflective coating. Thus the choice of organic material in the coating design is a combination layer of PE and PPE, with most of the thickness consisting of PE for minimum moisture penetration, and with the entire thickness controlled by the final PPE deposition. As Section 2 described, this combination also resists the wrinkling that is often encountered with single layers of PPE as the organic material.



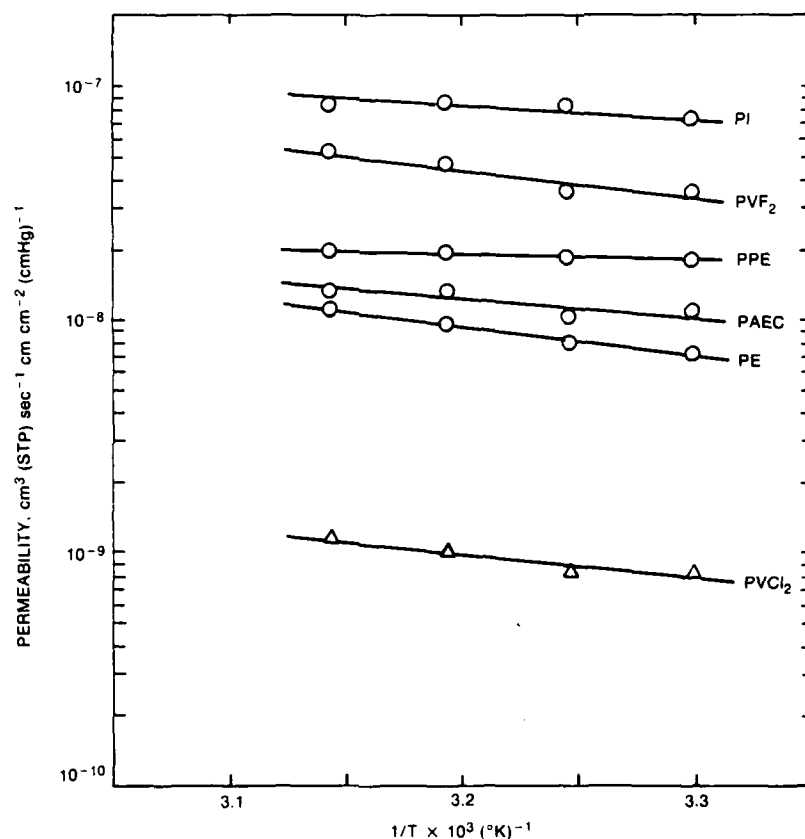


Figure 18. Moisture permeability versus reciprocal of absolute temperature  $T$  for six organic coating materials: PI = polyimide. PV F<sub>2</sub> = polyvinylidene fluoride. PPE = plasma polymerized ethane. PE = polyethylene. PAEC = polyacrylic acid-ethylene copolymer. PVCl<sub>2</sub> = polyvinylidene chloride.

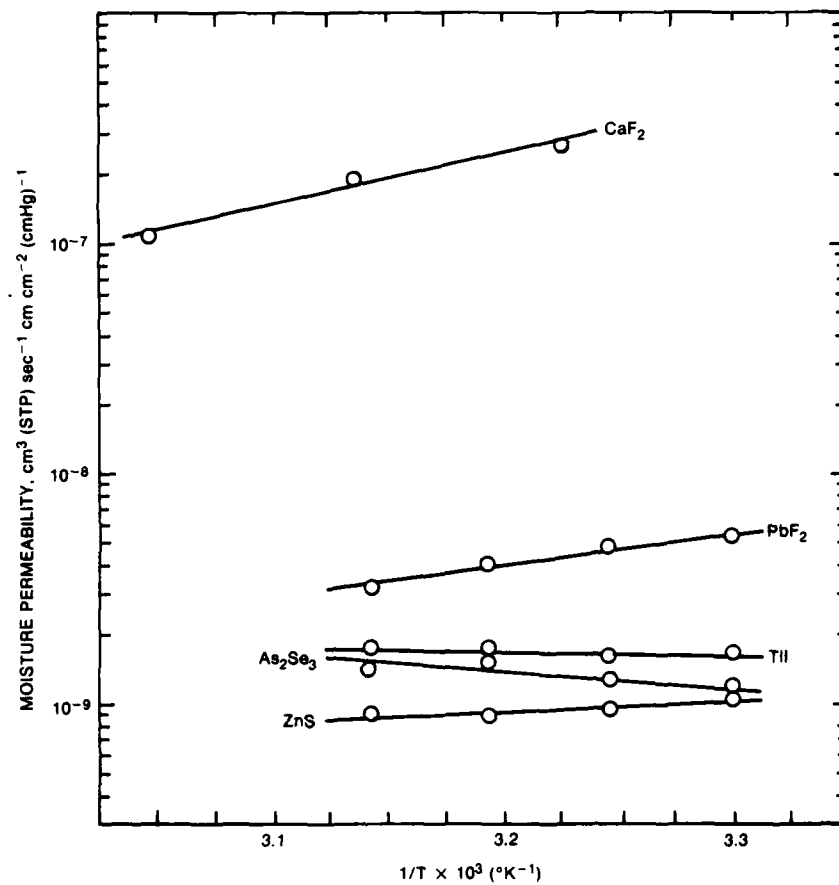


Figure 19. Moisture permeability versus reciprocal of absolute temperature  $T$  for five inorganic coating materials.

## Section 6

### Characterization of Coatings

**Task:** Perform the following experiments and studies on the coating materials:

1. Measure infrared transmission — Fourier transform spectrometry (FTS).
2. Surface texture analysis — Scanning electron microscopy (SEM).
3. Surface composition analysis — X-ray photoelectron spectroscopy (ECSA) and Auger spectroscopy.
4. Kinetics of moisture attack — Thermogravimetric analysis (TGA).
5. Heat of moisture-halide interaction — Differential scanning calorimetry (DSC).

#### INFRARED TRANSMISSION MEASUREMENT

Organic coating materials useful for protection of alkali halide optical elements to be used in thermal imaging systems for the 8 to 12 $\mu$ m region must be transmissive in that spectral region. Previous screening of many candidate materials<sup>(2)</sup> measured their infrared transmission. This work used a Digilab Fourier transform spectrometer (FTS). The screening identified polyethylene and polyethane as especially promising materials because of their low absorption in the 8 to 12 $\mu$ m spectral region.

Figure 20 shows the infrared transmission of a sample of uncoated KCl. It is apparent that the KCl substrate alone does not absorb at wavelengths less than 15 $\mu$ m except for a few spikes which may be due to surface defects or impurities. Plasma polymerized ethane polymer exhibits absorption only in a narrow band at 3000 to 2840  $\text{cm}^{-1}$  (3.3 to 3.5 $\mu$ m) and at two peaks, i.e., 1450  $\text{cm}^{-1}$  and 1357  $\text{cm}^{-1}$  as shown in Figure 21. This figure applies to a 0.5 $\mu$ m-thick layer of PPE on KCl. These absorptions lie outside the 8 to 12 $\mu$ m spectral region. The narrow band is attributable to C-H bond stretching, whereas the two peaks are identified as C-H asymmetrical bending and C-H symmetrical bending respectively. The noticeable low absorption appearing in other spectral regions makes ethane polymer attractive for infrared applications. This lack of absorption in the infrared is not typical of organic polymer films. When the plasma polymerized ethane polymer coating was treated with H<sub>2</sub> plasma, no change in the spectrum was observed (Figure 22). However, the treatment enhances the hardness of ethane polymer.

Table 2 summarizes infrared transmission measurements. In thicknesses of 1 to 2 $\mu$ m, all the materials tested except PE and PPE exhibit absorption bands of varying strengths in the 8 to 12 $\mu$ m region. Because of these results, work was concentrated on organic coating materials in the PE/PPE system.

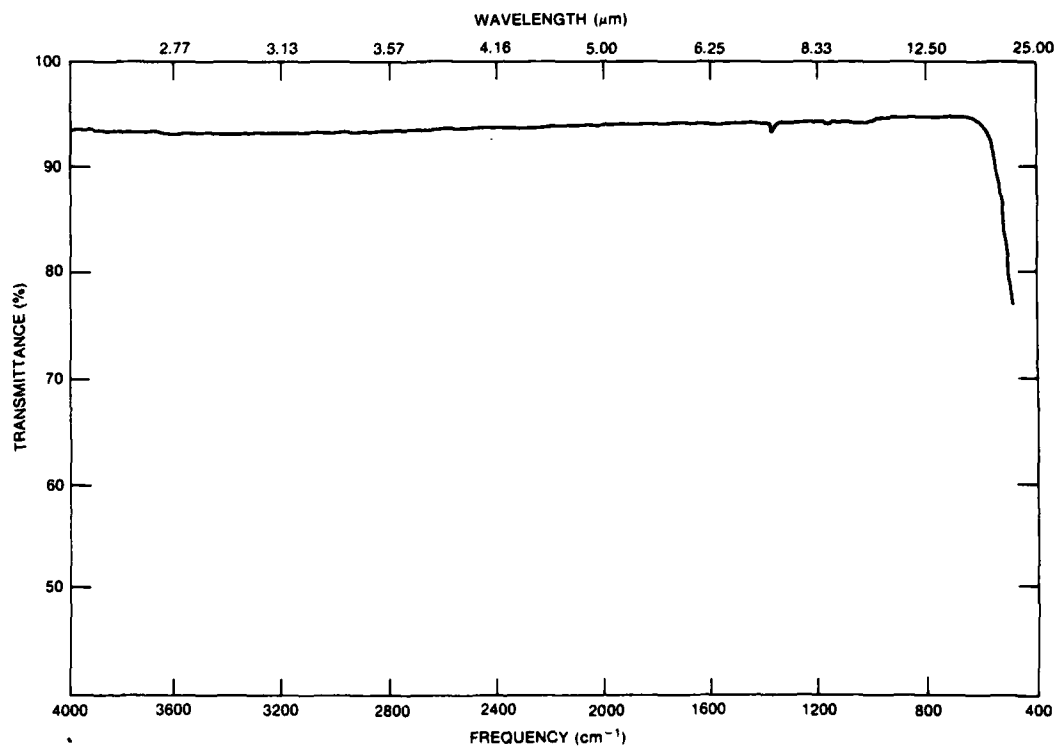


Figure 20. Infrared spectrum of typical as-received KCl substrate.

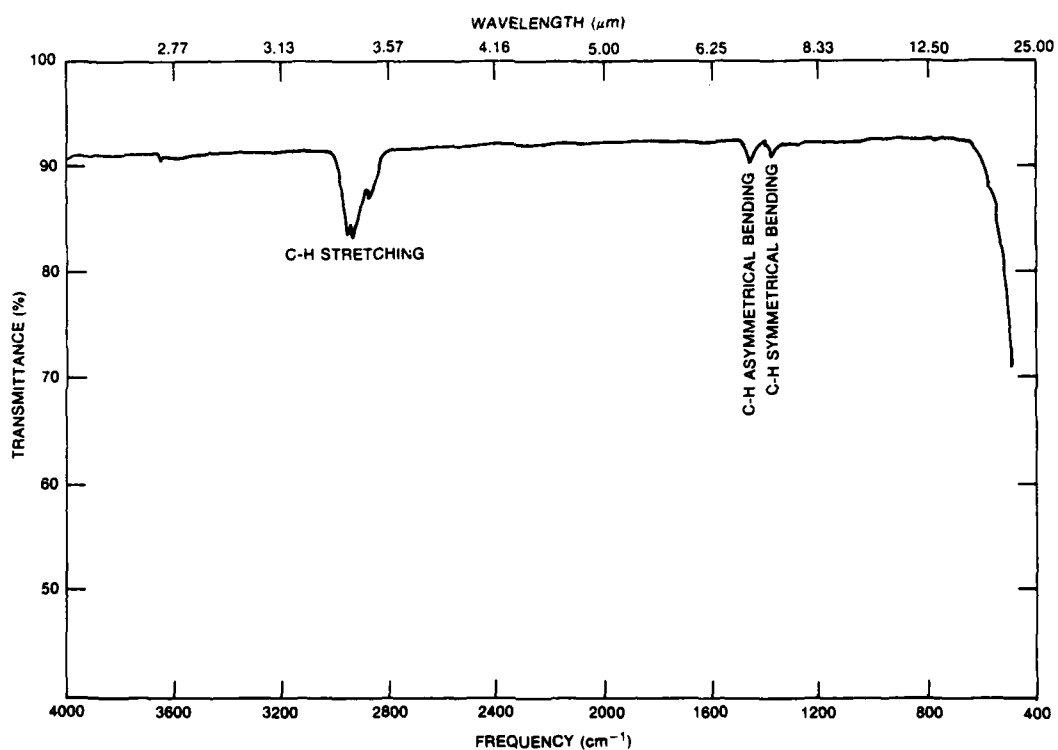


Figure 21. Infrared spectrum of plasma polymerized ethane.

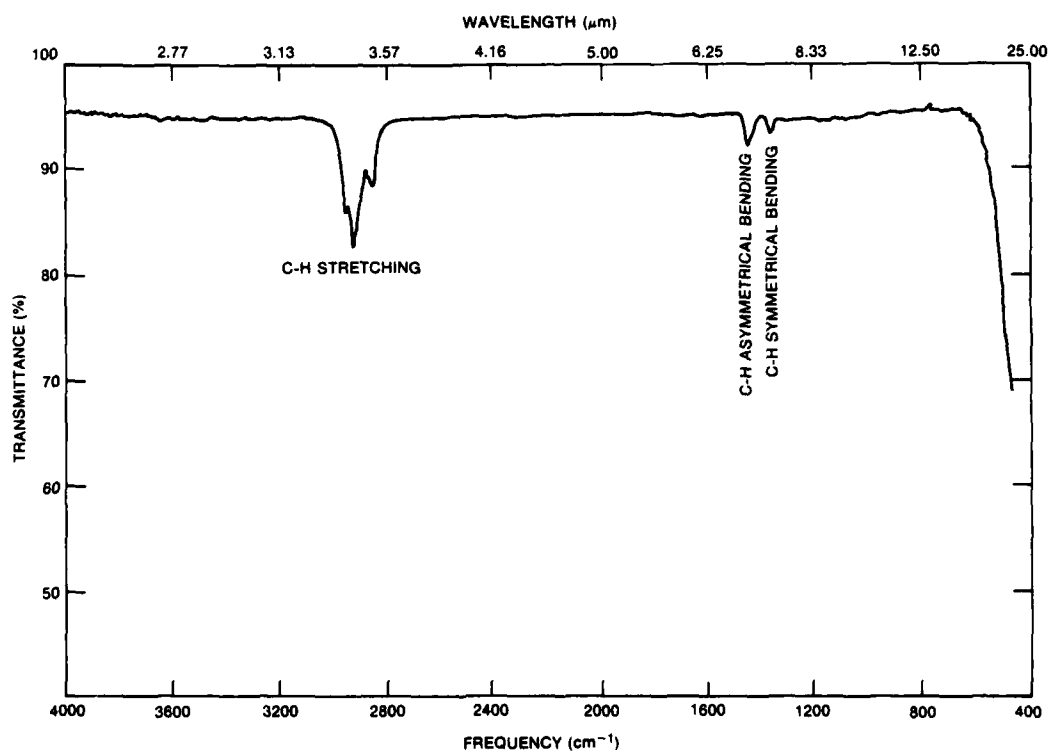


Figure 22. Infrared spectrum of plasma polymerized ethane treated with H<sub>2</sub> plasma.

Table 2. Summary of IR Absorption in 8 to 12 $\mu$ m Region

	IR Absorption at $\mu$ m				
	8	9	10	11	12
Plasma Polymerized Ethane Polymer	Not detectable with a film of $\sim 2\mu$ m				
Polyethylene	Not detectable with $\sim 2\mu$ m thick film				
Acrylic Acid-Ethylene Copolymer			W		
Ethylacrylate-Ethylene Copolymer	M				
Polyterpene	W				
Polyethylene Low Density	W				
Ethlene-Propylene Copolymer	W		W		
Polytetrafluoroethylene	VS		M		
Polytrifluorochloroethylene	VS		VS	W	
Nylon 6	W				
Nylon 610			W		
Nylon 11	W				
Polyvinylpyrrolidone	W				
Polyvinylcyclohexane			W		
Poly-Para-Xylene					VS

Note: W O.D. = 0.05 - 0.1 Base on samples with  $\sim 2$  mils thickness, O.D. is Optical Density.

M O.D. = 0.1 - 0.3

S O.D. = 0.3 - 0.5

VS O.D. > 0.5

## SURFACE TEXTURE ANALYSIS

The surface texture of uncoated forged KBr discs was studied by scanning electron microscopy (SEM). SEM pictures with various magnification at various locations (Figures 23 through 26) show scratches, defects, cracks, and nucleations on the surface. Note that these figures represent some of the worst surface conditions experienced. After the discs were coated with polyethylene (Figures 27 through 29), the coating itself seems to be smooth and covers most of the minor defects. Those coarse defects that the coating cannot cover are likely to be the spots that have poor resistance to moisture damage.

## SURFACE COMPOSITION ANALYSIS

X-ray photoelectron spectroscopy (ESCA) and Auger spectroscopy were considered for determining the effectiveness of surface treatment by evaluating the bonding between the molecules of surface-active solutions and the halide surface. The success of this experiment depends on the preparation of a monolayer coating that was never achieved. Thus, this effort was discontinued.



Figure 23. Scanning electron micrograph of uncoated KBr (2000X).

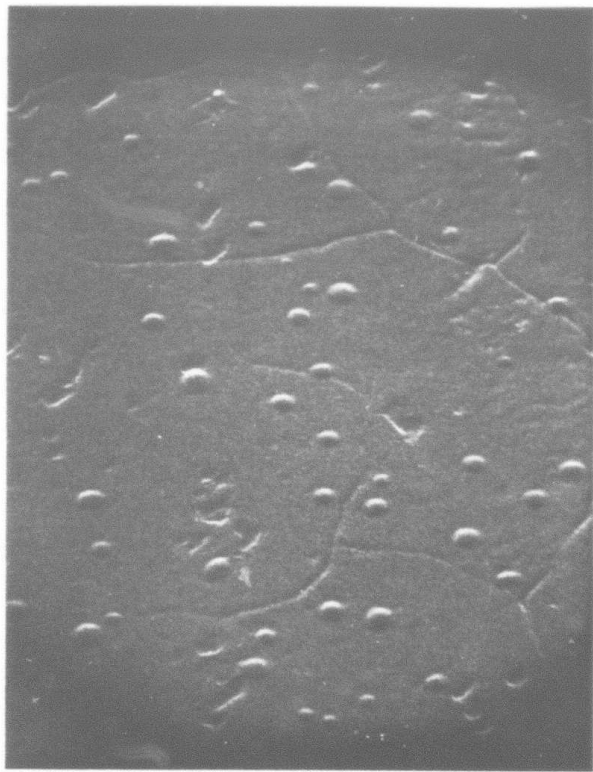


Figure 24. Scanning electron micrograph of uncoated KBr (5000X).



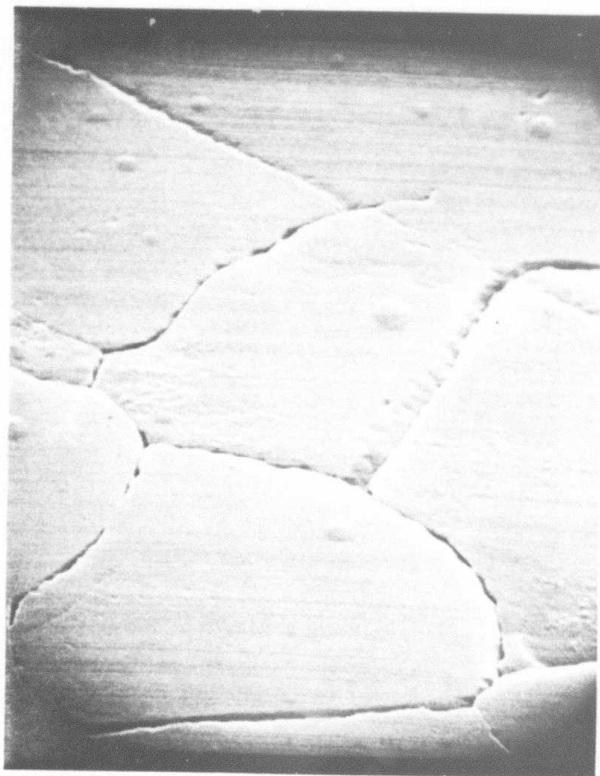


Figure 25. Scanning electron micrograph of uncoated KBr (5000X).



Figure 26. Scanning electron micrograph of uncoated KBr (10,000X).

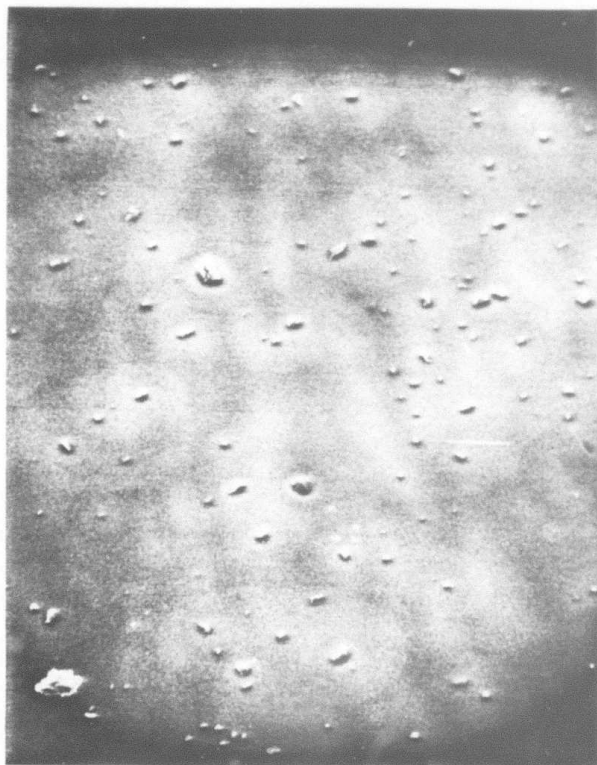


Figure 27. Scanning electron micrograph of KBr coated with polyethylene (100X).



Figure 28. Scanning electron micrograph of KBr coated with polyethylene (200X).



Figure 29. Scanning electron micrograph of KBr coated with polyethylene (1000X).

#### KINETICS OF MOISTURE ATTACK

An alkali halide is a water-soluble material that is readily attacked by moisture in the environment. Thus, to devise a protective coating for alkali halides, an understanding of their water absorption behavior is essential.

Numerous coating materials were tested with polished KBr discs from Harshaw used as substrates. Experiments were carried out at a constant 81% RH and various temperatures (40°, 45°, 50°, 55° and 60°C) for 4 hours or 7 hours. The weight increase of the samples was determined gravimetrically.

Figure 30 shows the test results for as-received polished KBr from Harshaw. An S-shape behavior was observed for the weight increase versus temperature. This weight gain due to water uptake was also plotted as a function of inverse absolute temperature as shown in Figure 31. Both 4-hour and 7-hour experiments gave linear relationships. A point representing the reduced water uptake when the KBr is coated with PPE is also included.

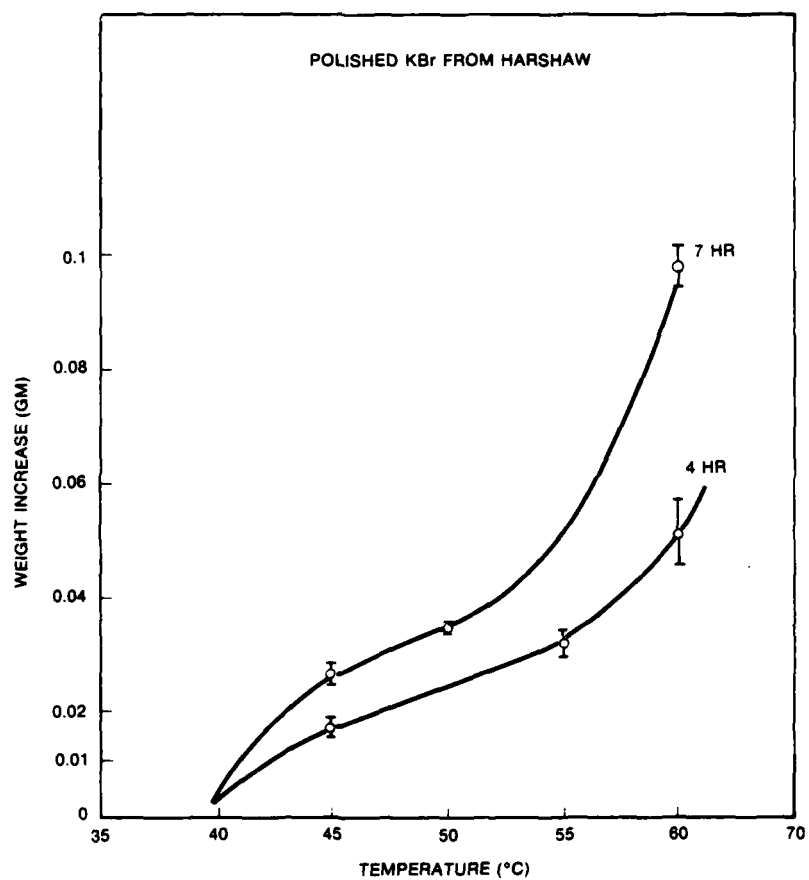


Figure 30. Water uptake of uncoated KBr versus temperature.

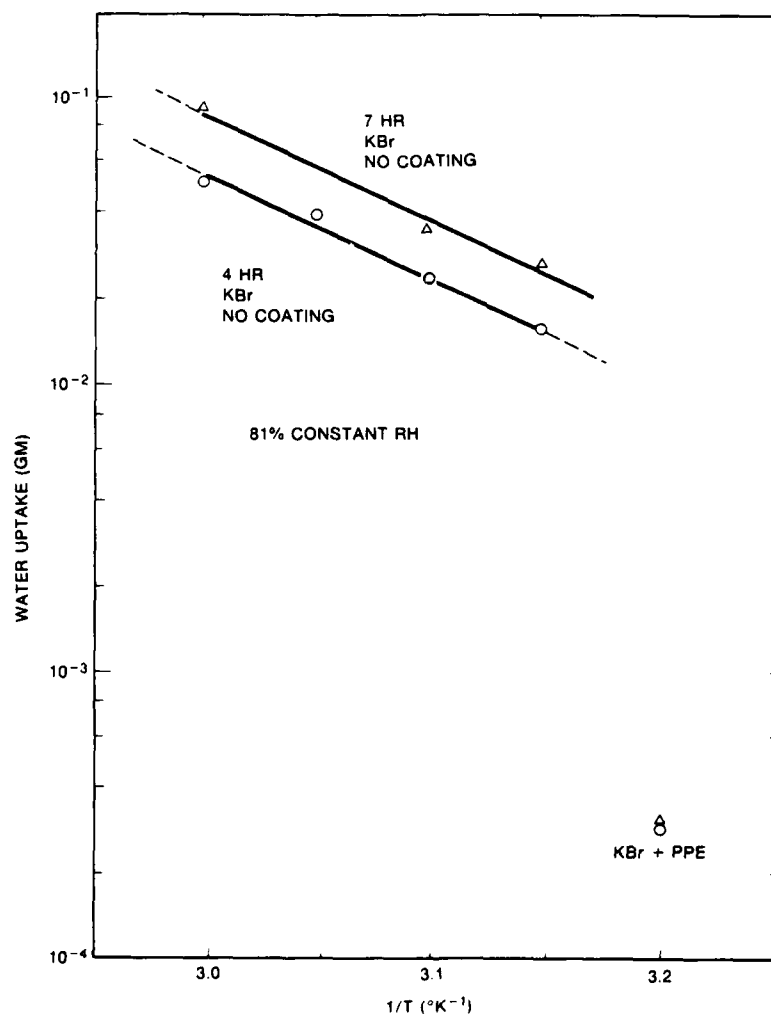


Figure 31. Water uptake of uncoated KBr versus reciprocal of absolute temperature. For comparison points for KBr coated with plasma polymerized ethane are included.

Hucher, Oberlin and Holart<sup>(4)</sup> have studied adsorption isotherms on cleaved surfaces of halides. They determined the weight gained in terms of the change in surface conductivity in the presence of wafer vapor. Plots of the logarithm of surface conductivity versus relative humidity for KBr, KCl, NaBr and NaCl showed an S-shape similar to that of Figure 30. The conductivity of the bromides was higher than that of the chlorides at the same relative humidity.

Three different domains were obvious in the field of relative humidity between 0 and 0.8. The first domain is attributable to physical adsorption of water on the surface, the second to hydrolysis of the cations  $\text{Na}^+$  and  $\text{K}^+$  by the water molecules and the third to dissolution. These interpretations were supported by electron micrograph pictures after each exposure of the halide surfaces in the three different regions.

Although these experiments are somewhat different from those of Hucher, et al., in that they were carried out at a constant relative humidity rather than at a constant temperature ( $25^\circ\text{C}$ ), the interpretation of the three regions of the S-shaped curves is applicable in both cases.

Thus, it was concluded that the mechanism of water uptake is: (a) initial adsorption of water on the surface of the halide initially; then (b) change in the surface area of the halide, presumably because the crystals coalesce with a decrease in surface area with no or little uptake of water, and finally (c) penetration of water into the crystal lattice and condensation of additional water on the surface, with rapid uptake of water. A schematic diagram of this process is shown in Figure 32.

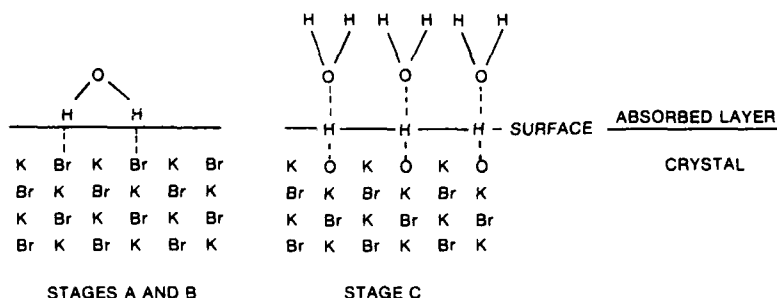


Figure 32. Schematic diagrams of surface attack of KBr by water in stages A, B and C, as defined in the text.

Polished KBr discs with various coatings also were tested for water uptake.

Coatings tested included polyacrylic acid (PPA)/thallium iodide (TII)/polyethylene (PE)/plasma polymerized ethane (PPE), Amicon® epoxy/TII/PE/PPE, Sr-80® (GE silicon coating)/TII/PE/PPE,  $\text{PbF}_2$ /PE/PPE, Amicon® epoxy, Humiseal®, polystyrene (PS), PAA/PS, and methylenedianiline/PS. The weight gained because of water uptake for all these coatings after 7 hours at 81% RH and  $60^\circ\text{C}$  (some coatings at  $70^\circ\text{C}$ ) are shown in Figure 33. For comparison purposes, the weight gain of uncoated polished KBr discs tested for 7 hours at a constant humidity of 81% as a function of temperature is also shown as the solid s-shaped curve. All the coatings tested slow down the water uptake of KBr. Among these, PAA/TII/PE/PPE, Amicon®/TII/PE/PPE, SR-80®/TII/PE/PPE and  $\text{PbF}_2$ /PE/PPE are especially effective moisture barriers.

These results show that water penetrates all the organic coatings to some extent. Thus, the coating must allow for this penetration and reduce its harmful effects. Again the necessity for an ion barrier, such as  $\text{As}_2\text{Se}_3$ , is indicated.

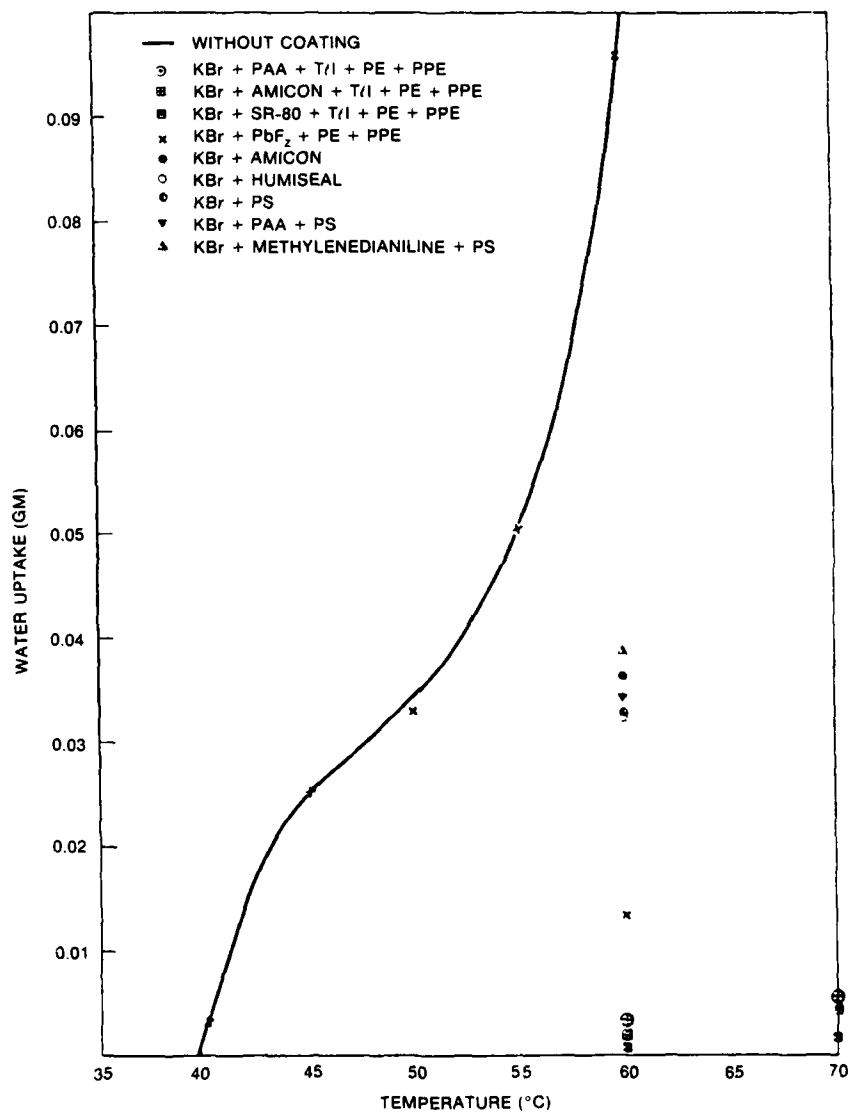


Figure 33. Water uptake of uncoated KBr and KBr with various coatings versus temperature.

The results are particularly significant in defining the problem that exists in meeting the severe humidity specification of Mil-Std-810B, which calls for environments of 70°C and 95% relative humidity in some parts of the cycle. This condition lies in water uptake stage (c), as defined above, so the mechanism of water attack involves surface dissolution. Because moisture penetrates any coating layer, organic or inorganic, at least to some extent as Section 5 has shown, some moisture will reach the surface. The coating layer, to be transparent in the 8 to 12 $\mu$ m region, must be thin enough that some moisture will penetrate to the surface and the surface will begin to dissolve. As the relative humidity decreases outside, moisture moves back out, carrying alkali and halide ions with it. This is a common failure mechanism by which crystal growth on the outside of the coating occurs. This crystal growth can be prevented by an ion barrier, but there is still the difficult problem of partial surface dissolution under the coating when environmental conditions reach stage (c) as defined above.

#### HEAT OF MOISTURE-HALIDE INTERACTION

Differential scanning calorimetry (DSC) was a technique used in attempting to study the nature of the moisture-halide interaction. Since the heat of the interaction turned out to be lower than 0.05 (mcal/sec) in<sup>-1</sup>, which is the detection limit of the Dupont 990 DSC, the effort did not continue after the initial measurements.



## Section 7

### Development of Combined Protective and Antireflective Coatings: Exploration and Development

**Task:** Explore and develop an advanced total coating system for alkali halides for FLIR applications to perform the functions of both environmental protection and reduction of reflection loss.

The use of alkali halides as optical elements requires layers of suitable coatings that will improve transmission by antireflection and resist damage from a humid environment. The approach to developing a coating system to achieve this objective was to design a multilayer coating system of moisture resistant materials with suitable thicknesses to provide antireflective properties. The coating system consists of a high-index inner layer and a low-index organic outer layer. To provide both high transmission between 8 and 12 $\mu$ m and good protection from the environment, the most promising coating system is As<sub>2</sub>Se<sub>3</sub>/PE/PPE. Thus, the design for antireflection coatings used As<sub>2</sub>Se<sub>3</sub> as a high-index inner layer and PE-PPE as a low index outer layer. Three antireflectance stacks were designed for 10.6 $\mu$ m as detailed in Appendix B. The required thicknesses of each layer in the three designs are:

Coating	Refractive Index	Required Thickness ( $\mu$ m)		
		Design 1	Design 2	Design 3
PE-PPE	1.51	2.1788	1.1042	4.5519
As <sub>2</sub> Se <sub>3</sub>	2.79	0.1972	1.7025	1.7025

The PE-PPE layer can combine the thicknesss of the two components in any ratio so long as the total thickness is correct.

The actual design of this coating and calculation of the transmission was carried out with contractor funds in an effort complementary to the contract work. The transmission of the coatings as a function of wavelength for the three designs is shown in Figure B-1, Appendix B.

Design 1 has the widest bandwidth of the three designs. It satisfies the transmission specification SM-C-773691 (MLAR) for the common modular FLIR. However the thicknesses of the coating layers are rather thin, and this design may provide inadequate environmental protection. The problems of design 2 are the lack of a high transmission at the 8 to 9 $\mu$ m wavelength range and the small thickness of the PE-PPE layer. Design 3 seems to be the best compromise in terms of both transmission and coating thickness, although the transmission near 12 $\mu$ m decreases rapidly.

Another design was a two-layer AR coating peaked for  $9.0\mu\text{m}$ . With TII ( $n=2.4$ ) and PPE or polyethylene ( $n=1.5$ ), an antireflective coating for KBr was obtained. The theoretical transmission of such a coating is shown in Figure 34. Note that this spectrum should result from either a two-layer PPE/TII or a three-layer PPE/PE/TII design. This is important since the best coating tested for moisture protection is the latter one. The total thickness of the organic layers can be built up by any combination of PE and PPE which provides the proper total thickness. The spectrum in Figure 34 also satisfies transmission specification SM-C-773691 (MLAR) for the common modular FLIR. This design does have the problem that the inner high-index layer is not an effective ion barrier—as  $\text{As}_2\text{Se}_3$  is.

In summary, antireflective coatings have been designed for KBr. The coatings provide the proper transmission to meet the FLIR specifications, and utilize the coating materials suitable for environmental protection. Measurements of the antireflection properties of the coatings are described in Section 11.

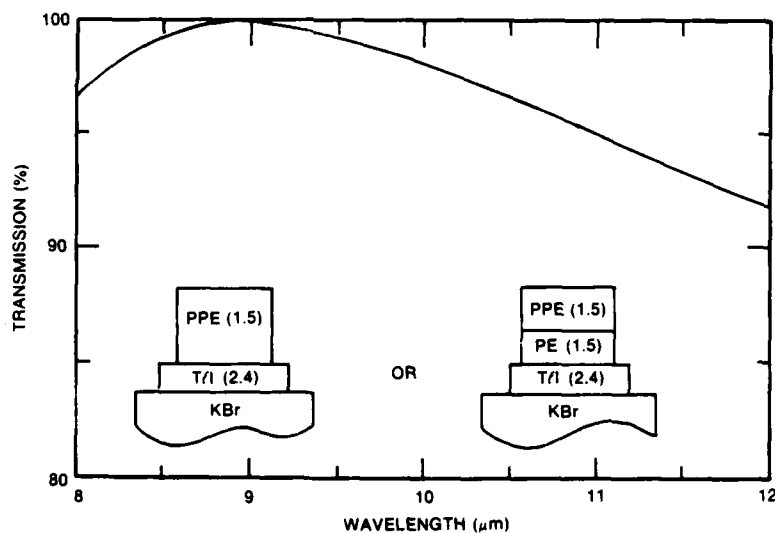


Figure 34. Transmission versus wavelength for the coating designs shown. The refractive indices of the coating materials are given in parentheses. Total thicknesses are  $0.26\mu\text{m}$  for TII and  $2.0\mu\text{m}$  for materials with index 1.5.

## Section 8

### Advanced Testing Methods

**Task: Develop advanced testing methods such as two-wavelength holographic interferometry in single- or double-pass transmission configurations and lateral shearing in single-pass transmission.**

This section reviews the development of interferometric techniques to provide a simple indication of the KBr lens quality. This includes the lateral shearing method and two-wavelength holographic interferometry (TWH) in the transmission mode.

Most of the efforts in advanced optical testing were spent in demonstrating the validity of using lateral shearing interferometry to correlate modulation transfer function (MTF) measurements for KBr lenses with more easily measured quantities.

The forging process is a direct replication method which differs greatly from conventional lapping/polishing for fabricating spherical lenses. The latter process requires a stringent surface figure specification. For the replication process, the thickness of a forged lens is conserved while the individual lens surfaces may warp as the lens cools from the elevated forging temperature. As a result, each surface of the finished lens differs from the design radius of curvature. Yet the errors in the two surfaces will tend to compensate one another to provide good optical quality in transmission. Therefore, the optical figure at the visible wavelength ( $\lambda = 0.63\mu\text{m}$ ) of each surface of a KBr lens is complicated. This would indicate that the element should not be a good lens. However, performance measurements (MTF in an imager) give good results. An alternate approach to evaluating lens performance is desirable.

The following first points out how these forged halide lenses behave in transmission, as compared to that of a ZnSe color corrector in the FLIR imager. Then it describes two methods being developed for the purpose of quality control in forged halide lenses. Because MTF measurements are costly and time-consuming, it is desirable to have an easier evaluation procedure.

#### TESTING LENSES IN TRANSMISSION

To determine how a lens behaves in transmission, the lens can be illuminated with collimated light, with the curved side (or the side with minimum spherical curvature) facing the collimated beam; then the light can be retroreflected with an appropriately curved mirror placed after the lens. In general, if a lens is tested at infinite conjugates, many waves of aberration will be produced. To avoid this problem, one of the following techniques can be used: (1) test the lens at the conjugate for which a perfect lens will produce a small amount of aberration, (2) use a computer-generated hologram (CGH) to remove aberrations produced by a perfect lens, (3) use two-wavelength holography, or (4) use a long-wavelength light source.

To compare the aberrations produced by a perfect lens for a different optical system (or design), Table 3 presents the results of ray-tracing the double-pass transmission test for diffraction-limited lenses of interest.

Table 3. Aberrations of a Perfect Lens

Lens*	Optical Path Difference (waves at 0.63 $\mu$ m)
KBr	1.2
ZnSe	16.7
KCl	29.0
KRS-5 (spherical)	90.1
KRS-5 (aspheric)	187.9

\*Note: All these lenses are designed to form-fit the IR imager for the FLIR system. For all lenses a 2.3-inch-diameter clear aperture was used.

From the result of this ray tracing, the KBr lenses could be tested without using CGH, whereas all the other lenses would require a CGH to subtract many waves of aberration present in the perfect system. The KRS-5 lens does not transmit well in the visible, so a long-wavelength light source would be needed for the test. In this program, efforts were concentrated on developing an interferometric technique which could provide a simple indication for qualifying the KBr lens.

#### DOUBLE-PASS TRANSMISSION USING TWO-WAVELENGTH HOLOGRAPHY (TWH)

J.C. Wyant of the University of Arizona showed that TWH can be used to generate visible fringes that are equivalent to less-sensitive, longer-wavelength fringes for testing aspheric surfaces. This technique employs the beat frequency of two different visible wavelengths to simulate the optical figure at equivalent wavelengths from 6.45 to 47.9 $\mu$ m using an argon-ion laser. A modified Twyman-Green interferometer and an automated thermoplastic holographic camera were assembled, as shown in Figure 35. First record on the hologram the fringe pattern obtained by testing a lens/mirror system at  $\lambda = 0.5145\mu$ m. A new fringe pattern, generated at  $\lambda = 0.488\mu$ m from the same laser, is then used to illuminate the hologram. The resulting pattern is visible but is the same as if it were made by a longer wavelength, an equivalent wavelength  $\lambda_{eq}$ , expressed as

$$\lambda_{eq} = \frac{\lambda_1 \lambda_2}{|\lambda_1 - \lambda_2|} \quad (1)$$

where  $\lambda_1$  and  $\lambda_2$  are the wavelengths used for the exposures. For the example above,  $\lambda_{eq}$  is  $9.47\mu\text{m}$ , which falls in the  $8$  to  $12\mu\text{m}$  region. Since the lens is used in a single-pass transmission mode, the result of errors would be magnified by two times, and yet would be simple enough to interpret. Alternatively, a more direct method would be to use a  $10.6\mu\text{m}$  light source in single-pass transmission. Such infrared interferometers are unusual and expensive.

### LATERAL SHEARING INTERFEROMETER

To reduce the interferometer testing sensitivity further in the visible wavelength region, lateral shearing interferometry can be used. This technique requires a more complicated procedure for the data reduction and does not have a variable sensitivity. However, if the concern is mainly the quality control of the forged KBr lens, a specific interferometer can be designed which will relate the root mean square (rms) error of the fringe pattern to the actual optical performance of the lens. To design such an interferometer, the first consideration must be how the MTF relates to the rms error of an optical system.

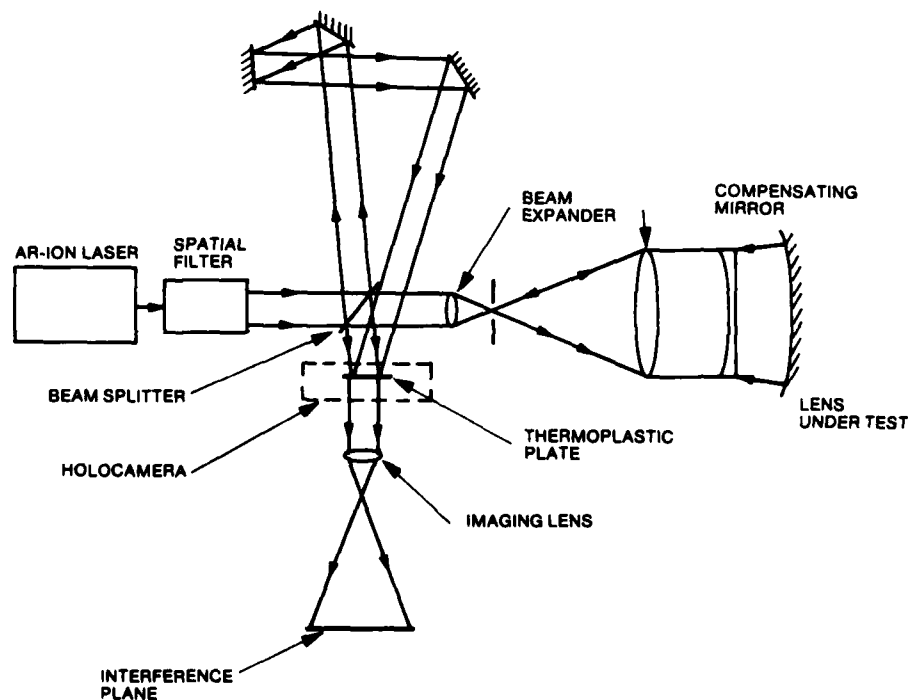


Figure 35. Two-wavelength double-pass holographic testing.

To simplify the testing, it is assumed that all the other components in the FLIR imager are perfect, and the KBr lens is treated as a one-element system. Then the following expression defines a forged KBr lens in terms of the rms error in single-pass transmission at  $10\mu\text{m}$ :

$$\frac{[\text{MTF}]_{\text{forged KBr}}}{[\text{MTF}]_{\text{perfect KBr lens}}} = 1 - 1/2 (\text{rms})^2 \quad (2)$$

where rms denotes the rms error.

Given the specifications for the lens performance

$$[\text{MTF}]_{\text{perfect KBr lens}} = 78\%$$

$$[\text{MTF}]_{\text{forged KBr lens}} = 74\% \text{ (as a minimum).}$$

one can solve for the maximum permissible rms error in terms of the known values,

$$\text{rms} = \sqrt{2 \left[ 1 - \left( \frac{0.74}{0.78} \right) \right]} = 0.316 \text{ radian} \quad (3)$$

$$\approx \lambda/20.$$

In practical experience, the peak-to-valley (PV) error is about five times the rms error in the wavefront. This is an empirical relation, but it is valid for a wide range of conditions. Thus

$$(\text{PV}) = \lambda/4 \quad (4)$$

The maximum permissible peak-to-valley distortion of a  $10\mu\text{m}$  interferogram would be about  $1/4$  wave according to equation (3). For testing in the visible, with a HeNe laser at  $0.64\mu\text{m}$  wavelength, the peak-to-valley distortion would be about four waves, for a barely acceptable lens. This barely acceptable PV wavefront error in the visible using a He-Ne laser, gives a numerical value of  $4\lambda$  (where  $\lambda = 0.6328\mu\text{m}$ ) or 4 fringes wavefront deviation in the interferogram.

To implement this interferometric measurement, a lateral shearing interferometer is used to correlate the MTF performance to the shear. In the actual MTF measurement of the FLIR imager, the on-axis clear aperture is 1.5-inch diameter instead of the 2.3-inch diameter of the entire lens. Also, the MTF value is usually specified at 10 line pair/mm instead of 50 lp/mm for the entire lens.

Therefore, a lateral shear of

$$\Delta X = \frac{10}{50} \times 1.5 \text{ inch} = 0.3 \text{ inch}$$

is required in the lateral shearing interferometer.

To provide such a shear, an optically flat parallel plate of 4-inch diameter by 0.625-inch thickness is used as shown in Figure 36. The tilt angle of the parallel plate is about 40 degrees. A compensating lens with relatively good quality is used to balance the divergence of the KBr lens. In general, a fringe pattern is seen reflected from the parallel plate when a 1.5-inch clear-aperture is used. Slight defocussing can be introduced to minimize the number of fringes in the interferogram. Interferograms of any lens with less than 4 fringes deviation indicate acceptable optical performance of the lens. Otherwise, any lens with a shearing interferogram showing more than 4 fringes deviation is disqualified. A group of KBr lenses were tested using this method and then related to the MTF measurements. Figures 37 through 41 show the shearing interferograms of different forged KBr lenses. The fringe deviation of these lenses and the corresponding MTF data of these lenses are compared in Table 4. These results show excellent correlation between lateral shear fringe deviation and MTF data for typical forged KBr lenses.

In summary, a lateral shearing interferometer using a parallel plate of high optical quality was constructed to test interferometrically the forged KBr lenses. These results show good correlation between the shearing pattern and MTF measurement for a group of forged KBr lenses. The correlation is discussed in detail in Section 9.

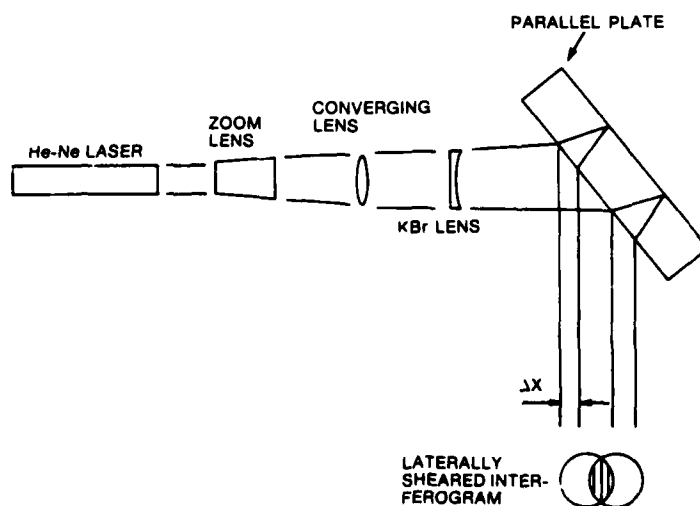


Figure 36. Lateral shearing interferometer.

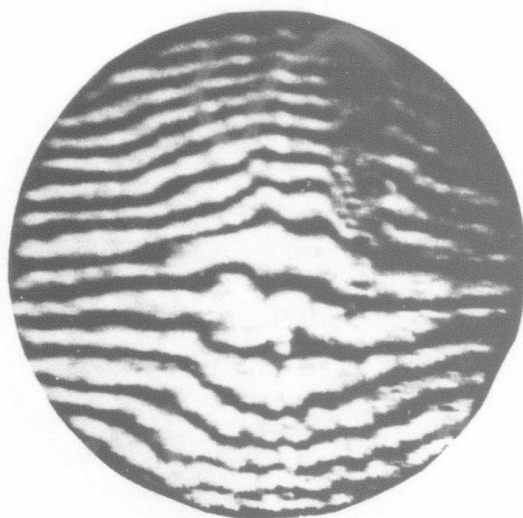


Figure 37. Shearing interferogram for KBr lens 018.

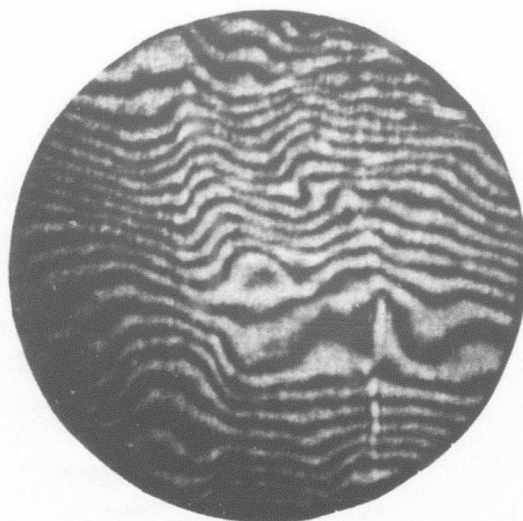


Figure 38. Shearing interferogram for KBr lens 668.



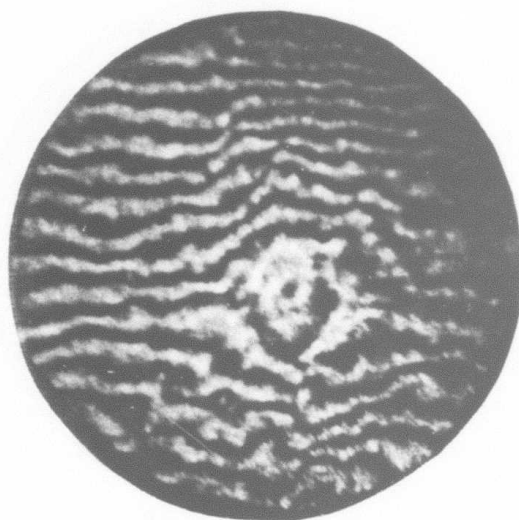


Figure 39. Shearing interferogram for KBr lens 672.



Figure 40. Shearing interferogram for KBr lens 608.

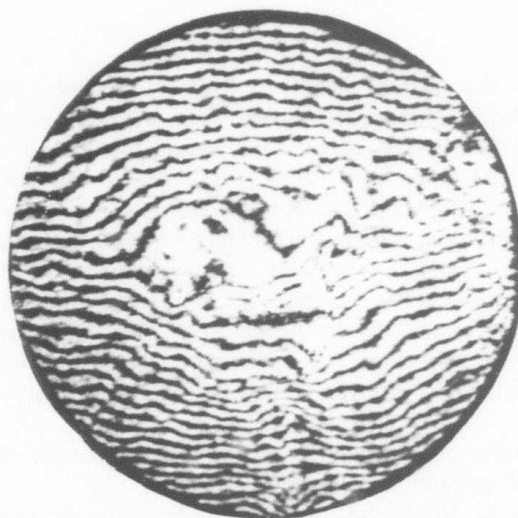


Figure 41. Shearing interferogram for KBr lens 719.

Table 4. Fringe Error versus MTF Measurements for Forged KBr Lenses

KBr Lens	rms Error ( $\lambda$ )	P-V Error ( $\lambda$ )	MTF* (%)
018	0.60	2.77	77.29
608	0.29	3.24	73.83
672	0.65	3.02	73.49
668	0.84	3.54	70.85
719	—	> 4	67.00

\*The MTF measurements were made by the substitution of a KBr lens for the ZnSe color corrector in the IR Imager. All MTF data were obtained at NV&EOL.

## CONCLUSIONS

It is recognized in the optical industry that, in general, lenses fabricated by the conventional lapping/polishing process are often over-specified, especially for components used at infrared wavelengths. FLIR lenses fabricated by replication processes differ greatly in appearance from those produced by conventional processes. A new standard for specifying these optical components is urgently needed. This program has addressed a similar problem and has established a testing method using interferometry for forged IR lenses at a visible wavelength. It was concluded that a simple method like lateral shearing interferometry can be used for testing lenses. To further reduce the sensitivity of this method, it is recommended that an infrared lateral shearing interferometer be used. However, the ultimate testing method and arbitrator of all disputes for the functional performance of the infrared imager should be:

- (1) Observation of a plane wave from an infrared source propagating through the imager. An IR interferometer should be used.
- (2) Measurement of MTF performance of the imager using an infrared optical transfer function instrument.

## Section 9

### Optical Testing

**Task: Perform optical tests on forged lenses using the Honeywell-Tropel holographic interferometer. Develop correlations between results of interferometric testing and performance of the lens as an optical element.**

This section describes application of the lateral shearing interferometer discussed in Section 8. The purpose was to develop a relatively simple low-cost method for inspection of KBr lenses and for prediction of their performance characteristics. There are optical testing tasks also specified under the MM&T contract at Honeywell Ceramics Center. Note that these tasks were distinct and did not overlap the tasks specified in this contract.

The tests on forged lenses on the Honeywell-Tropel interferometer for KRS-5 lenses and KCl lenses forged on this contract were charged to this contract. Tests on forged lenses for KBr lenses forged on the MM&T contract were charged to the MM&T contract. Tests on KBr lenses needed to develop correlations between results of interferometric testing and performance of the lens as an optical element were charged to this contract, although the lenses were supplied from forgings produced under the MM&T contract. Development of the advanced testing methods proceeded under this contract, and they were not used under the MM&T contract. Thus there was no duplication of the optical tests performed under the two contracts.

In this program there was no development of the KBr forging. All modifications to the forging procedure have been under the MM&T program. Evaluating the correlation between MTF and interferometry, a task in the current program, has been done by making measurements on lenses from the MM&T program. Those specific measurements were charged to this program and not to the MM&T program.

#### CORRELATION BETWEEN MTF AND INTERFEROMETRY

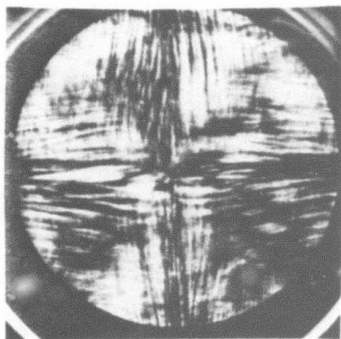
The double-pass transmission test and shearing interferometry are tools for identifying lenses that will cause the imager to pass or fail the MTF requirements. The lab test requirement is to be able to view the interferogram and predict the performance from that view alone. This requires a simple inexpensive setup that is easily operated, with results that are readily definable so that pass or fail is clearly perceived. This type of requirement is necessitated by the optical figures produced on the forged lenses. The optical figures are not straightforward interferograms of spherical surfaces because the lenses do not have very spherical surfaces. The approach is to use a transmission test that includes both sides of the lens at the same time. This is reasonable because both sides of the lens are forged at the same time. If some motion of the surface takes place during cooling, there is a probable opposite motion on the other side which compensates,

resulting in a lens very close to the shape of the dies that formed it. A transmission test will include both of these surfaces, as does the performance test of the imager. The approach is to observe the lenses in both the double-pass transmission and the shearing and then evaluate the lenses in the imager. Conclusions as to the applicability of the tests were accepted when there was a significant correlation between observed interferograms and performance. The technical approach to handling each forging involved cooperation with the MM&T program at the Honeywell Ceramics Center (HCC). This is because there was no KBr forging in this program. The availability of lenses for optical testing was curtailed by this arrangement because we planned to do the final forgings for the MM&T at the Corporate Technology Center, which is where the optical test facility is located. Each lens that is forged needs evaluation which was provided for by MM&T funds. That evaluation was provided by the FLIR team and included polariscope views through the bulk during processing as well as optical figure (both sides), a surface inspection and one or more of the advanced optical tests referred to above. These were provided to HCC on each lens and were charged to their MM&T by our personnel.

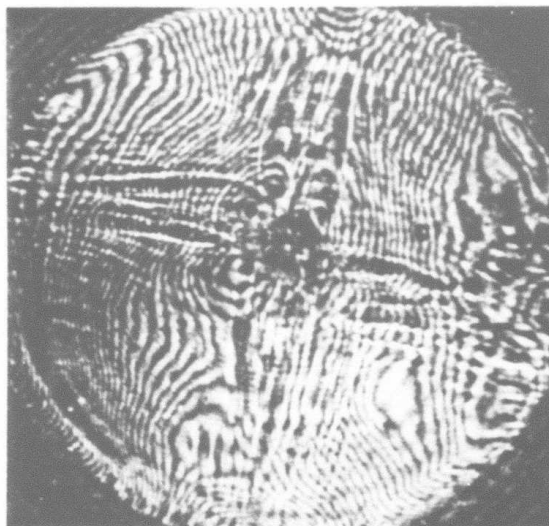
The correlation between MTF and the peak-to-valley deviation of the fringe pattern in lateral shearing interferometer was done using lenses forged under the MM&T program.

Of the 53 lenses, five were evaluated at NV&EOL. Three of the five were run in January 1980 to evaluate the influence of the initial forging parameters on the performance of the final lens. This assumed there were no other variables in the process and that the second stage forging on these three lenses were indeed held within the same procedural tolerances. Forging 038 was done with Teflon® conical dies, from a cylinder and at a high ram rate (0.800 inch/min) and then was final forged at 400 psi. Forging 014 was also forged between conical dies from a cylinder but without Teflon. The final forging pressure on 014 was also 400 psi. Forging 018 was forged from a cube between conical dies also with no Teflon. The final forging on 018 was done at 100 psi. Figure 42 shows sample 014 between crossed polarizers and shows the optical figure of the concave side and the shearing view. All three views show a significant strain in the bulk, which even shows up in the surface reflection.

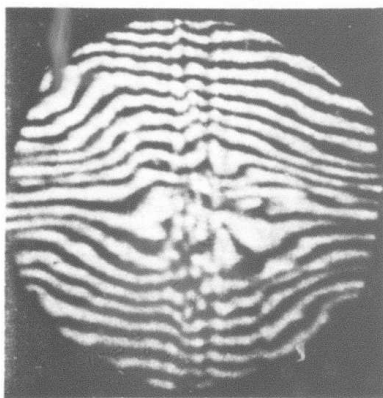
The theory is that the lack of lubricant on the die surface produces the strain. The shearing predicts good performance, however. Figure 43 shows forging 018. The view between crossed polarizers and the optical figure of the concave surface as well as the shearing are shown in this figure. These views show the strain with extra little curls in the crossed polarizer view possibly from starting with a cube and then first forging with no Teflon. The shearing predicted passing performance. Figure 44 shows forging 038 between crossed polarizers and a reflective optical figure of the concave side. These views show no cross but there is a hint of only marginal performance in the shearing. Figure 45 plots the MTF performance of the FLIR imager with forgings 018, 014 and 038 in it. These are the on-axis plots only—the off-axis plots were well above the requirements all the way out to 10 lp/mm. Plotting these three together shows the shearing to be a better predictor than the strain. It also says that with reasonable care the yield on these lenses should approach 100%.



Polariscope

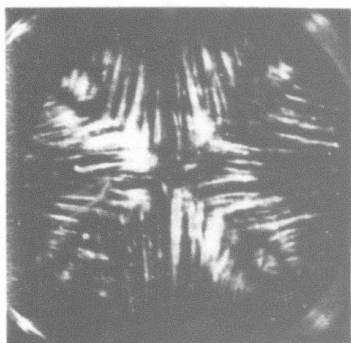


Concave Optical Figure



Shearing

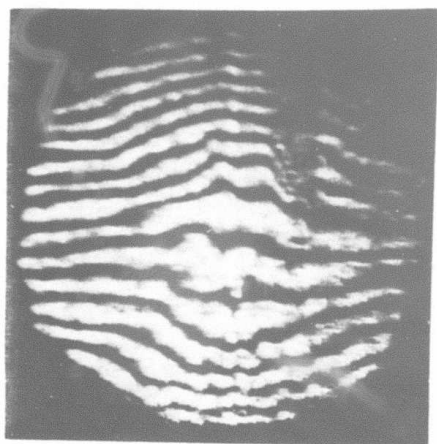
Figure 42. Optical figure, shearing interferogram and polariscope view of KBr lens 014.



Polariscope



Concave Optical Figure

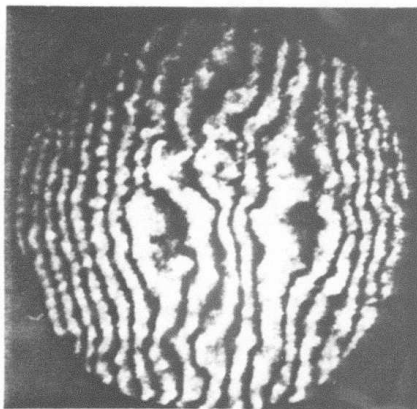


Shearing

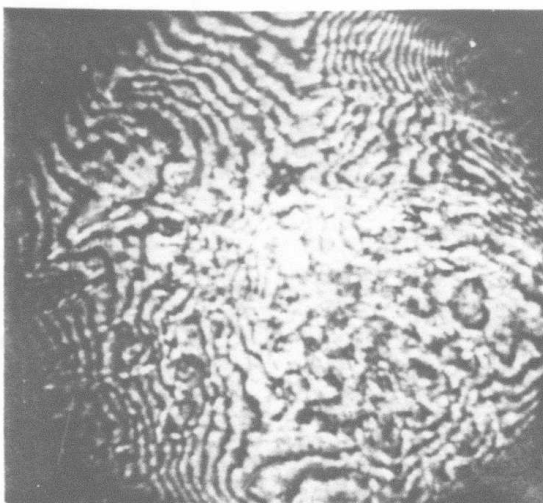
Figure 43. Optical figure, shearing interferogram and polariscope view of KBr lens 018.



Polariscope



Shearing



Concave Optical Figure

Figure 44. Optical figure, shearing interferogram and polariscope view of KBr lens 038.



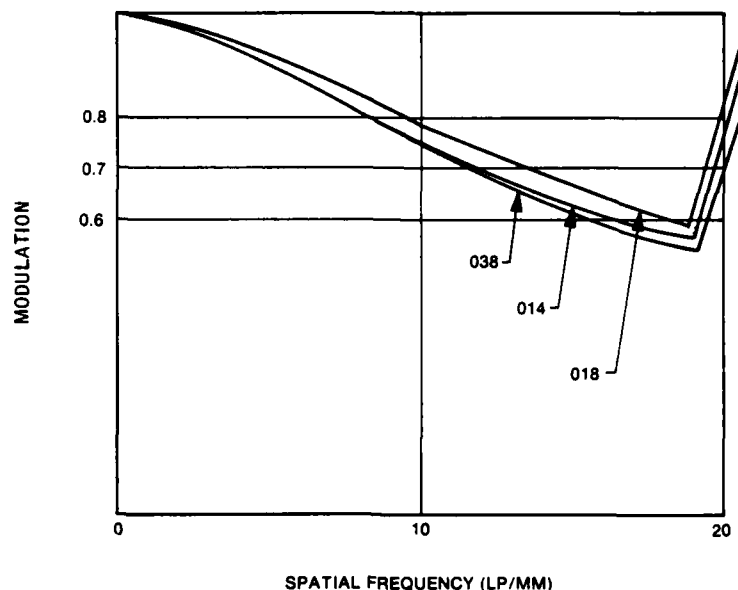
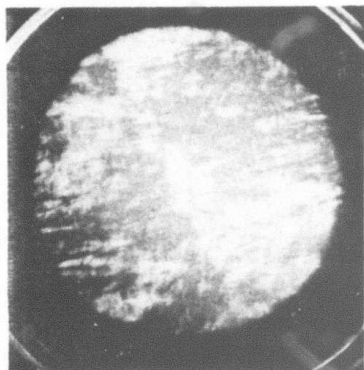


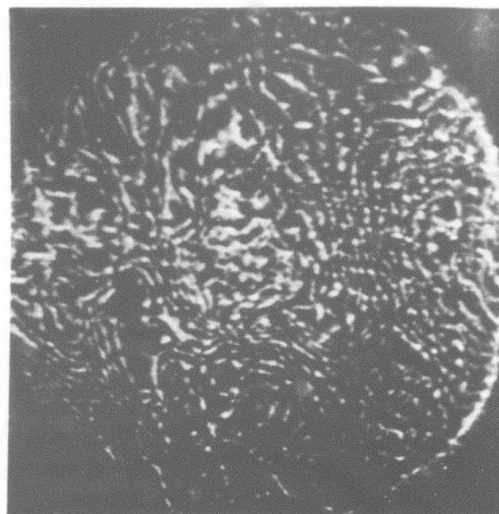
Figure 45. MTF of imager with KBr lenses 014, 018 and 038.

To verify this yield statement every KBr lens forged since the lens design had been changed to 17-inch radius and 0.300 inch thickness, including the MM&T lenses, was checked in the shearing interferometer. Of the 100 lenses surveyed, three lenses showed up poorly. All the rest looked good. Three of the good ones and three particularly poor ones were taken to NVL for MTF testing. Time constraints allowed only one pair to be tested, but that pair confirmed the contention that the shearing test would predict the MTF. This pair was lenses 849 and 719. Figure 46 shows 719 between crossed polarizers, an optical figure of the concave surface and its shearing interferogram. There is no obvious cross in the bulk and the surface figure is complicated but not obviously bad; however, the shearing shows a significant change in frequency implying poor performance. On the other hand, sample 049 shown in Figure 47, shows a similar polariscope view, a nice optical figure and a very well ordered shearing interferogram. Figure 48 plots the MTF performance of these two pass-fail lenses on axis showing that they do indeed pass or fail as the shearing predicts.

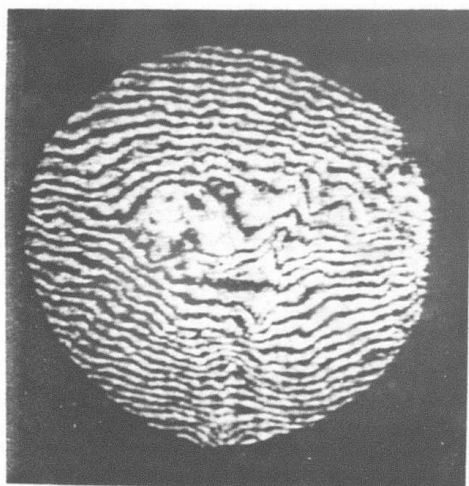
The shearing interferograms in Figures 42 through 47 were digitized and analyzed using the FRINGE computer program from the University of Arizona to give the maximum span of the optical path difference. This has been presented already as the peak-to-valley wavefront distortion in Table 4. The results in Table 4 show that the wavefront distortion in shearing interferometry does correlate with MTF performance, so the interferometry could possibly be used for production inspection.



Polariscope

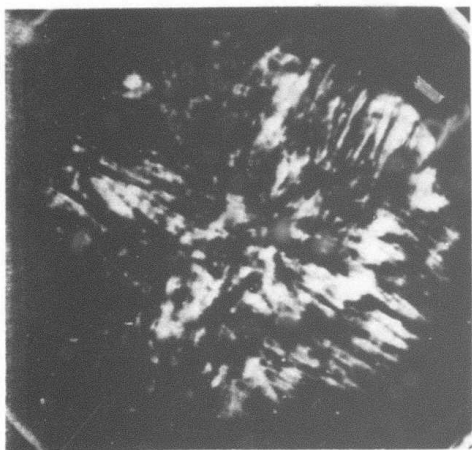


Concave Optical Figure

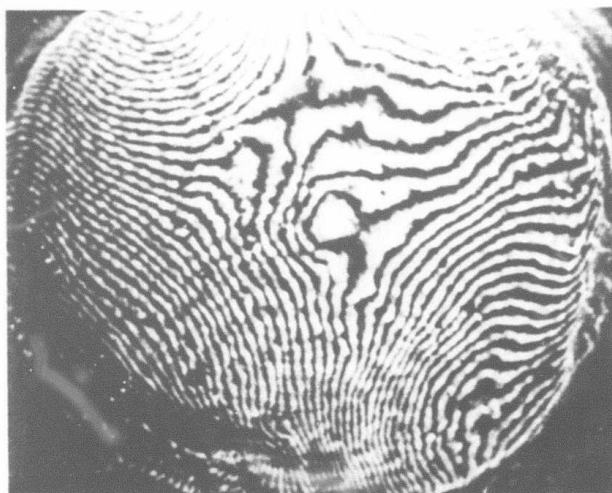


Shearing

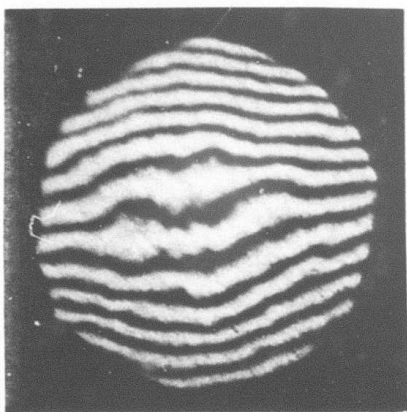
Figure 46. Optical figure, shearing interferogram and polariscope view of KBr lens 719.



Polariscope



Concave Optical Figure



Shearing

Figure 47. Optical figure, shearing interferogram and polariscope view of KBr lens 049.

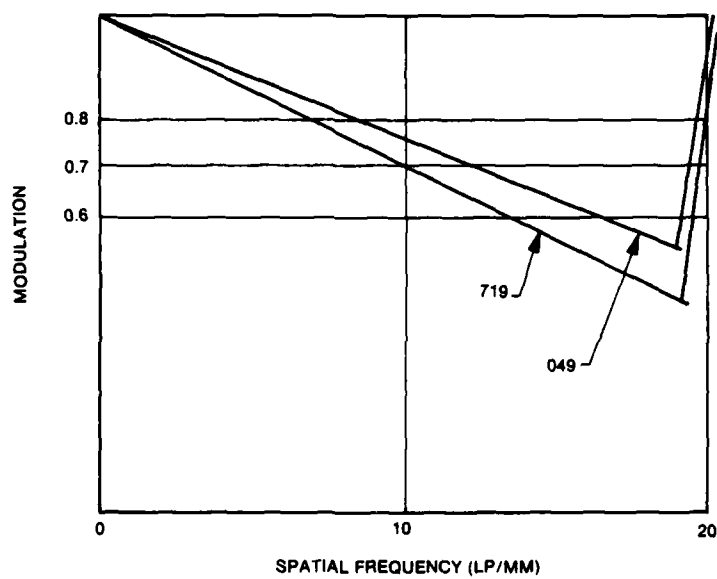


Figure 48. MTF of imager with KBr lenses 049 and 719.

## Section 10

### Development of Protective Coatings for KBr

**Task: Optimize coating procedures for the coating systems  $\text{As}_2\text{Se}_3$ /polyethylene (PE)/plasma-polymerized ethane (PPE) and Ge/TiI/PE/PPE to produce defect-free coatings and to demonstrate the maximum capabilities of these systems for the protection of polycrystalline KBr.**

Earlier sections, especially Sections 2 and 7, described the choice of coating system: inorganic thin film, polyethylene (PE), and plasma-polymerized ethane (PPE). The inorganic material, like  $\text{As}_2\text{Se}_3$ , is chosen as an ion barrier and also to have an index of refraction suitable for a combined protective and antireflective coating. The dense crystalline PE and pinhole-free PPE provide a continuous barrier to water vapor. Control of the deposition of the PPE leads to a total thickness of organic material suitable for the antireflection properties.

Section 2 described temperature humidity cycling of alkali halides with this coating. The coatings failed in isolated spots because of defects in the coating layers. To optimize the coating process, improvement of coating procedures leading toward defect-free coatings was emphasized.

The inorganic layer is deposited by thermal deposition, according to methods developed earlier<sup>(1)</sup>. This leads to uniform essentially defect-free layers.

Alkali halide samples, previously coated with  $\text{As}_2\text{Se}_3$  and polyethylene, were coated with plasma polymerized ethane (PPE) in an RF diode parallel-plate electrode system (GCA Corp., Vacuum Industries, Inc.). This system was modified (as described in Section 2) to improve the uniformity of the coating of more and larger samples. As a result, uniform pinhole-free coatings of PPE with controllable thickness were readily available.

The intermediate layer of the three-layer antireflective coating design is polyethylene (PE), an inert plastic material which, in thin layers ( $1.5\mu\text{m}$ ), can aid in meeting the antireflective and transmission requirements while providing environmental protection for alkali halides. In the early work, coating failures were often associated with defects in the PE layer. Accordingly, most of the emphasis went to improvement of the PE. A spin coating procedure was developed to replace the dip coating described earlier.

In the spin coating procedure, the substrate is placed in a fixture which holds the substrate in place by three narrow legs. Below the substrate is placed a disc which is also held in place by this rotatable fixture. This disc is necessary to ensure uniform, smooth coverage of the lower sample surface during spinning. Figure 49 shows four of these fixtures used for various-diameter substrates or lenses. The fixtures are adjusted with two screws to close and hold the sample and the disc during immersion and rotation. The sample was placed in the fixture and then preheated in an oven to  $100^\circ\text{C}$  prior to placement in the spin coating system.

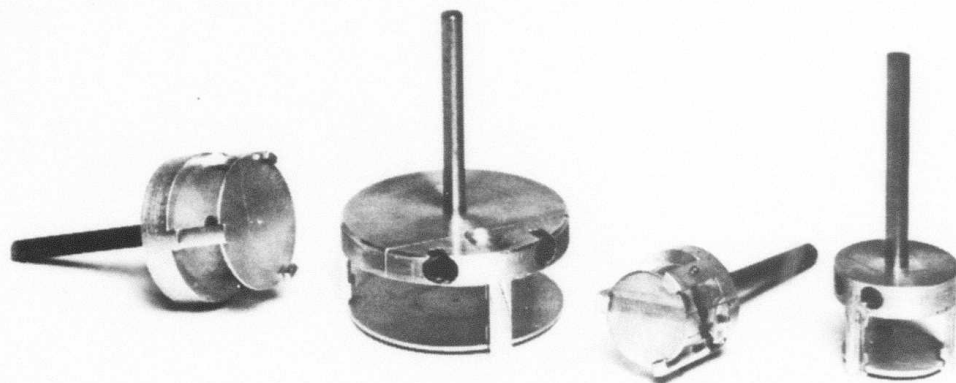


Figure 49. An assortment of spin coating fixtures.

Three grams of PE are dissolved in 150cc of xylene heated to 100°C. A heatable magnetic stirrer is used to assure mixing. The solution is contained in a stoppered flask during heating and stirring. After the PE is dissolved, the heated solution is decanted into a pyrex vessel inside the coating chamber.

Figure 50 is a sectional schematic of the spin coating system. A stirring motor is mounted on a mechanism with parallel shafts that permit vertical movement. This assembly is counterbalanced to stay in the upward position. The preheated fixture is removed from the oven and placed in the chuck which can be seen holding the shaft of the fixture. The cover to the coating chamber is removed, the stirring motor and fixture combinations are lowered, and the fixture enters the coating chamber. The coating chamber is formed by a steel tube about 11 inches in diameter and by an 8-inch-thick disc of Asbestolux® covered by a Lucite® disc. An exhaust air duct is shown on the right side to remove xylene vapor and promote evaporation. As the fixture approaches the inner cover, the covered heater is opened, exposing the heated Pyrex® vessel containing the PE-xylene solution. The fixture and stirring motor are tilted 5 degrees to the horizontal to ensure the escape of bubbles during submersion of the sample. The sample is immersed for 10 seconds, rapidly lifted from the solution, and then rotated for 30 seconds at 1650 rpm. The sample can be reimmersed a number of times to permit the accumulation of PE to the desired thickness. Figure 51 is a photo of the spin coating system. The fixture is shown suspended above the heated vessel for the xylene solution.

After coating, the sample is removed from the fixture and placed in a preheated (100°C) oven. This oven is purged with dry nitrogen to prevent oxidation of the film during subsequent heating and curing. It is slowly evacuated over 4 hours to permit the escape of xylene from the film. The temperature is then slowly increased to 130°C and held for 2 hours. The oven is then turned off and the sample allowed to cool. The sample is then ready for further processing or testing.



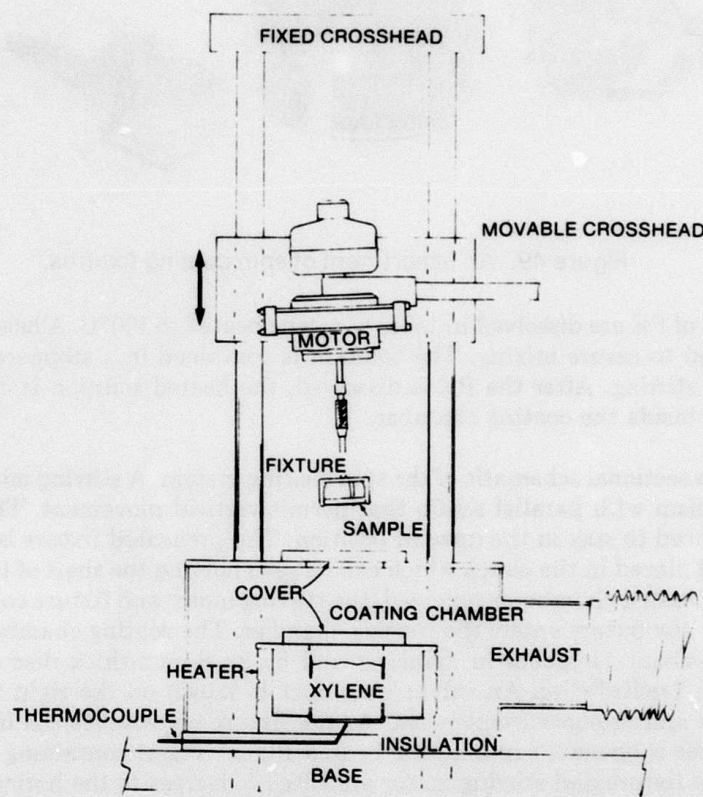


Figure 50. Schematic diagram of the spin coater.

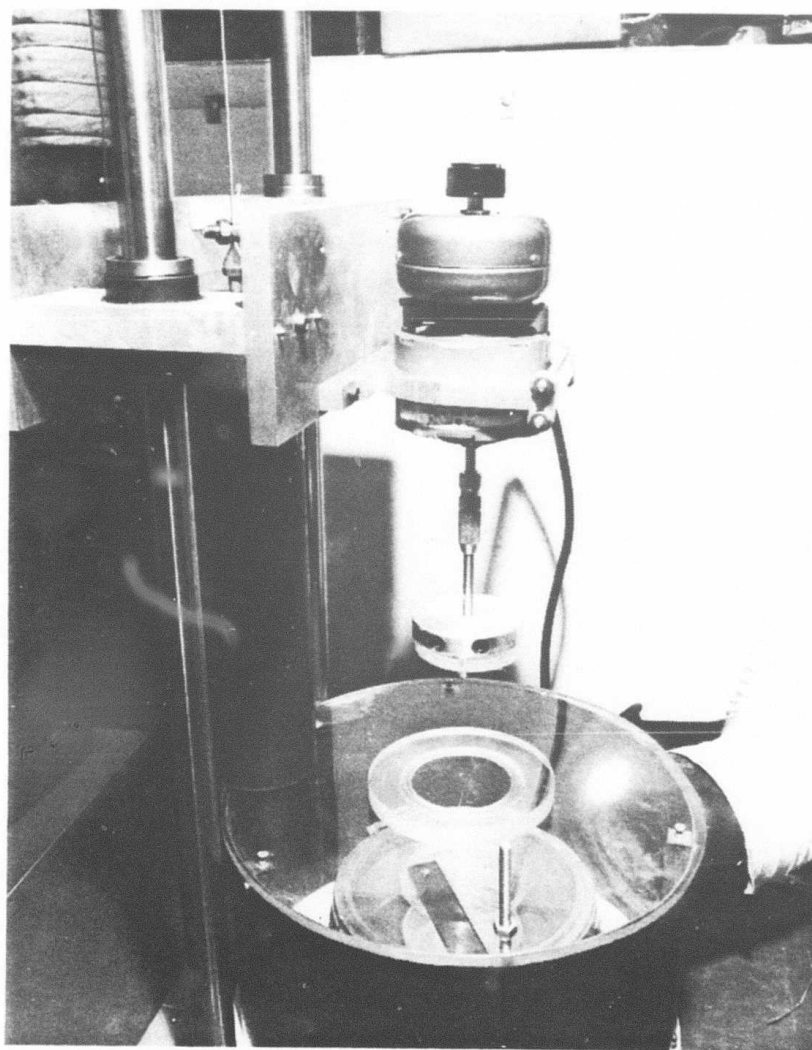


Figure 51. The spin coating system with coating fixture.



To determine the thickness of the accumulation of PE layers, test samples were immersed in liquid nitrogen and then cleaved. The cleaved surface was examined on the scanning electron microscope. Micrographs of coating thicknesses as a function of coating parameters are shown in Figure 52. It was found that, with eight layers and no air exhaust, the accumulated thickness of PE was  $1.4\mu\text{m}$ . When the air exhaust from the coating chamber is increased, the partial pressure of xylene is reduced, and the thickness of the PE deposit is increased. However, with increasing deposition thickness, the surface quality deteriorates in appearance because of the development of radial stria indicating slight thickness variations in the deposit. By using minimal air exhaust, the thickness of each layer was increased to  $0.3\mu\text{m}$  with minimal surface stria.

The spin coating system was used to produce samples for humidity testing to determine the maximum capabilities of the coating for environmental protection of KBr.

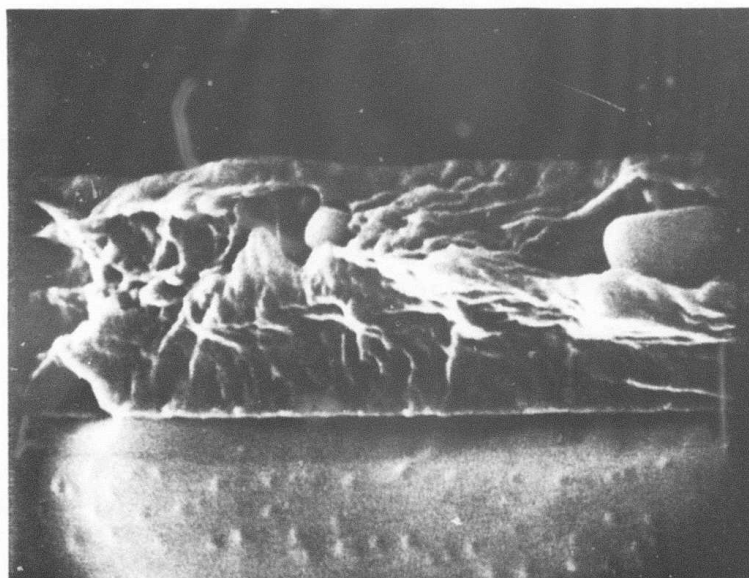
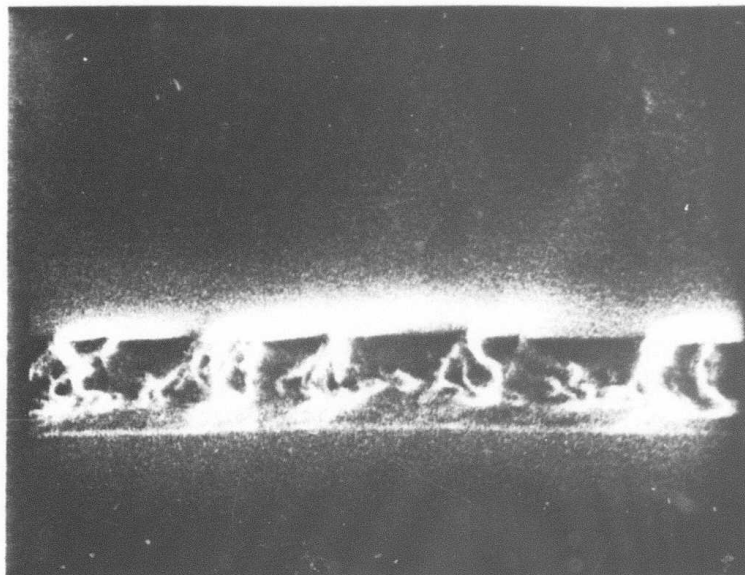


Figure 52. Spin coating samples:  $1\mu\text{m} = 1\text{ cm}$  at 10,000X; (a) eight layers with no air flow; (b) twelve layers with low air flow.

## Section 11

### Development of Combined Protective and Antireflective Coatings: Measurement

**Task:** By varying the thicknesses of the layers in the coating systems and measuring the IR transmission, develop a coating which has both protective and antireflection functions for KBr.

Section 7 described the design of an antireflective (AR) coating for KBr, using materials suitable for moisture protection. In accordance with the design, a forged KBr disc coated with  $\text{As}_2\text{Se}_3$  of  $0.1972\mu\text{m}$  thickness was used to test the theoretical AR design (Design 1 of Figure B-1). Figure 53 shows the infrared spectrum of the sample prior to the PPE coating. The sample was then coated with PPE, with the coating thickness being built up in steps in successive depositions.

The Digilab Fourier transform spectrometer was used to measure the IR spectrum. The infrared transmission was measured after each PPE deposition. Figure 54 shows the spectrum after one 10-minute deposition of PPE, which would have deposited a PPE layer about  $0.25\mu\text{m}$  thick. There was no significant change in the spectrum.

The spectrum did begin to change as later depositions increased the total PPE thickness. After the third 10-minute deposition, an antireflection peak had clearly emerged near  $4\mu\text{m}$  (Figure 55). As the total PPE thickness increased, the antireflection peak shifted to longer wavelengths. Figure 56 shows the spectrum after the sixth deposition, when the peak was near  $6\mu\text{m}$ .

The optimum conditions occurred after the ninth deposition (Figure 57). The antireflection peak is near  $9\mu\text{m}$ . With further depositions, the peak shifted to still longer wavelengths, and transmission in the  $8$  to  $12\mu\text{m}$  region decreased.

These results show clearly that the  $\text{As}_2\text{Se}_3$ /PPE coating, which is formed from materials useful for moisture protection, has strong antireflective properties when the coating thickness is optimized.

Before the PPE coating, the transmission over the  $8$  to  $12\mu\text{m}$  wavelength region was  $77\%$  to  $83\%$ . After the PPE thickness was built up to the optimum level, the transmission was improved to  $86\%$  to  $91\%$  (Figure 57). Only one side was coated, so there was a  $4\%$  loss due to reflection from the uncoated surface. The result shows achievement of a coating that serves both the needs of antireflection and environmental protection.

An even more direct demonstration of the antireflective properties was obtained by direct measurement of the reflection from one surface. The Fourier transform spectrometer was used in its reflectance mode. The reflectance of only the coated side was obtained.

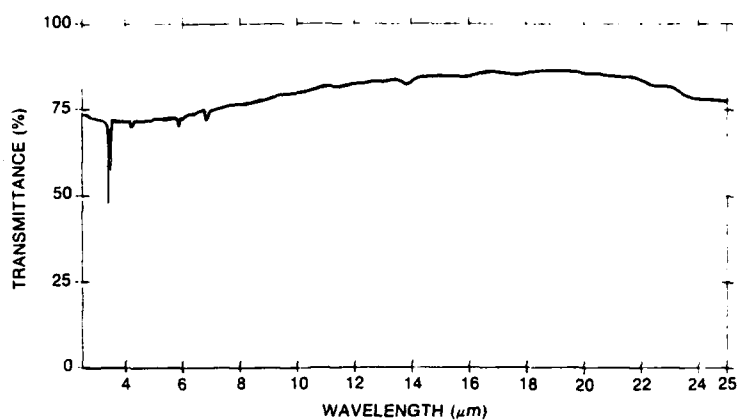


Figure 53 Transmittance of KBr sample without PPE.

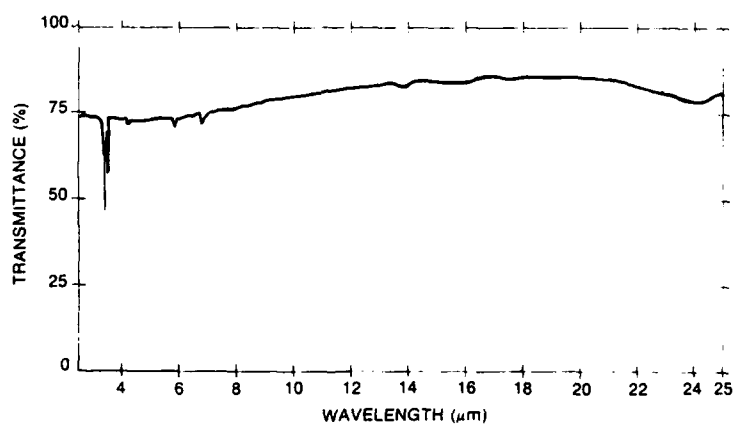


Figure 54. Transmittance of KBr sample after one 10-minute deposition of PPE.

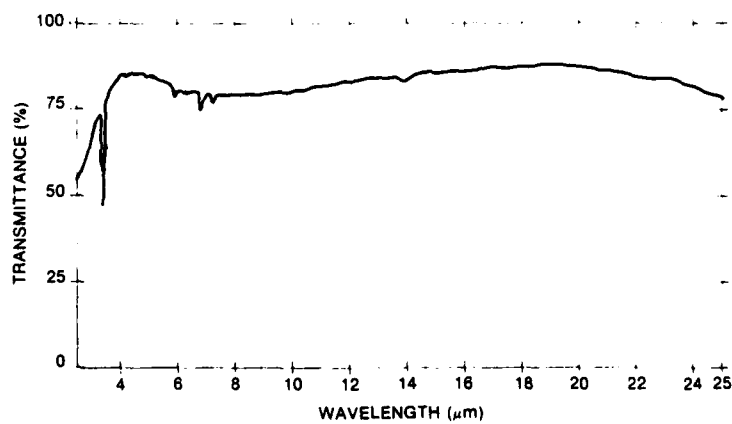


Figure 55. Transmittance of KBr sample after three 10-minute depositions of PPE

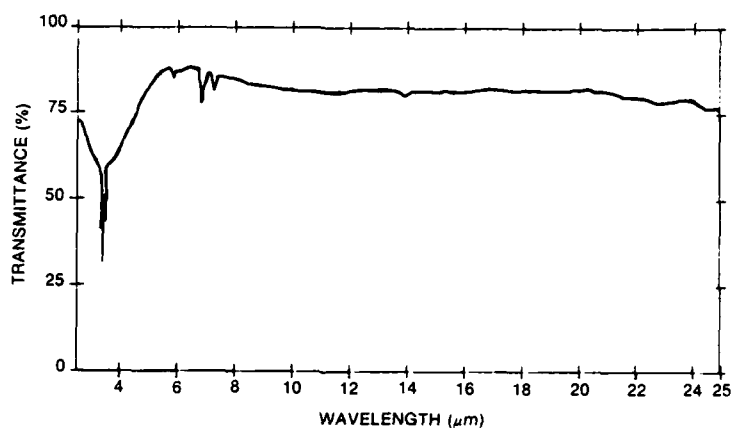


Figure 56 .Transmittance of KBr sample after six 10-minute depositions of PPE.

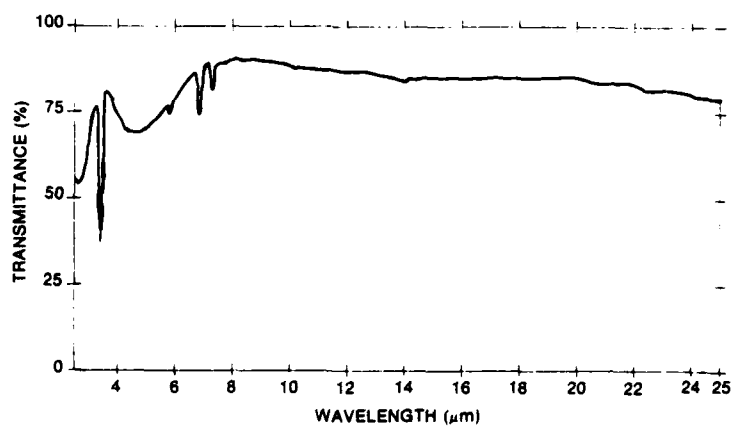


Figure 57. Transmittance of KBr sample after nine 10-minute depositions of PPE.

The effect of the uncoated side was removed by a standard prism-with-index-matching-fluid technique. The reflectivity was reduced below the required limits (2% per surface at  $8\mu\text{m}$ ) to obtain the transmission required for the common modular FLIR. Figure 58 shows reflectance versus wavelength for the forged KBr surface coated with  $0.1972\mu\text{m}$  of  $\text{As}_2\text{Se}_3$  and nine 10-minute depositions of PPE (the same conditions as in Figure 57). The reflectance near  $9\mu\text{m}$  is less than 1%.

These results show that the performance predicted for the coating designs (Section 7) can be achieved in practice with these combination organic/inorganic coatings.

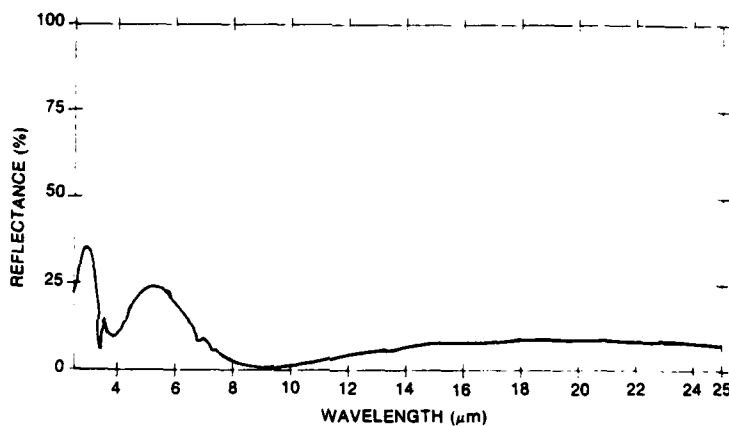


Figure 58. Reflectance of KBr after nine 10-minute depositions of PPE.

## Section 12

### Environmental Testing on Coated KBr

**Task:** Perform environmental tests on coated polycrystalline KBr, including tests for resistance to humidity, severe humidity and fungus, according to the methods of Mil-Std-810B. Determine the extent to which the coating systems can provide environmental protection for KBr.

#### SAMPLE PREPARATION

Forged KBr substrates were coated with vacuum deposited KCl, vacuum deposited  $\text{As}_2\text{Se}_3$ , dip-and-spin coated polyethylene (PE), and plasma polymerized ethane (PPE).

Each of the layers has its own purpose. KCl was deposited in a very thin layer ( $0.10\mu\text{m}$ ) on forged KBr in order to cover the highly moisture sensitive KBr with a slightly less moisture-sensitive material.

The  $\text{As}_2\text{Se}_3$  layer has multiple purposes:

- It is the high index layer in an antireflective coating.
- It is a barrier for potassium ion penetration.
- It provides an adherent support for the PE layer.

The PE layer is the major moisture-resistant layer and has excellent flexibility during humidity testing.

The PPE layer is another moisture-resistant layer. Its major advantage is absence of pin-holes; this is not true for the PE layer. Therefore, the PPE layer provides a sealcoat for the PE layer.

A series of coated forged PBr samples of the following designs were prepared for humidity testing purposes:

- (a) KBr (forged),  $0.1\mu\text{m}$  KCl,  $0.19\mu\text{m}$   $\text{As}_2\text{Se}_3$ ,  $1.4\mu\text{m}$  PE,  $0.8\mu\text{m}$  PPE
- (b) KBr (forged),  $0.16\text{-}0.28\mu\text{m}$   $\text{As}_2\text{Se}_3$ ,  $1.4\mu\text{m}$  PE,  $3.5\mu\text{m}$  PPE
- (c) KBr (forged),  $0.1\mu\text{m}$  KCl,  $1.7\mu\text{m}$   $\text{As}_2\text{Se}_3$ ,  $1.4\mu\text{m}$  PE,  $3.5\mu\text{m}$  PPE
- (d) KBr (forged),  $0.1\mu\text{m}$  KCl,  $1.7\mu\text{m}$   $\text{As}_2\text{Se}_3$ ,  $3.5\mu\text{m}$  PE,  $1.2\mu\text{m}$  PPE

Early experience showed an inability to protect the outside circular perimeters of coated alkali halide samples from moisture penetration even during an early phase of the humidity testing. To eliminate this problem, Torr-Seal® (Varian Associates, Vacuum Division) was applied around sample perimeters and cured 1 hour at 50° to 60°C. Since only one flat side of each sample was coated and tested, the opposite flat side was protected by placing each sample on a blackened (black acrylic spray paint) piece of aluminum foil, and applying Torr-Seal® described above. At the same time sample codes were inscribed into the uncured sealing material.

When the protected samples were tested at higher temperatures, e.g., 71°C, alkali halide crystals appeared at the sealant-coating boundary first, indicating that the coating may be ruptured at this place even before humidity tests. Therefore, a more elastic sealant, Dow Corning 93-076 Aerospace Sealant®, a two part silicone material with excellent tensile strength and resistance to moisture, was selected. Ten parts of the base and one part of the catalyst were mixed, and the mixture was applied to the samples as already described. The samples were then cured at room temperature for 24 hours. However, the problem of alkali halide crystals at the sealant-coating boundary was not eliminated in all tested samples.

#### **HUMIDITY TESTING**

Humidity testing was performed under two sets of conditions:

- 25°C and 88% relative humidity (RH).
- 50°C and 81% relative humidity (RH).

Both sets of test conditions lie in the region in which the kinetics of moisture attack do not involve surface dissolution, as described in Section 6.

For the first set of conditions (25°C and 88% RH) above, the humidity tests were done in a desiccator-like jacketed glass vessel. A constant temperature of 25°C was maintained by circulating water at the same temperature through the jacket. A saturated solution of sodium carbonate provided a constant relative humidity of 88% at 25°C<sup>(5)</sup>. Coated alkali halide (single-crystalline and forged KBr) samples to be tested were placed on the perforated plate seated 2 to 3 cm from the surface of the saturated sodium carbonate solution. Use of glass walls and lid made it possible to inspect the samples without lifting the lid and taking the samples out.

For the second set of test conditions (50°C and 81% RH) a dessicator was placed in an oven in which the temperature was maintained at 50° ± 0.5°C. The constant 81% RH at 50°C was provided by a saturated solution of ammonium sulfate<sup>(5)</sup>.

To avoid condensation of water vapor on cold samples when they were placed in the desiccator, the samples were first preheated for 1 hour in the same oven and then transferred to the dessicator for humidity testing.



The following discussion summarizes the combinations of samples and test conditions.

- **KBr (forged), 0.16 to 0.28 $\mu$ m As<sub>2</sub>Se<sub>3</sub>, 1.4 to 1.5 $\mu$ m PE, 3.5 $\mu$ m PPE tested at 25°C and 88% RH** — Six samples were tested. None of them had a thin KCl layer between the forged KBr and the vacuum deposited As<sub>2</sub>Se<sub>3</sub>. Two samples were sealed with Torr-Seal®, two with the two-part silicone sealant and two were not sealed.

Samples without sealed perimeters wrinkled during the second 24-hour period; all other samples but one (0.20 $\mu$ m As<sub>2</sub>Se<sub>3</sub>) sealed with Torr-Seal® developed surface roughness during the third day of exposure. All samples were removed from the test chamber after the fourth day, allowed to dry, and inspected. The surface of only one sample remained smooth. Other samples had different degrees of surface roughness. All surfaces were practically free of KBr crystals.

The samples were then tested two more days. The only sample that was smooth after 4 days of testing still remained smooth. All samples had a few tiny KBr crystals, the smooth sample having fewer than the others. However, the onset of three "craters" could be noticed on that sample. These samples were not tested further.

- **KBr (forged), 0.1 $\mu$ m KCl, 0.19 $\mu$ m As<sub>2</sub>Se<sub>3</sub>, 1.4 $\mu$ m PE, 0.8 $\mu$ m PPE tested at 50°C and 81% RH** — The samples began to show signs of failing, in the form of droplets on the sample surface, after approximately 20 hours. Humidity testing was stopped after 58 hours. The surface was allowed to dry. After drying, it was without wrinkles or roughness but there were many KBr crystals which had grown through the coating.
- **KBr (forged), 0.1 $\mu$ m KCl, 1.7 $\mu$ m As<sub>2</sub>Se<sub>3</sub>, 3.5 $\mu$ m PE, 1.2 $\mu$ m PPE tested at 50°C and 81% RH** — There were no visible signs of failing after 58 hours of humidity testing. The surface of the tested sample (after drying) was smooth with only one small rough spot. There were no KBr crystals on the sample surface.

This sample was further tested by method 507, procedure I, of Mil-Std-810B as described below.

#### SECURE HUMIDITY TESTING

The severe humidity tests were carried out according to method 507, procedure I, of Mil-Std-810B. This procedure calls for a 10-day temperature humidity cycle, reaching 71°C and 95% RH as the peak values in each 24-hour portion of the cycle. Under these conditions, the kinetics of moisture attack involve dissolution of the surface, as Section 6 described.

These tests were performed in an automated Thermotron Model SM-8C, temperature/humidity test chamber. The conditions used during the humidity testing are shown in Figure 59 and Table 5. The values given in the figure and the table are for one 24-hour portion of the 10-day cycle.

During the humidity testing, especially during intervals 1 and 2, water vapor condensed on all interior surfaces of the chamber, including the sample support rack. Also, heavy rain from the ceiling occurred.

Coated alkali halide samples were covered with condensation during intervals 1, 2, and 3. It is probable that during interval 1, when the temperature of the chamber is increasing, there is a lag in the temperature of alkali halide samples with respect to the temperature of the chamber due to their low thermal conductivity. This could cause additional condensation. Therefore, during the most severe phase of the humidity cycle, coated alkali halide samples were practically covered with liquid water and exposed to rain from the ceiling. The latter problem was partially solved by roofing the samples with a 3M paper facial mask which prevented falling from the ceiling to hit the samples.

The first humidity tests using method 507, procedure I, of Mil-Std-810B indicated that no coated alkali halide samples would survive prolonged exposure to conditions in which the samples were immersed in liquid water. To find out the protective capabilities of coated alkali halide samples with respect to humidity, method 507, procedure I, of Mil-Std-810B was modified as shown in Table 6.

The modification in the procedure was done in intervals 1 to 3, and only slightly in interval 4. Other intervals are identical to the ones in the original method.

During the humidity testing in this modified method, the condensation of water vapor did not occur on coated surfaces. This was confirmed by visual observation that the surfaces remained shiny.

Thus, this modification kept the samples from being covered by liquid water.

Previously during temperature-humidity cycling according to the methods of Mil-Std-810B pinholes were patched as they appeared (see Section 2) and, with such patching, large areas of the coating remained unblemished after as many as 10 cycles. In this series of tests, the initial evidences of developing defects, such as pinholes or craters, were interpreted as coating failure.

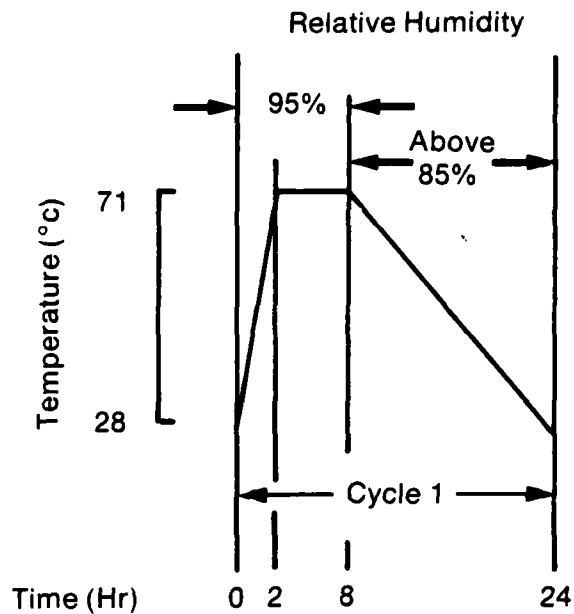


Figure 59. One temperature humidity cycle of method 507, Mil-Std-810B.

Table 5. Conditions for Severe Humidity Test

Interval	Temperature (°C) (Dry Bulb/Wet Bulb)		% RH (final)	Interval Time (hr)	Cumulative Time (hr)
	Start	Finish			
A	22/20	28/27	93	2	-2
1	28/27	71/70	95	2	2
2	71/70	71/70	95	6	8
3	71/70	71/68	87	0.5	8.5
4	71/68	60/57	86	3.5	12
5	60/57	49/46.5	86	4	16
6	49/46.5	38/35.5	85	4	20
7	38/35.5	28/26	86	4	24
8	Back to interval 1.				

One 24-hour Cycle

Table 6. Modified Severe Humidity Test

Interval	Temperature (°C) (Dry Bulb/Wet Bulb)		% RH (final)	Interval Time (min)	Cumulative Time (hr)
	Start	Finish			
A	22/18	22/18	68	30	-1.0
B	22/18	28/25	79	30	-0.5
1	28/25	71/66	80	120	2
2	71/66	71/68	87	30	2.5
3	71/68	71/68	87	330	8.0
4	71/68	60/57	86	240	12
5	60/57	49/46.5	86	240	16
6	49/46.5	38/35.5	85	240	20
7	38/35.5	28/25	79	240	24
8	Back to interval 3				

One 24-hour Cycle

The results of the combinations of samples and test conditions follow:

- **KBr (forged), 0.1 $\mu$ m KCl, 1.7 $\mu$ m As<sub>2</sub>Se<sub>3</sub>, 2.5 $\mu$ m PE, 1.2 $\mu$ m PPE tested by method 507, procedure I, of Mil-Std-810B** — Two samples were tested at the same time. One of them had been tested previously for 58 hours at 50°C and 81% RH as described above.

During the first cycle the sample previously tested at 50°C and 81% RH wrinkled. Some of the largest wrinkles seemed to be full of water. The wrinkles did not disappear when the sample was taken out of the humidity chamber and allowed to dry. At the sealant-coating interface, the coating was cracked. That part of the coating was covered with KBr crystals. However, the remaining portion of the surface area of the sample was free from KBr crystals. There were also large areas without wrinkles. KBr crystals at the coating perimeter were carefully removed with a Q-Tip® and the sample was returned to the humidity chamber for another cycle. During the second cycle the sample developed more wrinkles. At the Torr-Seal®-coating boundary, deep grooves were formed. Also crystals could be seen on the dry sample after it was allowed to dry after second cycle.

The other sample had a smooth surface after the first cycle; there were neither wrinkles nor KBr crystals. During the second cycle, after condensed water vapor had evaporated from the sample, small water droplets were visible on the sample as a first sign of failure. After the second cycle, the sample had several small craters, but there were neither wrinkles nor KBr crystals. Further humidity testing of this sample was stopped.

- **KBr (forged), 0.1 $\mu$ m KCl, 1.7 $\mu$ m As<sub>2</sub>Se<sub>3</sub>, 1.4 $\mu$ m PE, 3.5 $\mu$ m PPE tested by the modified method 507, procedure I of Mil-Std-810B** — Two samples were tested separately. There was no water vapor condensation on the samples during any period of humidity testing. This was the purpose of the modification of method 507, procedure I, of Mil-Std-810B.

During the first cycle one of the samples became slightly swollen and two or three wrinkles were formed. The sample was not removed after the first cycle for inspection. During the second cycle the appearance did not change. After being taken out of the humidity chamber and allowed to dry, the sample showed cracks and deep grooves at the Torr Seal-coating interface. In the remaining portion of the surface area, there were a few wrinkles, one 1mm "crater", and several tiny craters. KBr crystals were almost nonexistent.

To avoid cracks of the coating at the contact with Torr-Seal®, Dow Corning 93-076 Aerospace Sealant® was used for sealing the perimeter of the second sample.

During the first cycle this sample wrinkled slightly, but no other changes occurred. The sample was not taken out at the end of the first cycle. During the second cycle no further changes were noticed. After the second cycle, the dried sample had a few short wrinkles concentrated in three areas, but the remaining surface area was smooth. There were no KBr crystals on the surface. Also, there were no cracks at the sealant-coating interface except for one 5mm-long segment.

- **KBr (forged), 0.26 $\mu$ m As<sub>2</sub>Se<sub>3</sub>, 1.4 $\mu$ m PE, 3.5 $\mu$ m PPE tested by the modified method 507, procedure I, of Mil-Std-810B** — The perimeter of the sample to be tested was sealed with the silicone sealant.

During the first cycle the coating surface wrinkled. The sample was taken out of the humidity chamber after the second cycle. The coating and the sample itself were heavily damaged, with numerous large and deep holes and also with long lines. It is interesting that one large area (approximately one-fifth of the total surface area) remained undamaged and had almost no wrinkles.

It was concluded from these tests that the thin antireflective coating design ( $0.19\mu\text{m}$   $\text{As}_2\text{Se}_3$ ,  $2.3\mu\text{m}$  PE + PPE) on forged KBr has no chance to survive humidity testing at high temperature and high relative humidity for any measurable period of time. The thicker antireflective coating design ( $1.7\mu\text{m}$   $\text{As}_2\text{Se}_3$ ,  $4.7\mu\text{m}$  PE + PPE) on forged KBr can survive at least one high-temperature-high-humidity cycle and more than six days at lower temperature-medium high humidity.

Better results (no wrinkles) are obtained if the PE thickness is greater than the PPE thickness, but the right ratio is not known. However, the  $1.4\mu\text{m}$  PE/ $3.5\mu\text{m}$  PPE ratio fails via wrinkles and the  $3.5\mu\text{m}$  PE/ $1.2\mu\text{m}$  PPE ratio fails via "craters", i.e., expanded pinholes. This is certainly related to the nature of these two organic layers. Flexible polyethylene has pinholes. The rigid, relaxation-prone plasma polymerized ethane is pinhole free.

None of the designs has survived more than two of the severe temperature-humidity cycles without developing defects, which would lead eventually to coating rupture and dissolution of the KBr surface.

#### ENVIRONMENTAL TESTING — FUNGUS

*One of the stated goals of this program was to fungus test the three-layer AR and moisture protective coating that had been developed for the forged KBr color corrector lens. This coating consists of inorganic  $\text{As}_2\text{Se}_3$  next to the KBr surface, followed by a polyethylene layer, and then finally covered with a plasma polymerized ethane layer.*

The fungus test requires 28 days to complete the incubation and growth. As the coating program neared its end, not all the humidity testing relating to the AR three-layer coating had been completed. Since the fungus test was being performed primarily to determine whether the coating provides nutritive value for the fungus, the KBr samples were coated with a thicker layer of polyethylene than specified for the AR design to ensure that the sample would not fail because of the humidity used during the fungus testing. Typically, 10 to  $12\mu\text{m}$  of polyethylene was applied to the forged samples.

The fungus testing was done by a local certified testing company (Environ Laboratories, Inc.). The testing was according to Mil-Std-810C. The test specifies 28 days at  $90^\circ\text{F}$  and 92% to 96% RH. Six varieties of molds or fungi were incubated. Four forged samples were provided plus several samples which had layers of each of the individual materials for the three-layer AR coating on glass. None of the samples grew fungi, while the control samples grew ample quantities of fungi. None of the forged samples failed due to the humidity. The report of Environ Laboratories, Inc. is provided in Appendix C. The materials comprising the three-layer AR coating have passed the fungus test individually and serially without evidence of fungus growth.

## SUMMARY OF ENVIRONMENTAL TEST RESULTS

Coatings which incorporate thin layers of organic material ( $\sim 2\mu\text{m}$ ) fail rapidly, even under relatively modest conditions ( $50^\circ\text{C}$  and 81% RH).

Coatings with somewhat thicker organic layers ( $\sim 5\mu\text{m}$ ) can survive more than 58 hours under the above conditions but develop blemishes due to wrinkles or moisture penetration through coating defects within two cycles of the Mil-Std-810B severe humidity test.

Thicker organic coatings ( $\sim 15\mu\text{m}$ ) survive the harsh environment of the fungus test, with immersion in liquid water for 28 days, and without apparent coating degradation. However, such coatings will have too great absorption, because of the coating thickness, to meet transmission specifications.

KBr can be protected by organic coatings of reasonable thickness under conditions such that the kinetics of moisture attack (Section 6) involve chemi-absorption of water, but not under conditions where the kinetics involve dissolution of the surface. This means that, at  $25^\circ\text{C}$ , a reasonably thin coating could provide protection up to relative humidities around 80%.

Fungus attack of the organic coating materials is not a problem.

## Section 13

### KRS-5 Lens Development

**Task: Improve reproducibility of forged KRS-5 lenses by developing unconstrained forging procedures to replicate the die surface closely, using spherical dies.**

#### BACKGROUND

During earlier work<sup>(1)</sup> it was demonstrated that, by using a forging process, the surface of an alkali halide will replicate, or have the same shape, as the die used in this forging process. Extending this forging process to include aspheric surfaces would be particularly attractive to the optical designer. Diamond turning technology has progressed to the point where rotationally symmetric aspheric optical surfaces can be routinely produced. Using such as aspheric surface as a forging die, one could replicate this aspheric surface on an alkali halide for use in the infrared.

Before costly diamond turned metal dies were purchased, the feasibility of forging halide optical elements using pyrex die surfaces prepared by conventional optical techniques was explored. Promising results were demonstrated with KBr. A plano-concave element was designed to be used as the color corrector in the large FLIR imager<sup>(1)</sup>. This forged KBr lens has repeatedly produced acceptable modulation transfer function (MTF) performance when tested in the imager at 8 to 12 $\mu$ m. With this initial forging success, efforts were directed toward producing a forged optical element with an aspheric surface.

The large imager module was again chosen as a convenient vehicle to demonstrate an optical design which has an aspheric surface on a forged halide element. An imager module optical design which specified a KRS-5 first element with an aspheric front surface and a KCl color corrector with spherical surfaces was developed.<sup>(1)</sup>

The first half of this forging development program (1 October 1979 — 1 April 1980) was devoted to development of a KRS-5/KCl aspheric doublet lens which would meet the MTF specifications of the IR imager. During this period, a number of important developments were performed<sup>(2)</sup>.

- Forging of a number of KCl color corrector lenses considered acceptable for use in testing the KRS-5/KCl doublet performance.
- Forging an aspheric KRS-5 lens and determining its MTF performance in a doublet.
- Forging a spherical KRS-5/KCl doublet to demonstrate that the aspheric KRS-5 doublet provides superior MTF performance.

Later, in response to changing perceptions of the potential role of forged lenses in infrared systems, the contractual task relating to KRS-5 lens development was modified and changed to the statement given above. The philosophy was to develop forging



procedures for replication of KRS-5 as a material, with a view toward potential use of KRS-5 lenses in future infrared systems. At the same time the emphasis on fabricating a KRS-5 lens useful for the common modular FLIR was dropped.

The work in this area led to five published papers at the Optical Society of America Workshop on Optical Fabrication and Testing, 22-23 September 1980. These papers are listed in Appendix D.

In the following subsections, the technical approach for forging the KRS-5/KCl doublet is discussed, along with optical centering, profile probing of the lens surfaces to compare with the aspheric equation, and results using a single-crystal KCl lens produced by conventional methods. Efforts to improve surface replication are also discussed.

#### TECHNICAL APPROACH

The forging of alkali halide optical elements is done using a process called isostatic forging. This is a process developed by the contractor. During the forging deformation, the alkali halides are subject to fracture. To prevent fracture, a hoop stress is applied to the crystal by a high-pressure He gas environment. The He aids in several other important ways. It is inert, clean, aids in lubrication, and is thermally conductive. Figure 60 is a section schematic of this forging system. The forging die assembly is shown within the pressure chamber.

The forging process for both KRS-5 and KCl requires two steps. The first step produces material that is uniformly strained, which will then react in a more predictable manner in the final forging operation. Both the KRS-5 and KCl are initially deformed 60 percent at 250°C. The KRS-5 is then forged at 225°C if pyrex dies are used and at 210°C if the diamond-turned aspheric metal die is used. KCl is forged at 250°C for both operations. The He pressure is typically 4000 psi.

The orientation of the single crystal prior to forging influences the final forged lens. Because of broad experience with KCl, little difficulty was encountered in producing promising lenses. The  $\langle 100 \rangle$  orientation, 1-1/2 inches high by 1-1/2 inches in diameter, produces the best combination of properties using KCl. Six lenses were selected for final edging and shaping for use as the color corrector with the KRS-5 lens.

The deformation characteristics of KRS-5 differ from KCl. The three principal orientations,  $\langle 100 \rangle$ ,  $\langle 110 \rangle$  and  $\langle 111 \rangle$  have been examined. Several aspect ratios have also been evaluated. The best combination of orientation and aspect ratio for KRS-5 appears to be  $\langle 111 \rangle$  for a starting sample 1.5 inch in diameter by 1.5 inch high.

A ray tracing of the KRS-5/KCl doublet is shown in Figure 61. Curvature of both of these optical surfaces dictates that the forging die design must provide the center thickness, centration, and clear aperture requirements of each lens, as well as the radii of the optical surfaces. Since these materials are very soft, centration from these forged optical surfaces is not feasible. The edging and shaping for mounting are performed from the concentric outside diameter and from the forged faces of the annulus around each lens surface.

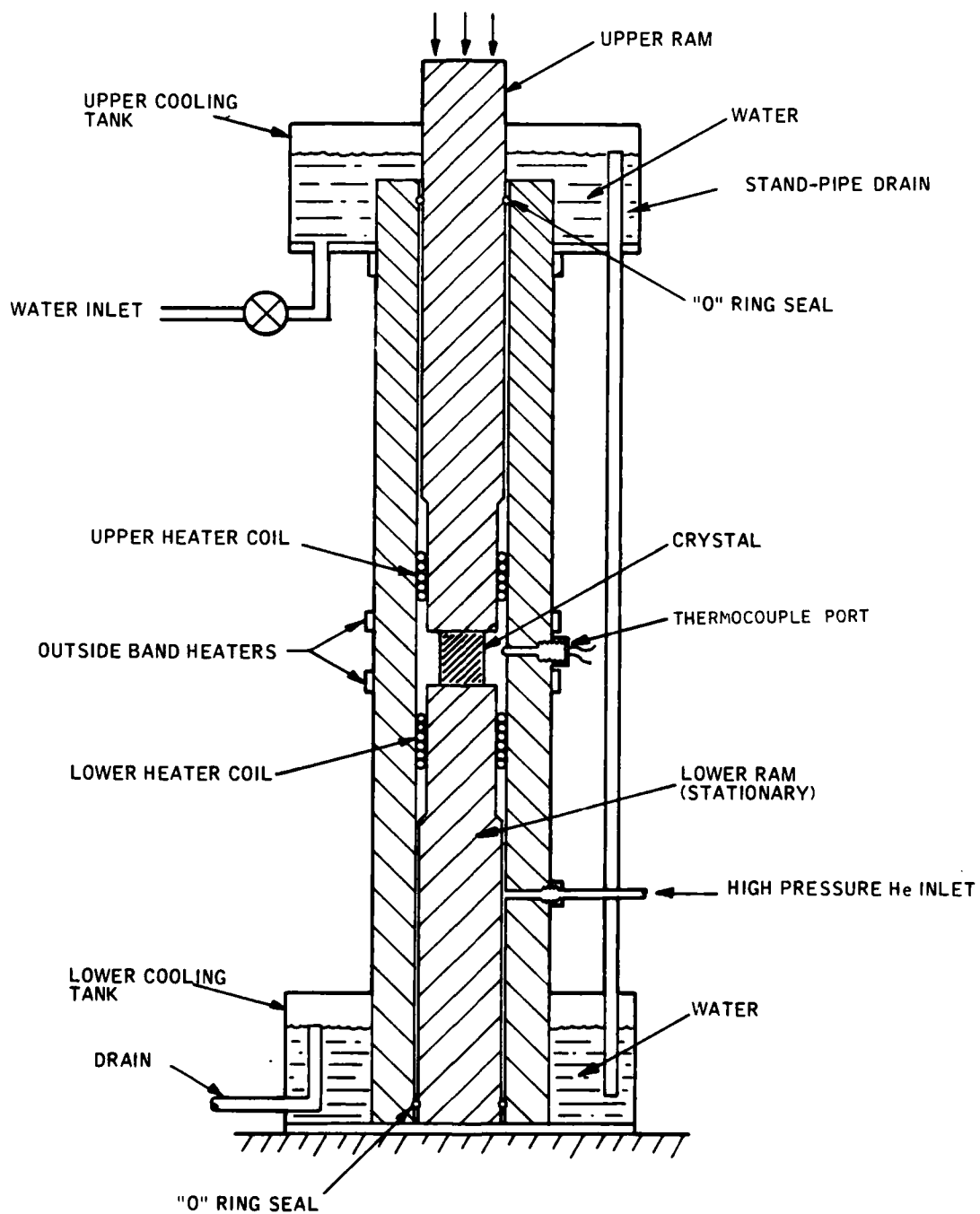
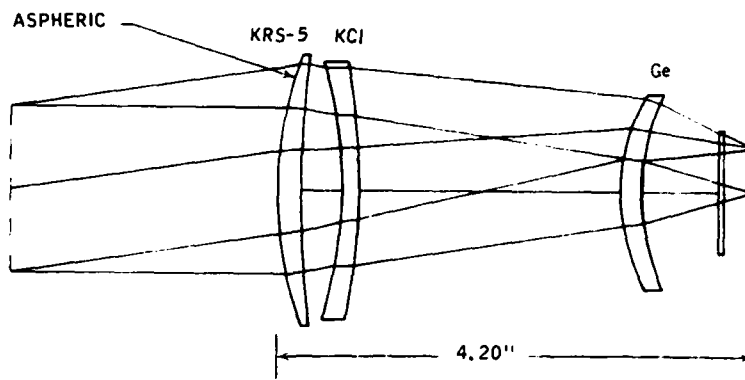


Figure 60. Schematic diagram of forging apparatus.



NVL FLIR DET. LEN  
 LENS Y-Z PROFILE  
 X SCALE 1.000000  
 Y SCALE 1.000000

Figure 61. Ray tracing of KRS-5 aspheric/KCl color corrector lens in imager module.

A closed die design consisting of a molybdenum alignment sleeve with close fitting pyrex dies is used. The length of the sleeve and the dies is maximized to aid in maintaining the required centration and alignment. Figure 62 shows the closed die components for the KCl lens. This arrangement is also typical of the KRS-5 die assembly. The small Mo sleeves surround the pyrex dies during forging and produce the annulus around the clear aperture.

The lenses in the imager are typically permanently mounted with an RTV rubber cement. To facilitate changing the lenses during MTF testing, two doublet mounting rings were purchased. Each was modified to accept threading collars which locate and retain each KRS-5 and KCl lens.

The radii of curvature and optical figures of the clear apertures are determined interferometrically. The aspheric surface can be evaluated partially by this method. This determination does not require contact with the optical surfaces of the lens.

Since it was anticipated that the diamond-turned die would not be received from Bell and Howell for 3 or 4 months after ordering, a spherical KRS-5/KCl doublet was also designed. The single difference between the aspheric and spheric doublets is the front surface of the KRS-5 lens. Making this spherical die with a Pyrex® die permitted the forging program to proceed in this interim.

The lens design predicts that the spherical doublet should produce an MTF of 0.67 at 10 line pairs (lp)/mm in the imager. The aspheric doublet should produce an MTF of 0.76

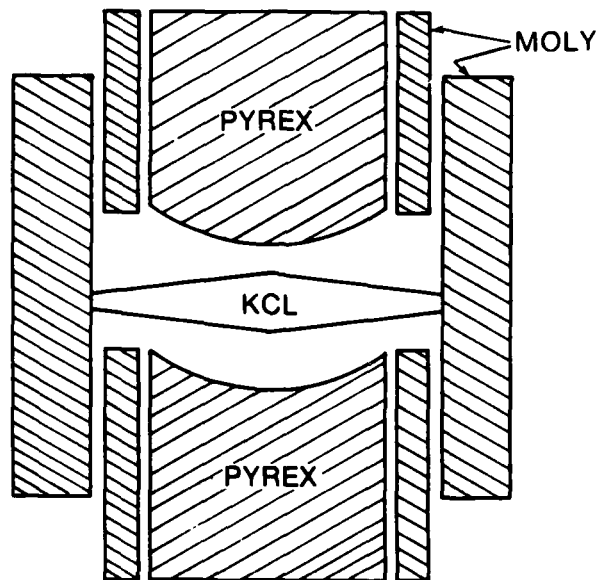


Figure 62. Closed die components for forging of KCl.

(1). This is a significant difference and should demonstrate that the forged aspheric doublet is performing as intended. It was intended to show that a forged aspheric would perform in an imager module and meet the specifications.

### OPTICAL CENTERING

The low hardness of KRS-5 and KCl make them very susceptible to scratching during evaluation. Consequently, attempts to measure the center thickness and wedge in the lenses have used optical methods which are noncontacting. Imperfect optical centering is one possible cause for poor optical performance. A simple centering fixture was made for use on a lathe. With a He-Ne laser reflecting from the concave surfaces of each element, lenses were centered and edged. Figure 63 shows this fixture mounted on the lathe. An aluminum plate is counterbored to accept the KRS-5 or KCl forging. A screw tightens the blank in the counterbore. Three screws, threaded into the aluminum plate, adjust for the wedge in the lens. Through the center of these screws are three more screws which permit centering through the outer screws. These center screws hold the fixture fixed during centering.

The screws are adjusted until the HeNe laser beam is accurately reflected back on itself. At the same time, the lens is rotating in the lathe. The HeNe laser beam will be deflected to the side, unless the beam strikes the center of the lens and unless the lens is not wedged in the fixture. When the beam is accurately reflected back from the center of the

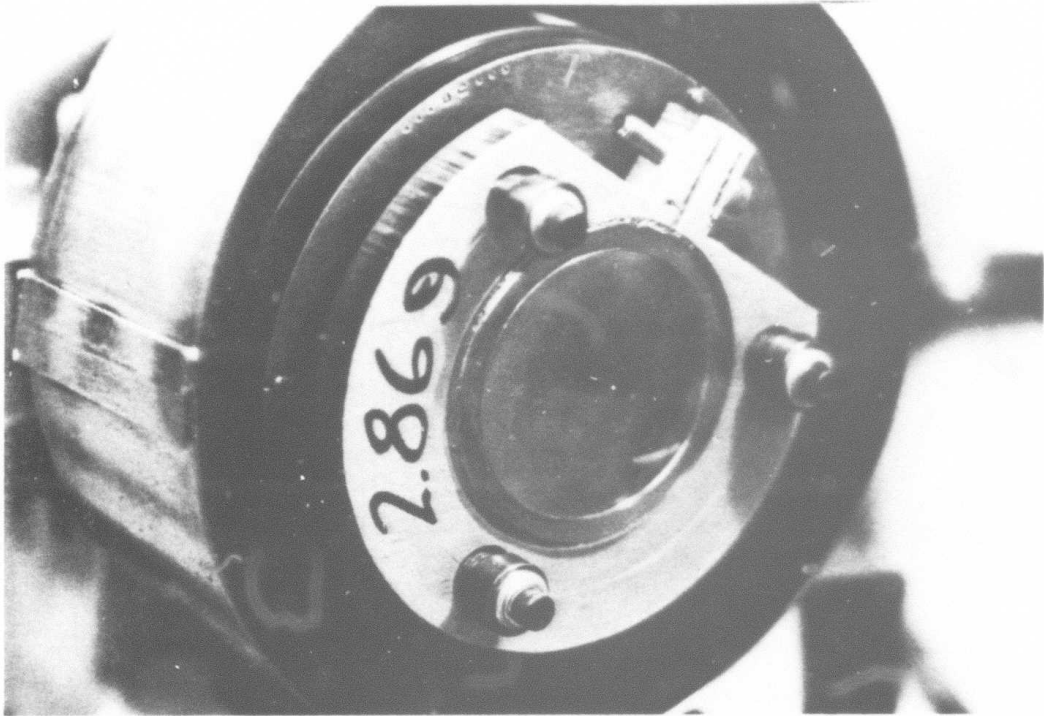


Figure 63. Optical centering fixture mounted on a lathe.

rotating lens, indicating good centering and no wedge, the edge of the lens is ground on the lathe to produce an accurate lens shape.

This fixture is simple and easy to use. After it was constructed, the optical performance of the KRS-5 and KCl lenses was improved.

#### EVALUATION OF THE ASPHERIC LENS

This portion of the work concerned optical tests on the aspheric KRS-5 lenses forged in the contract. This evaluation has predominantly used the Honeywell-Tropel interferometer and modulation transfer function (MTF) testing at NV&EOL.

Work on the asphere has been carried through one complete cycle of lens design, die design, die fabrication, lens forging, doublet assembly and MTF testing of the doublet for a series of KRS-5 lenses. The approach involved both a straightforward technique and a novel technique. The straightforward technique is to design a lens, make the die, forge the lens and test it. However, as aspheric lenses are difficult to test, a backup plan was developed that included designing and forging a lens like the asphere only without

the aspheric additions to the base sphere. The spherical lens design does not depart more than 0.001 inch from the asphere anywhere on its surface. It uses the same spherical die for the back side and the same center thickness as does the asphere. The idea is to show that the asphere is in fact present and functioning as it relates to its spherical counterpart. The design indicates that there should be an 11% increase in MTF with the asphere as compared to the base sphere lens. This was done because an asphere is difficult to check unless it performs perfectly. If anything were to go wrong in the application of the forging technique, it would immediately be assumed that the asphere had failed. With the base sphere design as a backup, the increase in performance would prove the asphere had been successfully forged, and the fault would lie elsewhere.

To make aspheric lens requires an aspheric die. A diamond-turned die from Bell and Howell was used. A stainless steel blank was first turned to the base sphere. The surface of this stainless steel die was then plated with 0.005 inch of nickel. This gives ample room for the 0.001-inch departure of the asphere. After being turned on the single-point diamond turning (SPDT) device, polished to remove the "record groove of the SPDT" and annealed, the die was ready to forge the KRS-5 lens.

Inspecting the aspheric die with a computer-generated hologram (CGH) was planned with two-wavelength holography (TWH) as a backup. The CGH was to be generated by the same polynomial that ran the SPDT apparatus so verification would be straightforward. However, if some failure mechanism came into play, TWH would be able to give a view of the surface at a simulated wavelength of at least  $28\mu\text{m}$ . This would detune the interferogram of the asphere enough to analyze it so the die could be certified.

To make the spherical surface, a pyrex® die was used. The spherical die of "base" radius would also be used to learn to forge KRS-5 while the aspheric die was being generated and also to make the spherical lenses that could be tested in the imager to compare to the asphere. The spherical concave "base" radius Pyrex® die and the spherical convex die for the backup were verified on the Honeywell-Tropel interferometer.

Centration and center thickness were always measured. Centration was verified by mounting the lens in a rotating jig off center under a microscope. A given radius is observed while the lens is rotated. Any change in focal position of the radius being inspected implies a decentration. The technique is accurate to  $\pm 0.001$  inch for the surface position and to  $\pm 0.005$  inch for the concentration specification.

Center thickness was measured by applying an apparent index in a simple procedure. A microscope was focused on the center of the lens and then focused through the lens on the other side. The travel of the microscope gives the center thickness when the index is known and the contribution of the power of the lens surface is known. This power is easily calibrated with the aid of a "used" lens where physical center thickness measurements can be made and the calibration verified.

The imager's movable lens doublet is Ge-ZnSe. The original program goal was to replace that with a KRS-5/KCl doublet. KRS-5 lenses described above are mounted in a special

threaded doublet mounting ring and a brass collar secures the lens to a shoulder inside the ring. This approach eliminates the silicone rubber mounting in the imager. The threaded ring facilitates removal and replacement of the lens in a matter of minutes, whereas silicone rubber requires overnight curing.

The mount holds two lenses. The second is the color corrector KCl lens. This too is screwed into place. The air gap is controlled by the height of the shoulder machined on the lens and centration is positioned by the brass ring. Center thickness measurements are made through the lens and the radius of curvature is derived from the optical figure. Separate KCl lenses were forged for the asphere and the sphere and two mounting rings were machined so that testing could be performed with minimal difficulty.

The aspheric design for the KRS-5 lens and its predicted MTF performance in the imager module have been discussed previously<sup>(2)</sup>. The calculated value of the MTF for on-axis performance at 10 lp/mm is 0.77. The design allows the first Ge lens and the ZnSe color corrector to be replaced directly with the aspheric KRS-5 lens and KCl color corrector.

The lens design parameters of the spheric KRS-5 lens with the best fit to the asphere indicate that the on-axis performance of the imager should be 0.66 at 10 lp/mm. This is a significant decrease of 0.11, as compared to the asphere.

The shape of the die must be such as to produce the designed lens shape after forging. This means the shape of the die is not the same as the lens or its design. The coefficient of thermal expansion (CTE) of the die material as the die heats to the forging temperature opposes the CTE of the lens material as it shrinks from the forging temperature back to room temperature. There are two basic assumptions that have never been validated but are included in all the designs. The first assumption is that the die radius of curvature swells linearly to the larger forging radius. Also, it is assumed that after forging the lens, when the force is relieved, the lens shrinks linearly from the hot forging radius to the room temperature lens design radius. The second assumption is that the asphere will follow the base sphere, and that all swelling and shrinking considerations need only address the spherical components.

The specifications supplied to Bell and Howell to turn the stainless steel aspheric die included a CTE for stainless steel of  $11 \times 10^{-6}/^{\circ}\text{C}$ .

This would produce the base radius of 3.539 inch for a temperature change from room temperature to a forging temperature of  $100^{\circ}\text{C}$  ( $\Delta T = 78^{\circ}\text{C}$ ). This produced a 0.014 inch change in the radius. The aspheric coefficients from the lens design were added directly to that new radius.

A spherical Pyrex<sup>®</sup> die was purchased to forge the other KRS-5 lens to a 3.539-inch radius. The concave side of both KRS-5 lenses was forged by a pyrex<sup>®</sup> die aimed at forging a 9.294-inch radius. All of the glass dies were purchased locally and if broken were readily replaced. Dies for the KCl lens were supplied by the same local vendor, Advance Optics.

The aspheric die from Bell and Howell did not appear to be correct when received. The view on the Twyman-Green interferometer showed successive spherical zones, precluding use of the CGH for verification of the asphere. The observed spherical zones (shown in Figure 64) had measurable diameters out to 2-1/2 inches. These zones were visible and as such gave fairly accurate numbers. The numbers from the spherical zones were then fitted to the asphere, with each zone being divided into ten subzones. The listing of each position, as approximated from the photographs and compared to the ideal case, is shown in Table 7 along with the difference values. In all cases but the last few points of the last zone, this difference is less than  $2\mu\text{m}$ , including the areas where the zones change over. This implied the die would work. An effort was made to verify the aspheric die with two-wavelength holography, but this particular surface is too steep for the optics available. The TWH setup could see about 1 inch of clear aperture ( $\Delta f/3$ ) at equivalent wavelengths of  $9\mu\text{m}$  and  $28\mu\text{m}$ . At both wavelengths the fringes showed no breaks as they passed from zone to zone. This implied acceptable performance in the  $8\mu\text{m}$  to  $12\mu\text{m}$  range but without a larger clear aperture it was not possible to confirm it. These two results, the zone plot and the equivalent  $9\mu\text{m}$  view, indicated that the aspheric die would be suitable for forging.

Figure 65 shows the reflected optical figure of the concave side of an aspheric forged lens. It shows that the radius came out short by  $\sim 0.3$  inch.

The aspheric convex side too was short. The spherical zones of the die are visible in the lens. Figure 66 shows the forged asphere. It shows the clear transition from zones 1 to 2 as was shown for the die in Figure 64a and b. The spherical character of these zones approximates those on the die. Figure 67 shows a KRS-5 lens forged between spheric glass dies. The reflected optical figure (in the visible) shows  $\lambda/4$  to  $\lambda/2$  departure from spherical on both sides and radius of curvature within 0.010 inch of design on both sides. This proves that accurate replication of the die surfaces can be done to within a fraction of a wavelength in the visible.

The forged KRS-5 asphere and its spherical counterpart each were checked for concentration with a microscope. The mount for the microscope allows focusing on the lens at a given distance from the center while rotating the lens. A detectable change in focus would imply a decentration about 0.001 inch which is close to the required 0.005 inch.

Center thickness was also observed on the same apparatus, using the 0.001 inch precision of the microscope to view the apparent thickness. The actual thickness is the apparent thickness times the index plus any power added by the shape of the transmitting surface. The index and the power are included in one constant for any given lens. A working number of 2.49 was determined for the KRS-5 lens viewed through the 3.5-inch-radius face. This was calibrated by sacrificing a few lenses with contact measurement.

The air gap between lenses is specified at the lens center assuming the surface is spherical all the way to the mounting flange. On the two KRS-5 lenses in question there was a difference of 0.005 inch between the measured sagitta and the sagitta calculated

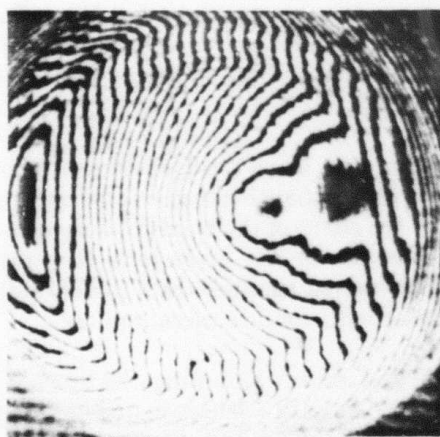




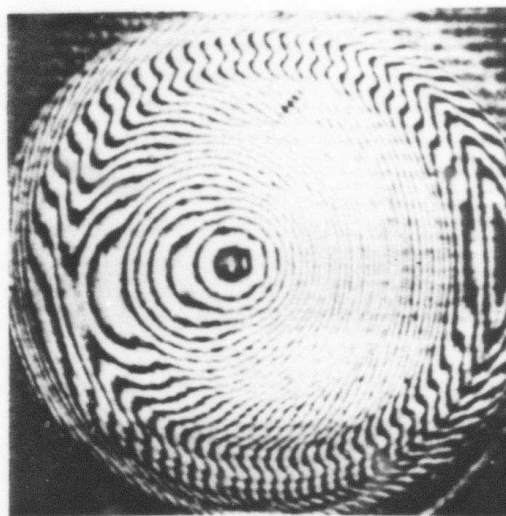
(a) 3.557 in.



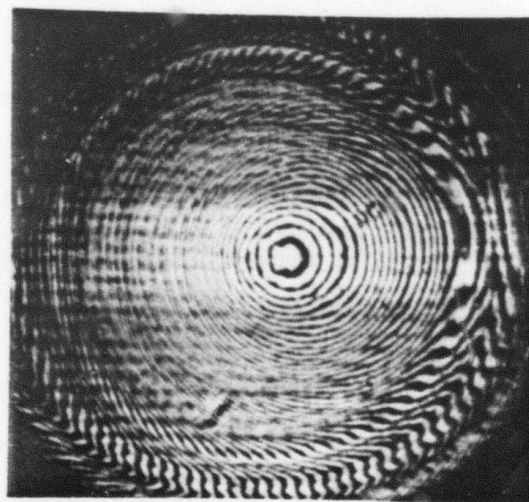
(b) 3.548 in.



(c) 3.541 in.



(d) 3.534 in.



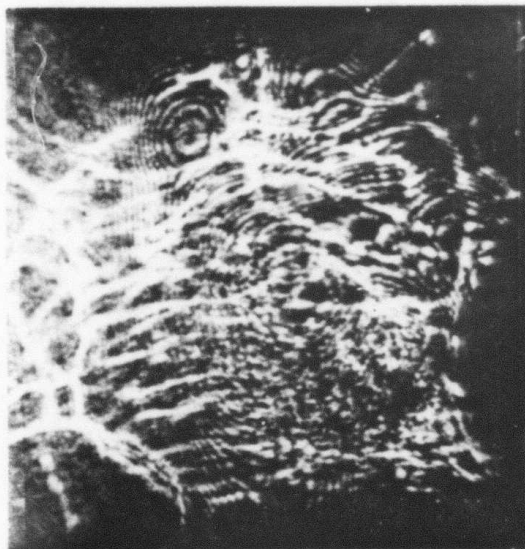
(e) 3.525 in.

Figure 64. Spherical zones on the aspheric die and their radii of curvature.

Table 7. Site Table for Ideal Asphere (ZIDEAL) Positions on the Die (ZAPPRX) and the Difference (DIFF) versus Radial Position Y

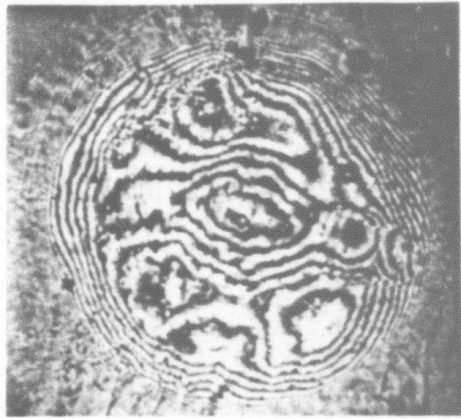
Y	ZIDEAL	ZAPPRX	DIFF
0.0281	0.000111	0.000111	-0.000000
0.0562	0.000445	0.000444	-0.000001
0.0843	0.001000	0.000999	-0.000001
0.1124	0.001778	0.001776	-0.000002
0.1405	0.002779	0.002776	-0.000003
0.1686	0.004003	0.003998	-0.000005
0.1967	0.005450	0.005443	-0.000007
0.2248	0.007120	0.007111	-0.000009
0.2529	0.009014	0.009002	-0.000012
0.2810	0.011132	0.011117	-0.000015
0.2982	0.012539	0.012525	-0.000014
0.3154	0.014031	0.014017	-0.000014
0.3326	0.015607	0.015594	-0.000013
0.3498	0.017268	0.017256	-0.000012
0.3670	0.019013	0.019001	-0.000012
0.3842	0.020844	0.020832	-0.000012
0.4014	0.022759	0.022747	-0.000012
0.4186	0.024760	0.024748	-0.000012
0.4358	0.026846	0.026833	-0.000012
0.4530	0.029017	0.029004	-0.000013
0.4686	0.031061	0.031051	-0.000010
0.4842	0.033175	0.033169	-0.000007
0.4998	0.035361	0.035357	-0.000004
0.5154	0.037617	0.037615	-0.000002
0.5310	0.039945	0.039945	0.000000
0.5466	0.042344	0.042346	0.000002
0.5622	0.044815	0.044818	0.000003
0.5778	0.047358	0.047362	0.000004
0.5934	0.049973	0.049977	0.000004
0.6090	0.052660	0.052664	0.000004
0.6231	0.055151	0.055160	0.000009
0.6372	0.057701	0.057715	0.000013
0.6513	0.060311	0.060329	0.000017
0.6654	0.062981	0.063002	0.000021
0.6795	0.065711	0.065735	0.000024

0.6936	0.068501	0.068527	0.000026
0.7077	0.071352	0.071379	0.000027
0.7218	0.074263	0.074291	0.000028
0.7359	0.077235	0.077263	0.000027
0.7500	0.080268	0.080294	0.000026
0.7656	0.083695	0.083727	0.000032
0.7812	0.087198	0.087234	0.000036
0.7968	0.090776	0.090815	0.000039
0.8124	0.094430	0.094471	0.000041
0.8280	0.098161	0.098201	0.000041
0.8436	0.101968	0.102007	0.000039
0.8592	0.105852	0.105889	0.000036
0.8748	0.109814	0.109845	0.000031
0.8904	0.113854	0.113878	0.000024
0.9060	0.117973	0.117987	0.000015
0.9185	0.121329	0.121345	0.000015
0.9310	0.124737	0.124752	0.000015
0.9435	0.128195	0.128208	0.000013
0.9560	0.131705	0.131714	0.000009
0.9685	0.135266	0.135270	0.000004
0.9810	0.138879	0.138876	-0.000003
0.9935	0.142544	0.142532	-0.000012
1.0060	0.146261	0.146239	-0.000023
1.0185	0.150031	0.149996	-0.000035
1.0310	0.153853	0.153803	-0.000050
1.0404	0.156763	0.156706	-0.000057
1.0498	0.159702	0.159638	-0.000064
1.0592	0.162672	0.162599	-0.000073
1.0686	0.165672	0.165589	-0.000083
1.0780	0.168702	0.168608	-0.000095
1.0874	0.171763	0.171656	-0.000107
1.0968	0.174855	0.174733	-0.000122
1.1062	0.177977	0.177840	-0.000137
1.1156	0.181131	0.180976	-0.000154
1.1250	0.184315	0.184142	-0.000173

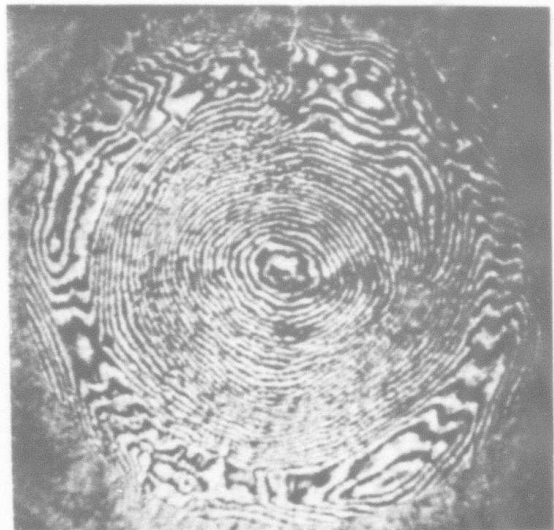


8.97 in. Radius  
of Curvature

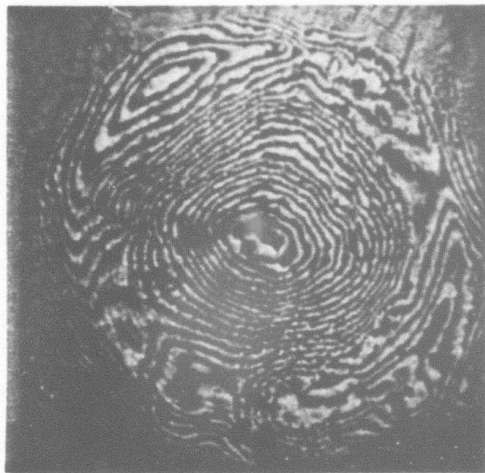
Figure 65. Optical figure of the concave side of aspheric lens 727.



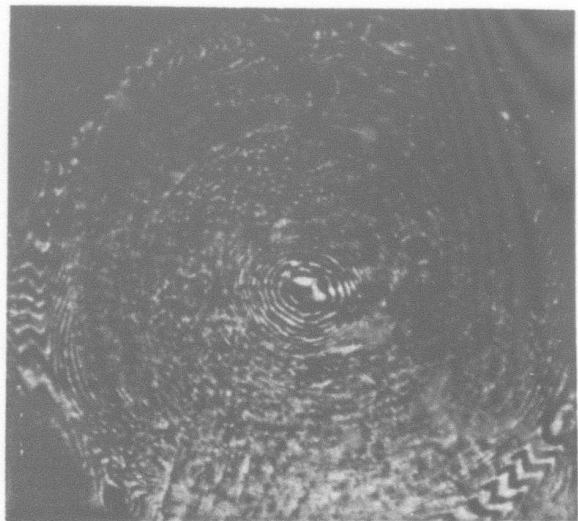
(a) 3.48 in.



(c) 3.46 in.

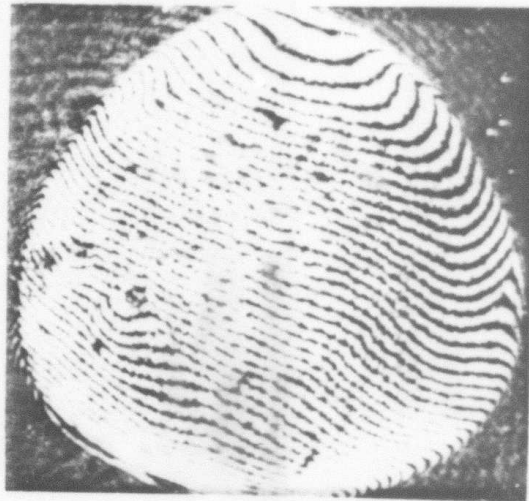


(b) 3.47 in.



(d) 3.44 in.

Figure 66. Optical figures of the forged asphere.



CONVEX  
3.54 in. Radius



CONCAVE  
9.29 in. Radius

Figure 67. Optical figure of a forged spherical KRS-5 lens 714.

from the measured radius of curvature. This places the center of the lens 0.005 inch further from the detector than the design calls for. It was assumed this would not be significant and that the best procedure was to fabricate the lens as close to the design as possible. The total doublet air gap should be the KRS-5 concave sagitta plus the 0.083-inch dimension of the doublet mounting ring, plus the concave sagitta of the KCl lens. This combination results in too much air by 0.026 inch. The easiest element to machine of those three elements is the concave shoulder of the KCl color corrector. Removal of 0.026 inch from that shoulder moves the KCl lens toward the KRS-5 0.026 inch so the design is achieved.

Table 8 lists the relevant parameters of the two doublet lenses which were initially produced.

These doublets were measured at NV&EOL in April 1980. The doublets were evaluated in an unconventional mounting. The conventional mounting included a folding mirror that had been replaced and was, therefore, subject to some question. Also the presence of a mirror in the apparatus compounded the difficulty of aligning the MTF equipment. The new mount has a straight-through design with all the correct dimensions. It is designed to hold all three lenses of the imager. The third lens element was removed from the other imager and placed within the straight-through unit so that a calibration could be done using the elements identical to those used for the previous phases of the program. Figure 68 plots the MTF of the FLIR imager containing the three original lenses, showing acceptable performance both on axis and off axis. This imager has been

Table 8. Doublet Lens Characteristics

Lens Parameter	Aspheric Doublet 727,720 (inches)	Design Values (inches)	Spherical Doublet 701,710 (inches)
<b>KRS-5 Lens</b>			
Asphere radius	3.48	3.54	3.54
Lens thickness	0.279	0.270	0.276
Concave radius	8.97	9.29	9.34
<b>KCl Lens</b>			
Air gap	0.305	0.297	0.296
Concave radius	4.14	4.16	4.15
Lens thickness	0.150	0.150	0.162
Convex radius	7.17	7.33	7.10



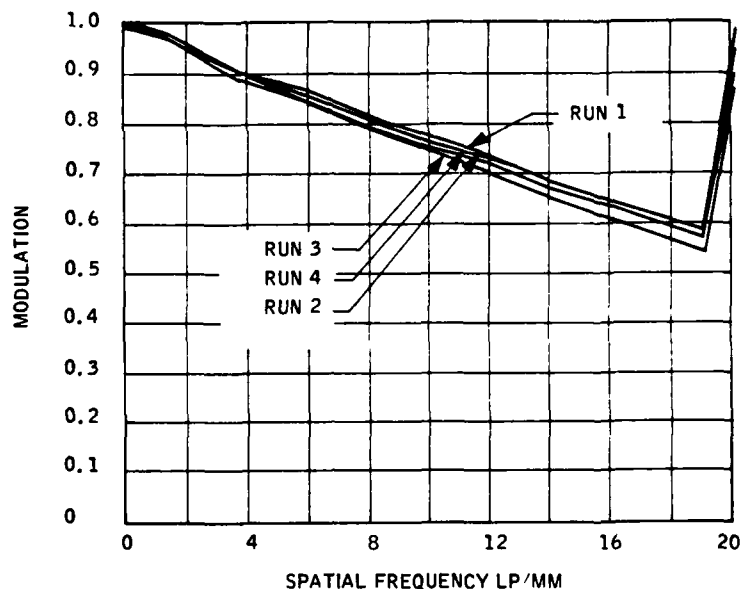


Figure 68. Imager MTF with Ge-ZnSe doublet in the modified straight-through design.

tested before at NV&EOL and as such is labeled Martin Marietta S/N 1. The performance plotted in the above figure is tabulated in Table 9 along with the measured values for effective focal length (EFL) and flange distance (FD). The FD must also move through a range of  $\pm 0.47\text{mm}$  which is larger than the FD tolerance of  $\pm 0.25\text{mm}$ . This ranging of the FD is accomplished by moving the doublet to its focusing limits. Imager S/N 1 performed outside of this specification. The FD was  $0.2\text{mm}$  short in the midrange focal condition and  $0.38\text{mm}$  long at the counterclockwise (CCW) limit. The clockwise (CW) limit put the FD  $0.91\text{mm}$  short, showing that all of the tolerance went on the CW side of focus. This calibration run verified the straight-through imager as an acceptable mount for the imager lenses and cleared the way for evaluating the asphere.

The imager data taken with the aspheric doublet is labeled No. 2027. Our lenses 720 and 727 comprise this doublet. The MTF plot for the imager with alkali halide S/N 2027 is shown in Figure 69. The MTF is  $0.54$  at  $10\text{ lp/mm}$ . The separation of the two traces across the plot is probably due to a centration difficulty. Table 10 lists the numerical data for the four runs as well as the EFL and FD. The FD was short  $0.4\text{mm}$  whereas the requirements allow  $0.25\text{mm}$ . With the focusing ring fully CW, the FD included the required  $0.47\text{mm}$  range; however, with the ring CCW, the FD only went to  $18.04\text{mm}$ , falling short of the requirement by  $0.2\text{mm}$ .

The low MTF value of  $0.54$  at  $10\text{ lp/mm}$  was offset by the performance of the spherical doublet. The reason for the spherical doublet is to prove the presence of the asphere. The performance of the spherical doublet should be  $11\%$  less than that of the asphere when the asphere is functioning correctly. This difference is considered a proof of the asphere.

Table 9. MTF Performance Tabulation 1

This data file contains 4 runs on Martin Marietta large common module imager, serial number 1.

Run No.	<u>Azimuth</u>		<u>Elevation</u>		Refocus Desired	Slit Orientation
	<u>Degrees</u>	<u>Minutes</u>	<u>Degrees</u>	<u>Minutes</u>		
1	0	0	0	0	Yes	Vertical
2	-4	-12	0	0	No	Vertical
3	0	0	-4	-12	No	Vertical
4	0	0	4	12	No	Vertical

All these data were taken using a  $23\mu\text{m}$  wide scanning slit and a step size that calculated MTF numbers at 1.282 lp/mm apart. The measured effective focal length is 66.93mm. The flange focal length is 17.9mm.

Martin Marietta large common module imager, serial number 1

<u>Frequency</u> <u>lp/mm</u>	<u>Run</u> <u>No. 1</u>	<u>Run</u> <u>No. 2</u>	<u>Run</u> <u>No. 3</u>	<u>Run</u> <u>No. 4</u>
0	100	100	100	100
1.282	98.25	97.77	98.31	97.61
2.563	94.49	93.28	94.6	92.77
3.845	90.96	89.88	90.98	88.92
5.126	88.34	88.1	88.09	86.78
6.408	85.56	85.85	84.96	84.29
7.69	82.25	82.5	81.36	80.77
8.971	79.05	79.28	77.94	77.43
10.25	76.54	76.95	75.16	75.13
11.53	74.18	74.41	72.41	72.79
12.82	71.59	71.13	69.34	69.87
14.1	68.87	67.92	66.2	66.95
15.38	66.42	65.55	63.45	64.73
16.66	63.86	63.2	60.66	62.39
17.94	61.22	60.36	57.78	59.57
19.22	58.68	57.64	55.02	56.88



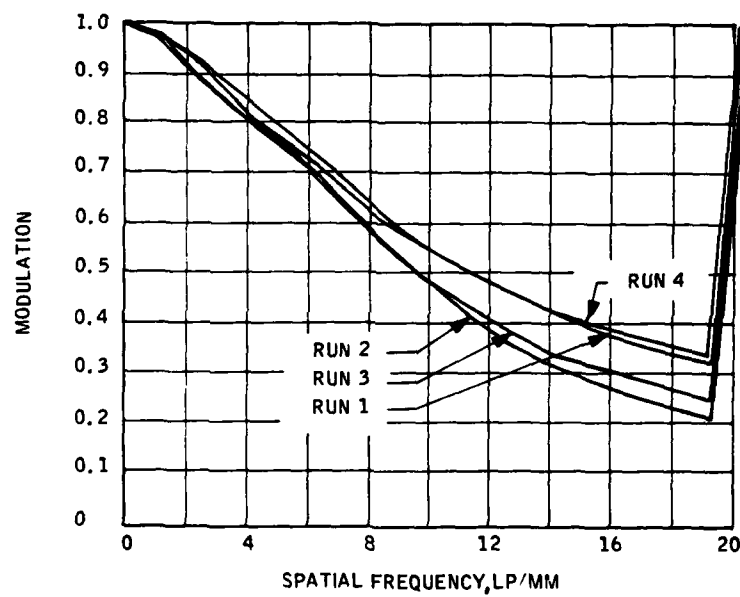


Figure 69. Imager MTF with aspheric KRS-5 and forged KCl.

Table 10. MTF Performance Tabulation 2027

This data file contains 4 runs on Honeywell Inc.  
large imager with alkali halide, serial number 2027.

Run No.	Azimuth		Elevation		Refocus Desired	Slit Orientation
	Degrees	Minutes	Degrees	Minutes		
1	0	0	0	0	Yes	Vertical
2	-4	-12	0	0	No	Vertical
3	0	0	4	12	No	Vertical
4	0	0	-4	-12	No	Vertical

All these data were taken using a  $23\mu\text{m}$  wide scanning slit and a step size that  
calculated MTF numbers at 1.282 lp/mm apart. The measured effective focal length is  
67.8mm. The flange focal length is 7.9mm.

Honeywell Inc.  
large imager with alkali halide, serial number 2027

Frequency lp/mm	Run No. 1	Run No. 2	Run No. 3	Run No. 4
0	100	100	100	100
1.282	97.62	97.4	96.45	96.78
2.563	92.06	91.25	88.65	89.7
3.845	85.81	84.16	81.04	82.92
5.126	79.85	77.13	74.77	77.57
6.408	73.35	69.43	67.8	71.79
7.69	66.31	61.16	59.67	65.09
8.971	59.71	53.32	52.21	58.93
10.25	54.38	46.73	46.64	54.36
11.53	49.7	40.95	41.84	50.39
12.82	45.3	35.69	37.14	46.37
14.1	41.52	31.26	33.25	42.84
15.38	38.87	28.01	30.84	40.39
16.66	36.73	25.36	28.76	38.22
17.94	34.52	22.99	26.32	35.91
19.22	32.22	21.00	24.2	33.98

Figure 70 plots the performance of the imager with the spherical doublet. The KRS-5 spherical lens 701 and the KCl lens 710 comprise this doublet. They perform 14% below the asphere (at 10 lp/mm). It is not presently known why the asphere performance was 0.54, but it speaks well for the system and the overall design to have the spherical counterpart come in at the relatively defined values. The numerical listing of the spherical doublet's performance is shown in Table 11. Its EFL and FD are also listed. The FD is correct in the midrange position, is long by 0.01mm in the CW position and meets the requirement with 0.05mm to spare in the CCW position.

Table 12 lists the EFL and FD in the three focusing positions for S/N 1, (Ge-ZnSe doublet), S/N 2027 (KRS-5 asphere-KCl) and S/N 1001 (KRS-5 sphere-KCl) along with the imager specifications.

The forged KCl lenses were also tested separately. Figure 71 shows the optical figures of the KCl lens of doublet 2027 and doublet 1001. Six of these KCl lenses were forged on the program. They all have acceptable optical figures as shown in Figure 71. The radius of curvature repeats well, as shown in Table 13.

The optical figure is so close to the grinding specification that three figures (with tilt) are shown in Figure 72. The figures show the surfaces to be within 3 fringes in the visible. The forging of the KCl lenses thus produces good lenses.

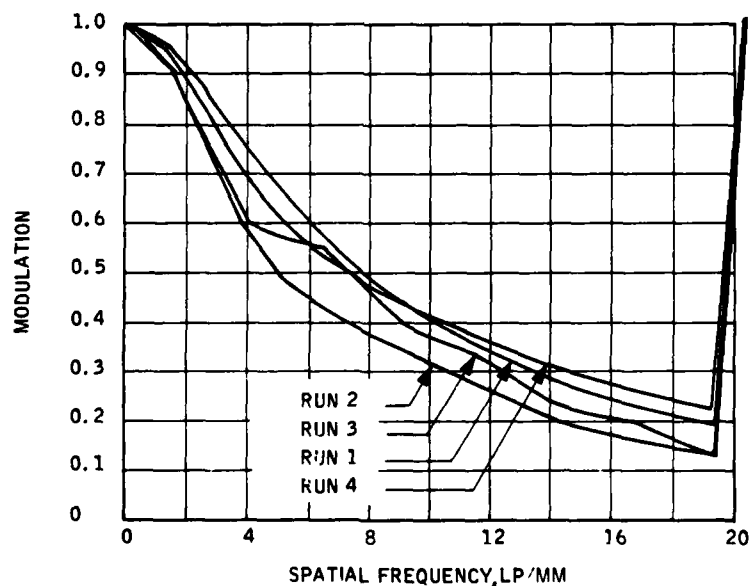


Figure 70. Imager MTF with spheric KRS-5 and forged KCl.

Table 11. MTF Performance Tabulation

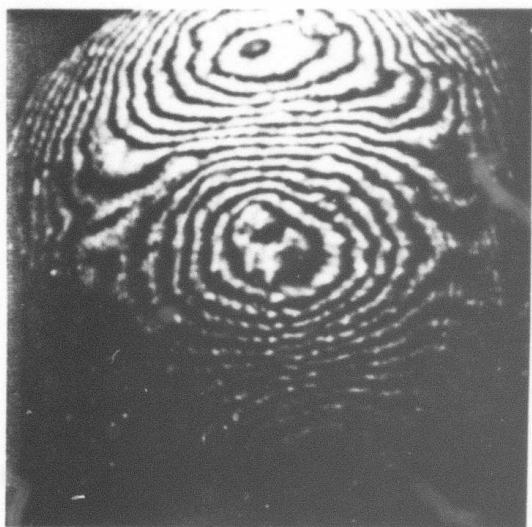
This data file contains 4 runs on Honeywell Inc.  
large common module imager, serial number 1.

Run No.	Azimuth		Elevation		Refocus Desired	Slit Orientation
	Degrees	Minutes	Degrees	Minutes		
1	0	0	0	0	Yes	Vertical
2	-4	-12	0	0	No	Vertical
3	0	0	4	12	No	Vertical
4	0	0	-4	-12	No	Vertical

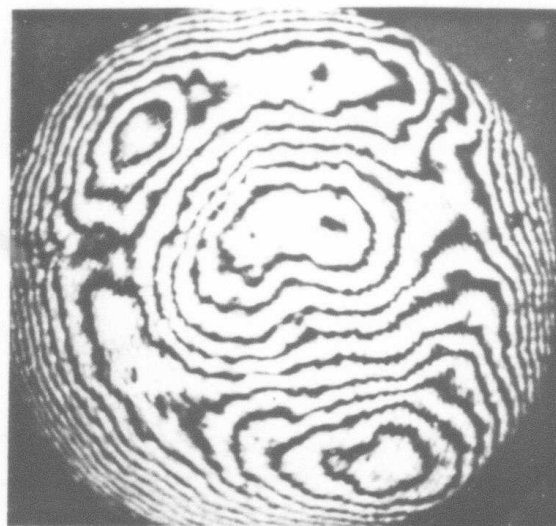
All these data were taken using a 23 $\mu$ m wide scanning slit and a step size that calculated MTF numbers at 1.282 lp/mm apart. The measured effective focal length is 67.17mm. The flange focal length is 17.93mm.

Honeywell Inc.  
large imager with alkali halide, serial number 1001

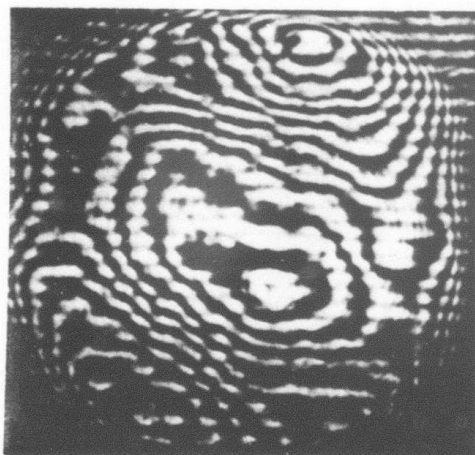
Frequency lp/mm	Run No. 1	Run No. 2	Run No. 3	Run No. 4
0	100	100	100	100
1.282	96.00	91.47	92.9	94.67
2.563	86.46	73.23	76.46	82.32
3.845	75.65	59.8	60.12	69.47
5.126	66.21	56.82	49.68	60.03
6.408	57.95	54.82	43.95	53.33
7.69	50.56	47.86	39.71	48.00
8.971	44.47	40.15	35.58	43.78
10.25	39.95	36.25	31.91	40.65
11.53	36.07	33.4	28.44	37.51
12.82	32.19	28.43	24.84	34.09
14.1	28.59	23.49	21.39	30.98
15.38	25.94	21.53	18.93	28.8
16.66	23.79	20.18	17.31	26.81
17.94	21.72	17.00	15.96	24.65
19.22	19.89	14.07	14.66	22.79



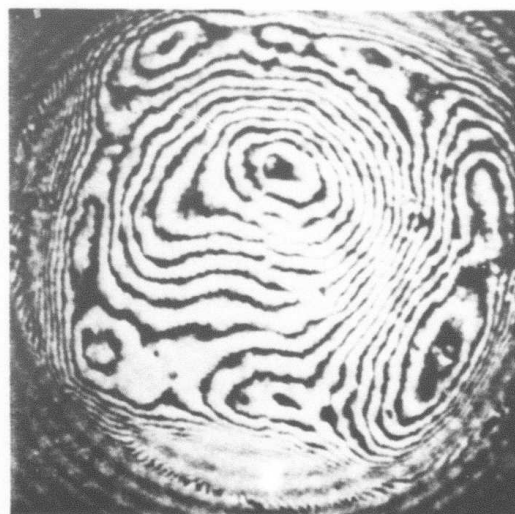
7.175 in. R.C.



7.10 in. R.C.



4.14 in. R.C.  
Lens 720



4.15 in. R.C.  
Lens 710

Figure 71. Optical figures and radii of curvature of forged KCl lenses.

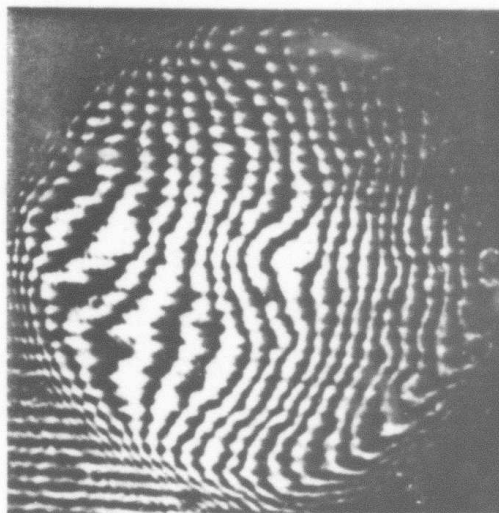
Table 12. EFL and FD Tabulation (mm)

	S/N 1		S/N 2027		S/N 1001		Specs	
	EFL	FD	EFL	FD	EFL	FD	EFL	FD
CW	68.97	16.95	68.86	16.84	68.68	17.47	(1)	17.39
Middle	67.90	17.66	67.69	17.46	67.17	17.78	67.8±.7	17.86±.25
CCW	67.45	18.24	66.70	18.05	66.76	18.38	(1)	18.33

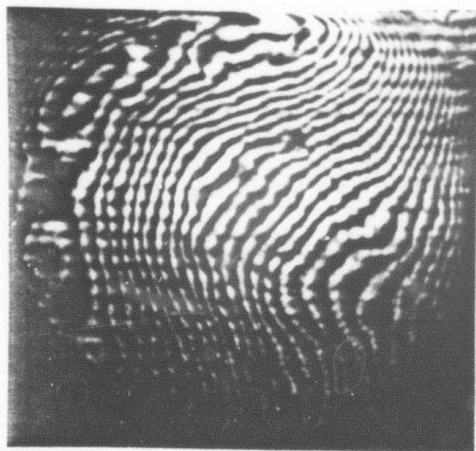
(1) "EFL test shall be conducted with the ring gear set to the midpoint of its angular rotation." Paragraph 4.2.5.1 of the image inspection requirements.

Table 13. Radii of Curvature Lenses

Lens No.	Convex Side (inches)	Concave Side (inches)
710	7.10	4.15
711	7.26	4.16
713	7.23	4.15
715	7.22	4.14
720	7.18	4.14
721	7.05	4.12



Lens 711



Lens 720



Lens 721

Figure 72. Reproducibility of optical figures of forged KCl lenses.

Three additional efforts were made to prove the asphere at NV&EOL. They were made in June 1980, July 1980 and January 1981. In each case a combination series of MTF tests was done on forged KC1 and forged KRS-5 lenses. One lens was alternately tested with other lenses. The intent of this mix and match technique was to smooth out the error bars on the aspheric data with the understanding that the KC1 lens was also a new and untested parameter. This procedure was dictated by the fact that the KC1 lens had no way to be certified except in conjunction with its KRS-5 counterpart. They comprise a unique doublet.

In June 1980 one KC1 lens and four KRS-5 lenses were tested at NV&EOL. Seven combinations were evaluated because one of the aspheres had a deep scratch across its face and the influence of the scratch on the MTF was unknown. Three of the KRS-5 lenses were forged aspheres, and the third was a remake of a KRS-5 spherical lens. This spherical KRS-5 lens was number 737 and the aspheres were numbers 733, 734 and 738. The results at 10 lp/mm are shown in Table 14. The values ranged from 0.51 to 0.72. The spherical KRS-5 lens 737 produced test results within the scatter of the aspheric data.

The scratched asphere (734) showed the best MTF so it was retested using the scratch as a marker. Repositioning did not repeat the first test results, which implied a need for improved lens centration. The MTF results at 10 lp/mm with the scratch at 12 o'clock, 10:30 and 9:00 were 0.69, 0.63 and 0.64, respectively.

The data listed above from June 1980 implied a need for a more accurate centering of the lenses. An optical centering scheme, described earlier in this section, was developed using a combination of a laser and a lathe. KC1 lenses 710, 711, 715 and 721 were recentered using this technique. KRS-5 lenses 733, 734, 737 and 738 were also recentered on the same fixture. These recentered lenses were re-evaluated at NV&EOL in July 1980. The imager containing the two original germanium lenses and the ZnSe color corrector was also tested with the intention of verifying the entire system. The imager did perform within specifications with the original lenses. An interesting note on the performance of Martin Marietta large IR imagers delivered to NV&EOL is that they perform so closely to the diffraction limit that at times their MTF data exceeds the limit. The average MTF at 10.25 lp/mm for 14 different imagers was:

	On-Axis	Up	Down	Left	Right
Average MTF	77.11	73.91	74.05	75.5	75.52
Standard Dev.	1.90	3.10	4.24	2.84	2.21



Table 14. MTF Test Results for KCl Lens 715  
Paired with Four KRS-5 Lenses

KRS-5 Lens	MTF at 10 lp/mm
738	0.51
734	0.72
733	0.66
737 (spherical)	0.54

The MTF data on the contractor imager containing germanium and zinc selenide optics is listed below. Table 15 summarizes the data from measurements in which each KCl lens was paired with each KRS-5 lens to generate this comprehensive performance matrix.

LP/mm	MTF
0	100
1.282	38.41
2.564	94.94
3.84	91.45
5.128	88.71
6.4	85.9
7.692	82.82
8.974	79.88
10.26	77.51
11.54	75.16
12.82	72.6
14.	69.88
15.38	67.37
16.67	64.8
17.35	62.22
19.23	59.79

Thus, in different tests the highest values of MTF at 10 lp/mm were 0.72 and 0.71, below the specification of 0.74. In addition the value varied with lens orientation.

One question left unanswered by these tests was the effect of the color corrector being a forged lens as well as the asphere. A polished KCl lens was ordered from Janos. After receipt it was centered on the laser/lathe device and then tested in the imager at

Table 15. MTF at 10 lb/mm, EFL in mm and FD in mm of lens Combinations Tested After Recentrization

KCl Lens	Parameter	KRS-5 Lens				Nonasphere
		733	734	738	737	
710	MTF	0.69	0.69	0.47	0.58	
	EFL	67.81	67.52	68.03	67.74	
	FD	17.42	17.57	17.42	17.81	
715	MTF	0.72	0.68	0.71	0.5	0.55
	EFL	67.59	68.24	Not Measured	67.8	67.59
	FD	17.73	17.21 (12:00)	(9:00)	17.49	17.98
721	MTF	0.54	0.68	0.5	0.5	
	EFL	67.5	67.45	67.96	67.66	
	FD	17.46	17.55	17.24	17.84	

NV&OEL. It was assumed that this KCl lens would be "perfect". If the measured MTF values of the doublet were low, the fault could then be ascribed unambiguously to the KRS-5 lens.

The results (Table 16) show an inability to achieve on-axis MTF values higher than 0.68 at 10 lp/mm with the polished KCl lens.

The table shows the on-axis results when various KRS-5 lenses were tested in conjunction with the polished KCl lens, with lens 733 tested in two different orientations, as indicated.

To verify the data from the test runs of July 1980, aspheres 733 and 734 were also tested, along with the forged KCl 715 in January 1981. Also tested was KCl lens 711 that had been untested previously. It was paired with the asphere 734. Table 17 lists this last on-axis MTF data and shows that it consistently reaches the high 0.60s but also consistently is below the required range of 0.74 to 0.78 at 10 lp/mm.

#### ASPHERIC FORGING DIE

The disappointing performance of the doublets led to examination of possible sources which might degrade their optical performance. It was previously reported that interferometric examination of the aspheric die revealed a series of concentric zones<sup>(2)</sup>.

Table 16. On-Axis MTF Values Using Polished KCl Lens  
and Various KRS-5 Lenses

Frequency (lp/mm)	MTF Values		
	Lens 733 (9:00 orientation)	Lens 733 (12:00 orientation)	Lens 734
0	1.000	1.000	1.000
1.282	0.9694	0.9779	0.9501
2.563	0.9064	0.9294	0.8550
3.845	0.8560	0.8817	0.7992
5.126	0.8258	0.8430	0.7892
6.408	0.7906	0.8007	0.7677
7.690	0.7431	0.7525	0.7171
8.971	0.7011	0.7064	0.6729
10.25	0.6743	0.6691	0.6554
11.53	0.6474	0.6316	0.6362
12.82	0.6118	0.5898	0.5995
14.10	0.5773	0.5476	0.5667
15.38	0.5538	0.5134	0.5556
16.66	0.5307	0.4835	0.5442
17.94	0.5007	0.4550	0.5165
19.22	0.4729	0.4279	0.4900

Table 17. On-Axis MTF Values

Frequency (lp/mm)	Lenses 715 and 734 (12:00 orientation)	Lenses 715 and 734 (9:00 orientation)	Lenses 715 and 733 (9:00 orientation)	Lenses 715 and 733 (12:00 orientation)	Lenses 711 and 734
0	1.000	1.000	1.000	1.000	1.000
1.292	0.9727	0.9736	0.9750	0.9723	0.9747
2.563	0.9139	0.9163	0.9211	0.9153	0.9190
3.845	0.8613	0.8639	0.8718	0.8675	0.8666
5.126	0.8255	0.8288	0.8381	0.8361	0.8299
6.408	0.7879	0.7954	0.7988	0.7990	0.7940
7.690	0.7394	0.7537	0.7554	0.7507	0.7501
8.971	0.6895	0.7099	0.7157	0.7056	0.7041
10.25	0.6494	0.6723	0.6852	0.6740	0.6648
11.53	0.6149	0.6381	0.6536	0.6436	0.6289
12.82	0.5827	0.6050	0.6188	0.6082	0.5936
14.10	0.5561	0.5761	0.5848	0.5741	0.5620
15.38	0.5385	0.5548	0.5548	0.5481	0.5379
16.66	0.5219	0.5340	0.5231	0.5208	0.5152
17.94	0.5023	0.5102	0.5018	0.4887	0.4897
19.22	0.4840	0.4866	0.4793	0.4597	0.4645

We used the radii of each zone and estimated the inside and outside diameter of each zone in order to make a mathematical comparison with the aspheric equation. These results suggested the asphere was probably of acceptable accuracy. However, after the MTF performance of the doublet was measured, we decided to probe the die surface as carefully and accurately as the instruments in our facilities permitted.

This portion of the work was supported by contractor funding in a separate effort complementary to the contract-supported work. This work on probing the die surface and also the KRS-5 lens surface contours is described in Appendix E.

After probing, these results were again compared to the equation of the asphere. Figure E-5 in Appendix E is a graph of the sagittal difference between the die and the equation.

The curve shows the large departure of the die from the equation. The surface of the die is good to a radius of 0.3 inch but then departs rapidly from the equation. The deviation reaches almost 0.002 inch at the edge of the clear aperture. Fortunately two of the forgings (733 and 734) had radii longer than anticipated from the die radius. This accounts for their superior MTF performance.

Another consideration concerning the aspheric doublet performance was the fact that both lenses were forged. The previous forging success involved the KBr color corrector for substitution of the ZnSe lens. In an effort to separate the lens performance of each forged lens in the doublet, a single crystal KCl lens, polished to the exact dimensions of the optical design, was purchased from Janos Optical. The use of this lens, when substituted for a forged KCl, did not significantly change the measured MTF values. These observations were covered in the optical testing section. This result shows that the failure of the KRS-5/KCl doublet to meet the MTF specifications is attributable to the KRS-5 lenses.

#### IMPROVED REPLICATION

In the later stages of the program, after the measurement of low MTF values for the KRS-5 lenses, emphasis shifted to improving the ability to forge KRS-5 reproducibly, so that the surface of the lens would better match the surface of the die used for forging. This was the result of the measurements described in Appendix E, in which it is shown that there are significant non-reproducible departures of the lens surface figure from that of the die.

These efforts to increase the replication of the die surface shape on the KRS-5 surface have not been successful. Only a very limited number of experiments have been possible. The sample described in a previous report<sup>(2)</sup> referring to KRS-5 forging 714 was produced by halting the forging procedure before the total clear aperture of the lens was forged. This lens had good surface figure. It was felt that forging in such a way that the KRS-5 was not constrained by the sleeve could reduce stresses and improve surface replication.

Two approaches were attempted: forging KRS-5 samples of small area and machining the circumference of the first stage forging to prevent the second stage forging from reaching the alignment sleeve. It was considered that the alignment sleeve might contribute to internal stress and the ultimate degradation of the surface figure.

This work was done with flat dies to allow easy inspection of the forged surface on the interferometer. Neither approach yielded significantly improved surface replication.

A possible explanation for not improving the replication is associated with the frictional forces developed between the die surfaces and the deforming crystal. In general, the coefficient of expansion of a material and its Young's modulus are inversely related. That is, high expansion gives low stiffness. It appears that KRS-5 work hardens rapidly during deformation. As this effect increases, more and more elastic deformation is

produced. The frictional forces contribute to this problem also. When the deformation stress is relaxed, the elastic strain allows the lens to assume its equilibrium shape. This may be markedly different than the die surface figure. If the frictional forces could be reduced or the samples annealed prior to final deformation, some improvement might be noted. This is an area that should be explored further.

#### **FORGING ACCOMPLISHMENTS**

Despite the inability to forge a KRS-5/KCl doublet lens which would meet the MTF performance specifications, the forging portion of the program did lead to significant accomplishments.

Little previous experience with forging lenses with curved surfaces of moderately short radii had been gained prior to this program. Eight KCl lenses were forged. Six of these were considered acceptable for use as the color corrector for the doublet. Purchase of a single-crystal lens prepared by conventional methods verified this decision.

Prior to this program, the forging parameters associated with KRS-5 were unknown. Three typical orientations,  $\langle 100 \rangle$ ,  $\langle 110 \rangle$ , and  $\langle 111 \rangle$ , were examined. The  $\langle 111 \rangle$  orientation was found the most acceptable because of the deformation mode associated with this material. Five aspect ratios were examined. A single crystal 1.5-inch in diameter by 1.5-inch high produced the most predictable results. A problem was often encountered in that the starting crystal was not single. After deformation the divergent deformation characteristics of each area due to their respective orientations would become apparent. These forgings were unusable as lenses.

Thirty individual KRS-5 single crystals were forged in an attempt to produce either aspheric or spherical lenses. From these forgings three aspheres and two spherical lenses were tested for their MTF performance.

The cosmetic appearance of the forged lenses is good. The appearance of the KRS-5 lenses improved during the program because of improvements in the machining technique. Repeated handling, as during testing, tended to degrade the appearance of the lenses. They had no protective coating, only suitable transport containers.

## Section 14

### Conclusions and Recommendations

The work in this contract was performed in response to the need for moisture protection for halide optics. The successful development of KBr color corrector lenses which met the MTF specifications for the common modular FLIR raised expectations that halide optics could be qualified for FLIR procurements in the early 1980s. The halide lenses needed protective coatings in order to avoid degradation by water vapor in the atmosphere. No suitable moisture-protective coatings were available. Previous work on inorganic coatings had not led to an adequate protective coating. Organic polymeric coatings offered promise, but most organic coatings have high absorption in the 8 to 12 $\mu$ m spectral region.

This program was undertaken as a materials-based effort to determine the relevant properties of candidate coating materials for moisture protection. At the same time, it was hoped that the development could provide a coating which would meet the relevant environmental specifications and thus allow halide optics to be deployed in the common modular FLIR.

This latter hope has proved to be overly ambitious. During the course of the contract, expectations for the role of halide optics have changed. It became apparent that halide optics would not be included in the FLIR procurement. Accordingly, the program was redirected to emphasize the materials development aspects.

The coating development has in fact not succeeded in providing moisture protective coatings for KBr that satisfy the severe humidity conditions prescribed by the relevant Mil-Std-810B specifications. Moreover, the development of KRS-5 lenses as a possible alternative for germanium did not yield lenses which meet the FLIR's MTF specification. Nevertheless, the program has provided significant advances and accomplishments.

#### ACCOMPLISHMENTS

- Materials characterization; the program generated new knowledge about material properties, such as values of moisture permeability for a number of materials.
- Kinetics of moisture attack; definition of mechanisms by which water attacks a halide surface led to new insights for coating development.
- Development and optimization of a specific coating system ( $\text{As}_2\text{Se}_3/\text{PE}/\text{PPE}$ ) which offers:
  - Moderate moisture protection
  - Antireflective capabilities
  - Resistance to fungus growth

- Development of improved processes for deposition of organic coatings.
- Definition of the limits of moisture protection afforded for KBr by organic coatings thin enough to be transparent near  $10\mu\text{m}$
- Advanced optical testing capabilities, such as:
  - Two-wavelength holography.
  - Lateral shearing interferometry.
  - Development of transmission tests relevant to lens performance.
  - Correlation of lateral shearing interferograms with MTF performance.
  - A potential low-cost screening procedure usable in lens production.
- Definition of forging parameters relevant to KRS-5, the deformation characteristics of which were previously unknown.

To summarize the limits of coating protection available now, it appears possible to protect KBr to a relative humidity of 80% (the region where surface dissolution replaces chemisorption as the dominant mechanism of moisture-surface interaction), with a coating having at least  $5\mu\text{m}$  thickness of organic material. It is possible to protect KBr to a relative humidity of 95% with a coating having around  $12\mu\text{m}$  thickness of organic material, but such a coating would reduce the infrared transmission to a value which might not be acceptable for all applications.

#### RECOMMENDATIONS FOR FUTURE WORK

The introduction of low-cost halide optics into military systems should proceed slowly. There should be identified a specific system which can be utilized as a test vehicle for halide optics. The initial goal should be to deploy a small number of these systems, in order to gain field experience with halide optics and to gain broader acceptance for them. It is suggested that a candidate system make use of one of the advantages offered by halide optics, such as very broad spectral transmission.

Specifically, for near-term technical development, it is recommended that the following tasks be performed:

- Determine the thickness of organic coating necessary to satisfy the severe humidity requirement of Mil-Std-810B. Determine the transmission of a lens coated with this thickness, and evaluate potential applications for lenses with that value of transmission. Design a multilayer antireflective coating incorporating that total thickness of organic material.
- Evaluate potential applications for which the currently available coatings will provide adequate moisture protection.
- Evaluate potential applications for which the currently developed forging status of KRS-5, as a substitute for germanium, will provide adequate optical performance.



## References

1. R.H. Anderson, E. Bernal G., K.M. Leung, T.J. Moravec, F.M. Schmit and D. Wertman, Alkali Halide FLIR Lens Development, Semiannual Technical Report No. 2, on Contract DAAK70-77-C-0218, October 13, 1978.
2. R.H. Anderson, R.J. Stokes, K.M. Leung, T.J. Moravec, J.W. Lin, F.M. Schmit, J.F. Ready and E.L. Stelzer, Alkali Halide FLIR Lens Development, Semiannual Technical Report No. 1, on Contract MDA 903-80-C-0098, 31 May, 1980.
3. R.H. Anderson, et.al., Alkali Halide FLIR Lens Development, 1978-1979. (Unpublished Report).
4. M. Hucker, A. Oberlin and R. Holart, Bull. Soc. Frana. Mineral 90, 320 (1967).
5. Handbook of Chemistry and Physics, 54th Edition, p. E46, CRC Press, Cleveland, Ohio (1973-1974).

## Appendix A

### Ion Barrier Materials

This investigation of the effectiveness of various materials as ion barriers on alkali halides was performed under contractor funding in an effort complementary to the contract.

KCl substrates coated previously were tested to determine which coating procedure had imparted the best humidity protection to the substrates. These substrates were first potted in an aluminum ring using an epoxy similar to Torr-Seal.<sup>®</sup> To protect the uncoated side of these substrates during the humidity test plastic discs were sealed to the back of the aluminum rings with rubber gaskets. The potted substrates were then simultaneously submitted to a humidity test consisting of 40 minutes exposure to a 74°F environment with a relative humidity cycling between 72% and 92%. The five coating procedures for pinhole prevention tested were:

- Blowing the substrate with ionized nitrogen prior to placing the substrates under vacuum
- Deposition of two coating layers with cleaning of the first layer between the two depositions
- Electrical cleaning under vacuum by using an electrode mounted in vacuum
- Strip coat cleaning
- Mechanical defect-masking with thick layers of KCl followed by a TII layer blended into the KCl masking layer

The ratio of the transmission after and before the humidity test for the five substrates at a number of wavelengths is shown in Figure A-1. The curves for the substrates except for the one with the KCl masking layer show either a decrease in transmission that is either flat as a function of wavelength or a relatively structureless decrease with decreasing wavelength. The substrate with the KCl masking layer has a strong decrease in transmittance at  $3\mu\text{m}$ , a change in transmittance at  $6\mu\text{m}$  and a broad decrease in transmittance beyond  $10\mu\text{m}$ . Water has absorption bands at  $3\mu\text{m}$  and  $6\mu\text{m}$  and a broad decrease in transmittance starting in  $10\mu\text{m}$  and extending to longer wavelengths.

This indicates that water has been trapped beneath the TII film in the thick KCl masking layer. The fact that substrates with thick KCl masking layers with no protective coating became cloudy in less than a minute after being taken out of the vacuum system indicates that the masking layer has a large capacity for absorbing water.

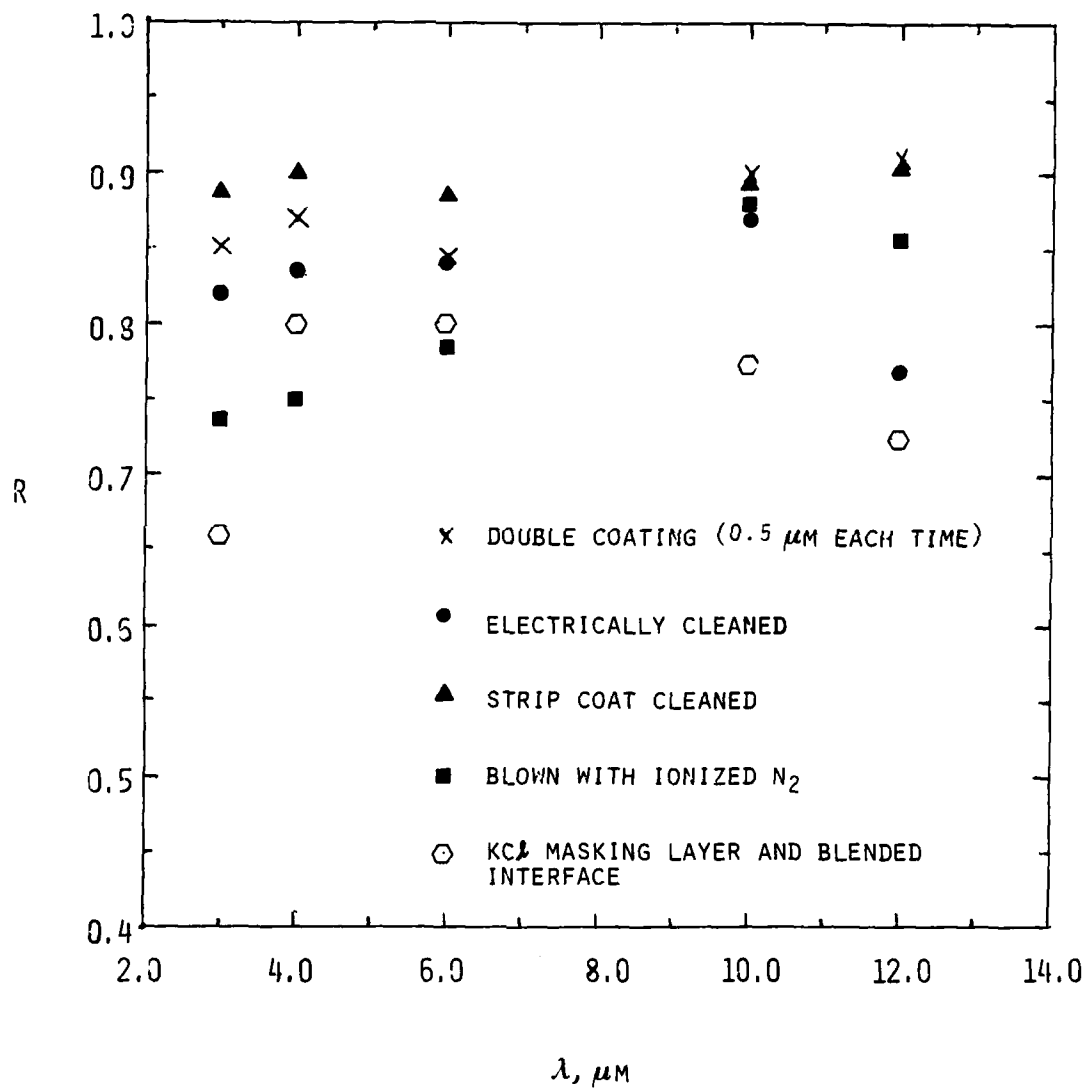


Figure A-1. The ratio  $R$ , of the transmission after and before a humidity test (40-minute exposure to 74°F, 72 to 92% RH) of five TII coated KCl substrates each coated by a different procedure.

After the humidity test the substrates were examined under a microscope and showed small square crystals on the TII outer surfaces. The crystals are assumed to be KCl substrate material. The substrate with the KCl masking layer showed dark inhomogeneous areas under the TII layer. The growth of KCl crystals on TII coated KCl substrates during humidity tests had been observed earlier. The mechanism by which the crystals are formed on the TII surface is assumed to be by ion transport of KCl through the TII film.

It appears that strip coat cleaning of the substrate offers the most promise for pinhole prevention in a coating operation designed to protect alkali-halide from a high-humidity environment. Even though the technique using a KCl masking layer and a blended interface TII coating yielded less visible damage as viewed under a microscope, the transmission results after the humidity test indicate that substrates treated this way give worse transmission than the strip-coat treated substrate.

The compatibility of the Kristal Koat® stripping material with a high vacuum environment was tested by measuring the weight loss of thin films of Kristal Koat® when they were exposed to a high vacuum for 3 hours after being dried for 1 hour. The Kristal Koat® films suffered a weight loss of less than 0.3% and still were able to be stripped after the test. The infrared transmittance of a KCl substrate before and after having Kristal Koat® applied and stripped was measured. None of the absorption bands associated with the infrared transmission spectra of a thin film of Kristal Koat® on a KCl substrate were found on the coated and stripped substrate. It seems feasible to use Kristal Koat® for stripping in a high vacuum environment. It would probably be advisable to make sure the coating was not heated in the vacuum environment before and after stripping. A strip coat material with the brand name Durepoly® was also evaluated. This material clouded the surface of the KCl substrates and was very difficult to strip off. It was therefore found to be an unsatisfactory strip coat material for KCl substrates.

Additional investigation of materials for an ion barrier focused on a search for visibly transparent materials that would make an ion-transport barrier on alkali-halide substrates. The materials tried were ZnS, SiO, CeF<sub>3</sub>, CaF<sub>2</sub> and As<sub>2</sub>Se<sub>3</sub>. TII was also included for comparison. The humidity passivation effectiveness of a thick KCl masking layer graded into a ZnS layer was also evaluated.

To make glue layers and graded interfaces, a vacuum system was fitted with dual evaporation sources with independent shutters. One source was a Radak crucible. The other was an e-beam hearth equipped with a carbon crucible and a molybdenum cap having a 0.1-inch-diameter hole in it. The e-beam was played across the molybdenum cap which radiantly heated the evaporant material, making the e-beam source similar to a conventional furnace source. The substrates were rotated during deposition of the films to help prevent columnar growth of the films. The substrates were not heated or cooled during deposition of the ion-barrier layers.

The first ion-barrier coating system tried was KCl masking layer ( $5\mu\text{m}$ ) graded into a ZnS final film. This coating had a cloudy appearance. After a humidity test, (40 minutes exposure at  $74^\circ\text{F}$  to relative humidity cycling between 72% and 92%) this substrate showed a severe decrease in transmission. All the other ion-barrier coatings were deposited using a glue layer with a graded interface. This glue layer was necessary for getting the ZnS to stick to the KCl substrates and was used for all the other materials so that the presence or absence of a glue layer was not a variable from one material to another. These films were tested by subjecting them to the same humidity test.

Typical damage to the ZnS coated substrate involves breakup of the coating into plates with KCl growing up at the edges of the plates. This type of damage appears in the SiO and  $\text{As}_2\text{Se}_3$  coated substrates with larger plates than for the ZnS coatings. Typical damage to the  $\text{CaF}_2$  and  $\text{CeF}_3$  involves breakup into much smaller pieces than the ZnS,  $\text{As}_2\text{Se}_3$  or SiO coatings.

The ratio of the transmittance of the six coated substrates after and before the humidity test is shown in Figure A-2. These substrates show a post-humidity test decrease in transmission which appears to be most likely due to scattering when one considers the damage visible under a microscope.

The scattering lowers the transmittance level independent of wavelength for the SiO and  $\text{As}_2\text{Se}_3$  coated substrates. The other substrates appear to scatter more at shorter wavelengths. The structure in the ZnS curve may be due to the formation of zinc sulfide monohydrate  $\text{ZnS}\cdot\text{H}_2\text{O}$  or zinc sulfide  $\text{ZnSO}_3\cdot 2\text{H}_2\text{O}$  during the humidity test.

The amorphous materials, SiO and  $\text{As}_2\text{Se}_3$ , showed the least degradation in transmission after the humidity test. However the SiO coating has a broad absorption band between  $8.5$  and  $12\mu\text{m}$ . The  $\text{As}_2\text{Se}_3$  gives the substrate a redish color even in thin layers ( $< 0.5\mu\text{m}$ ). Thicker layers of  $\text{As}_2\text{Se}_3$  become increasingly opaque especially at non-normal viewing angles. Nevertheless, it appeared that  $\text{As}_2\text{Se}_3$  offers the best chance for making an ion-barrier layer despite its undesirable optical properties in the visible.

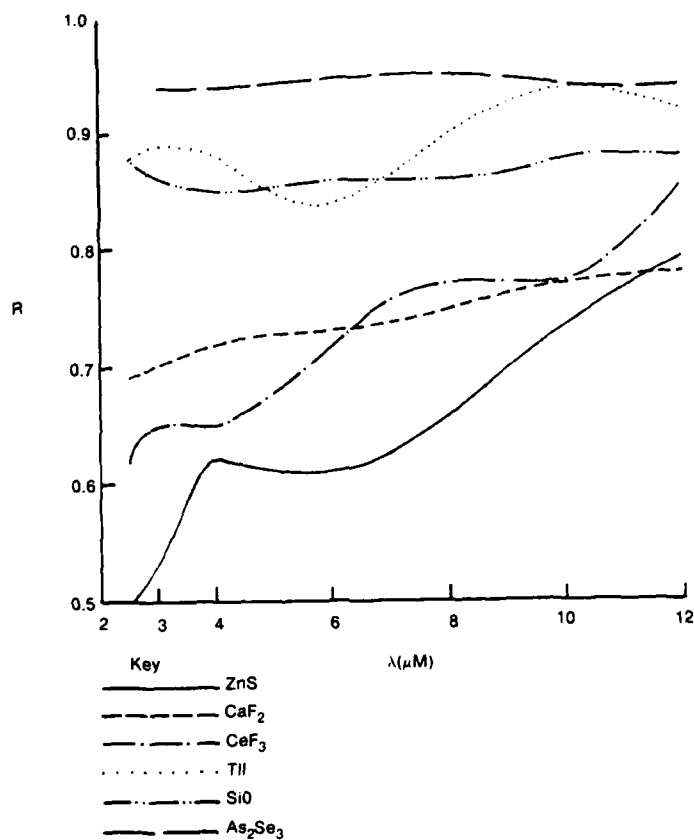


Figure A-2. The ratio  $R$  of the transmittance after and before a humidity test (40-minute exposure to 74°F, 72 to 92% RH) of six substrates coated with different ion barrier candidate materials.

## **Appendix B**

### **Antireflective Coating**

Because of the success of  $\text{As}_2\text{Se}_3$  as an ion barrier on alkali halide surfaces, an antireflective coating was using designed coating  $\text{As}_2\text{Se}_3$  as a high-index inner layer and an plasma polymerized ethane outer layer. Three antireflectance stacks were designed for  $10.6\mu\text{m}$ . The transmission of the coatings as a function of wavelength and the thicknesses used are shown in Figure B-1. The stacks may be modified by adding half-wave multiples of either as  $\text{As}_2\text{Se}_3$  or plasma polymerized ethane layers.

This coating design was performed under contractor funding in an effort complementary to the contract.

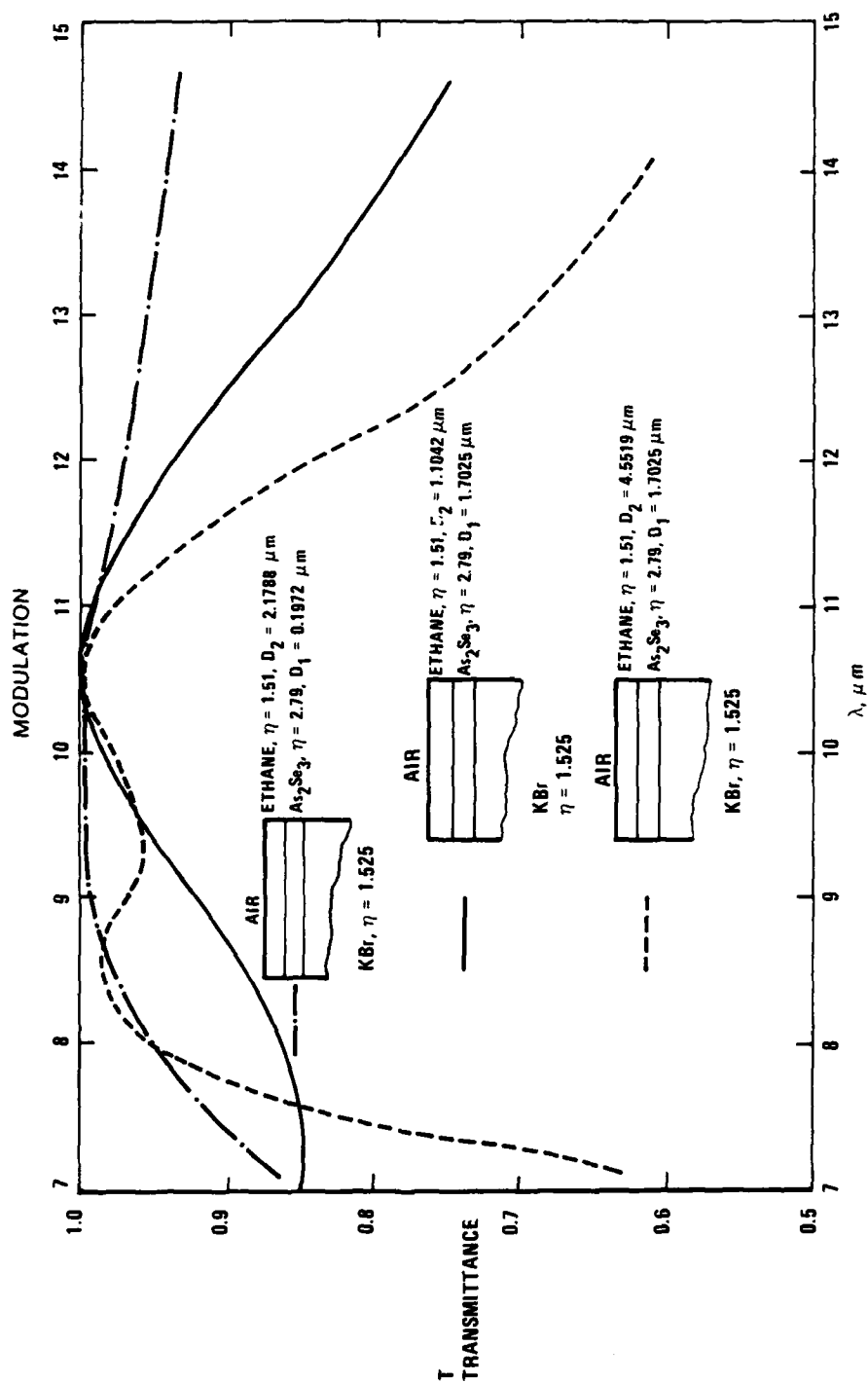


Figure B-1. The theoretical transmission curves of three antireflectance stacks on a KBr substrate. The stack with a  $4.5519 \mu\text{m}$  thick ethane layer differs from the stack with  $1.1042 \mu\text{m}$  ethane layer by the addition of a half-wave ( $10.6 \mu\text{m}$ ) layer of ethane.



## **Appendix C Fungus Test**

The report of Environ Laboratories, Inc., on fungus testing of coated KBr samples appears on the following pages.

ENVIRON LABORATORIES, INC.  
20 August 1981

ENGINEERING REPORT NO. 11352  
Page 1

Prepared for: HONEYWELL, INC.  
10701 Lyndale Avenue South  
Bloomington, Minnesota 55420

Subject: FUNGUS TEST

1. ABSTRACT

1.1 Object

Four potassium bromide lenses with a multi-layered protection coating and samples of the coating components, were subjected to a Fungus Susceptibility Test to determine if the protective coatings would support fungal growth or be degraded by the conditions associated with the test exposure.

1.2 Conclusions

No fungal growth was visually evident at the conclusion of the exposure on the lenses themselves or the samples of the protective coating components. Additionally, none of the samples appeared to be degraded by the high humidity associated with the exposure.

2. UNITS TESTED

Four coated potassium bromide lenses were subjected to a Fungus Test in accordance with MIL-STD-810B, Method 508, with exceptions as detailed below.

Samples of each component layer of the composite protective coating were applied to  $\frac{1}{2}$ "x $\frac{1}{2}$ " glass slides. These samples were also tested to ensure that each was resistant to fungal growth.

3. TEST REQUESTED

The test requested was the Fungus Test of MIL-STD-810B, Method 508. This calls for a 28-day exposure to conditions of 84  $\pm$  2.5°F with a minimum of 95% relative humidity in the presence of active fungal spores from five different organisms.

The control items employed to verify active spores and proper growing conditions were those specified in the Fungus Test of

3. TEST REQUESTED (Cont'd)

MIL-STD-810C, Method 508, Paragraphs 3.1.3 and 3.1.4. These controls were used because of their ready availability. Since MIL-STD-810C employs the same organisms as MIL-STD-810B a substitution of this type is valid.

4. INSTRUMENTATION, PROCEDURE AND RESULTS

4.1 Instrumentation

Environ Fungus Chamber, Environ No. F-4  
Petroff-Hauser Bacteria Counter  
Swift Compound Microscope, Model No. 645258  
International Clinical Centrifuge, Model CL  
Process (Temperature/Humidity) Controller, Research, Inc.,  
MicRicon Model VI-G  
Hellige pH Comparator, Model 605

4.2 Fungus Specimens Used

The fungus specimens used for the test were obtained from the American Type Culture Collection, 12301 Parklawn Drive, Rockville, Maryland. These were as follows:

<u>Fungi</u>	<u>ATCC No.</u>
Aspergillus niger	9642
Aspergillus flavus	9643
Aspergillus versicolor	11730
Penicillium funiculosum	11797
Chaetomium globosum	6205

4.3 Procedure

A composite suspension was made from the above specimens in accordance with MIL-STD-810B, using nutrient salts solution with a pH value of 6.2 when measured at room ambient conditions.

The test units and control items were placed in the fungus chamber, preconditioned, and sprayed with the composite suspension. This was accomplished on 7 July 1981. The test chamber was then maintained at a temperature of  $84 \pm 2.5^\circ\text{F}$  and a minimum relative humidity of 95 percent for 28 days. The potassium bromide lenses and control items were removed from the fungus chamber on 4 August 1981.

ENVIRON LABORATORIES, INC.  
20 August 1981

ENGINEERING REPORT NO. 11352  
Page 3

4. INSTRUMENTATION, PROCEDURE AND RESULTS (Cont'd)

4.4 Results

Visual inspection, upon completion of the Fungus Test, revealed no visible evidence of fungus growth on the test units.

The units were returned to Honeywell, Inc. for further evaluation.

## Appendix D

### Papers Resulting from Work on Lens Development

The following papers were presented at the Workshop on Optical Fabrication and Testing, September 22-23, 1980, at Sea Crest Hotel, N. Falmouth, Cape Cod, Mass., The workshop was sponsored by the Optical Society of America.

**Handling the Turning of Machinable Thallium Salts.** F.M. Schmidt and R.H. Anderson, Honeywell Corporate Material Sciences Center, 10701 Lyndale Avenue South, Bloomington, MN 55420.

A TII-ThBr compound known as KRS-5 is being investigated as a forgeable IR optical material. A novel technique for machining the KRS-5 is presented in which all the turnings are removed from the lathe without obscuring the operator's line of sight. The results are shown to be not only a safe lab but also a fine machining performance.

**Testing Forged Infrared Optics by Holographic Techniques.** K.M. Leung, F. Schmit, and R. Anderson, Honeywell Corporate Material Sciences Center, Bloomington, MN 55420.

During the early stages of fabrication of forged aspheric lenses, a significant difference can be found between the forged lens surface and the diamond-truned die. A unique holographic technique can be used to test the forged aspheric surface when the resulting interferograms are too complicated to analyze. The use of these tests on complex surfaces of forged infrared optics is described.

**Hot Forging the Infrared Lens: KBr.** F.M. Schmit, R.H. Anderson, K.M. Leung and R. Betsch, Honeywell Corporate Material Sciences Center, Bloomington, MN 55420.

A procedure is described in which a KBr single crystal is heated to 250°C in a helium atmosphere and pressed between spherical Pyrex dies. Orientation of the starting crystal, the die-crystal interface for each forging, temperature limits, pressure limits, ambient isostatic atmosphere, and optical tests of the final lens are discussed.

**Building the Lens Mount into the Lens.** F.M. Schmit and R.H. Anderson, Honeywell Corporate Material Sciences Center, Bloomington, MN 55420.

Forged optics can include a mounting flange on the periphery of a convex lens. We show that a lens with a flat annulus on both sides of the lens may be included in an experimental forging program.

**Forging an Aspheric Optical Element**, R.H. Anderson, F.M. Schmit, and K.M. Leung, Honeywell Corporate Material Sciences Center, Bloomington, MN 55420.

A meniscus lens of KRS-5 with an aspheric convex surface is being isostatically forged using a two-step forging process. The surface figures and optical performance of the forged aspheric lens are discussed.

## Appendix E

### Aspheric Profile Measurements

The work described in this appendix was supported by contractor internal funds and is complementary to the contract-supported work. It involves measurement of the surface profiles of the forged KRS-5 aspheric lenses and of the dies used for the forging.

Aspheric surface profiles can be measured interferometrically, although with a limited degree of precision when the reference wavefront from the interferometer is spherical and the aspheric surface to be tested departs significantly from a sphere. This appendix describes the method for a particular profilometer arrangement used to measure aspheric surfaces. Although the method involves contacting the surface being measured, it has proven to be more accurate than previous methods utilizing an interferometer.

The basic arrangement for the profilometer is shown in Figure E-1. A dial indicator probe with a finite contact radius is zeroed at some nominal contact point on the asphere. The probe is then withdrawn via a z-axis screw feed, translated over an increment  $\Delta y$  with a y-axis screw feed, and then repositioned by using the z-axis feed until contact is once again made with the surface and the dial indicator becomes zeroed again. Recording the (y, z) pairs across the surface will allow the surface profile sag to be obtained after appropriately correcting for the ball radius of the probe. These resulting sag values can then be fit to a surface profile equation which will determine the best fit surface coefficients, as well as removing any residual tilt and offset in the measurements. It is assumed that the measurements are taken along a meridian of the surface, although if there is a known offset from the center in or out of the plane of the measurements, this can easily be incorporated into the surface profile equations. It should also be noted that the practice of zeroing the dial indicator for each measurement repositions the probe at the same angle  $\theta$ , thus eliminating a considerable complication in the data reduction. Thus, one need only be concerned with the different point of contact on the probe ball in reducing the data.

The surface profile equation used in the optimization program which determines the best fit set of coefficients is given by

$$z = \frac{cy^2}{1 + [1 - (k+1)cy^2]^{1/2}} + dy^4 + ey^6 + fy^8 + gy^{10} + z_0 + Ty$$

where the coefficients to be determined are

- c = vertex curvature
- k = conic constant
- d,e,f,g = 4th-10th order deformations
- $z_0$  = axial origin offset
- T = linear tilt

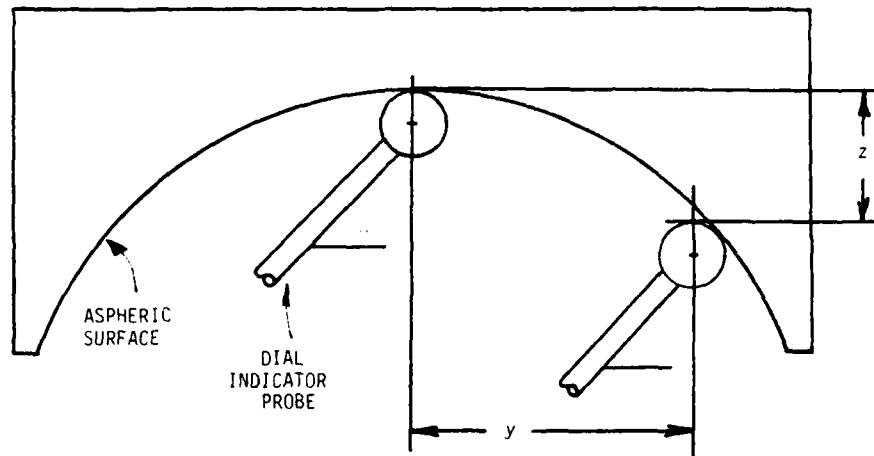


Figure E-1. Profilometer measurement schematic.

The origin offset and linear tilt terms are included for ease of transcribing the input data and to allow the removal of any constant offsets due to these terms. A more accurate surface profile results by being able to subtract off these latter two terms, and use only the rotationally symmetric surface coefficients in the description of the best fit surface profile.

The raw  $(y, z)$  pairs themselves do not represent the actual sag coordinates of the surface because the probe ball has a finite radius and will change its point of contact as the probe is translated across the surface. Thus, the  $z$  coordinates of the data pairs must be adjusted accordingly. Figure E-2 shows the probe contact geometry.

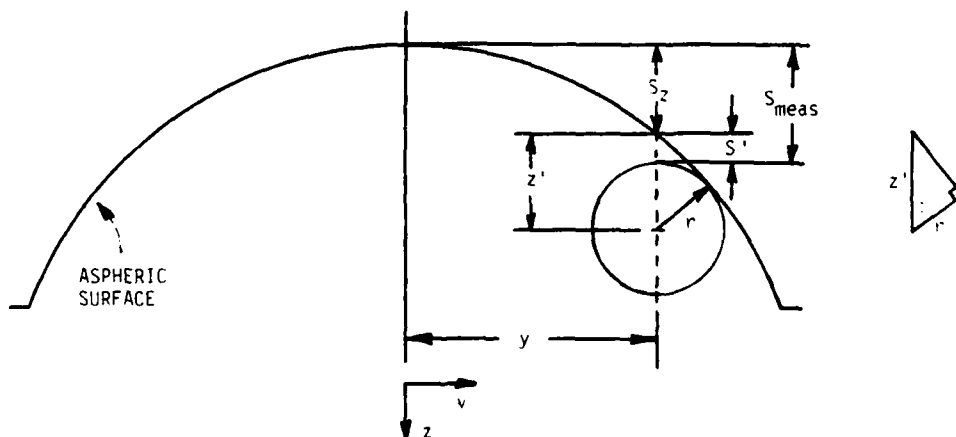


Figure E-2. Probe contact geometry.



To find the point of contact on the ball with the aspheric surface, the slope of the profile must be known. The measurement process produces the (y,z) pairs along the surface profile which allows the calculation of the slope

$$\tan \phi = \frac{dz}{dy} = \frac{z_i - z_{i-1}}{y_i - y_{i-1}}$$

The inset triangle of Figure E-2 shows that

$$z' = \frac{r}{\cos \phi}$$

$$s' = S_{\text{meas}} - S_z = z' - r$$

$$S_z = S_{\text{meas}} - S'$$

which reduces to

$$S_z = S_{\text{meas}} + r \left( 1 - \frac{1}{\cos \phi} \right) \quad \text{concave surface}$$

$$S_z = S_{\text{meas}} - r \left( 1 - \frac{1}{\cos \phi} \right) \quad \text{concave surface}$$

Thus, the measured sags for the surface ( $S_{\text{meas}}$ ) are corrected to the actual sags ( $S_z$ ) at the given y position, by the right hand side of the above equations. These corrected sags are then used as input to the optimization program, and the best fit profile coefficients are obtained.

As an example of the method, the following data is from measurements taken for the Bell and Howell diamond turned stainless steel die. Approximately 120 measured data points for this concave surface were used as input to the optimization program. The probe ball radius was a constant value = 0.0195 inch and the offset of the center of the profile from the edge of the die was 1.170 inch. After three iterations the program converged to the following solution for the coefficients:

$$\begin{aligned} c &= -0.28302 \quad (R = 1/c = -3.533) \\ k &= 0.23291 \\ d &= -0.78848\text{E-}2 \\ e &= 0.21123\text{E-}1 \\ f &= -0.21870\text{E-}1 \\ g &= 0.76742\text{E-}2 \\ z_o &= 0.19893 \\ T &= 0.30757\text{E-}3 \end{aligned}$$

Excluding the endpoints of the data, which were given weight one-tenth that of the rest of the data points, the maximum departure of the data points from the best fit profile given by the above coefficients was  $\pm 0.0003$  inch, and typically the departures were less than  $\pm 0.0001$  inch for over 85% of the data points. This indicates that the above coefficients adequately describe the actual die profile to the accuracy of the measuring instrument.

The axial offset term,  $z_0$ , represents the full aperture sag of the die, since the edge data points of the die were nominally defined as the zero reference. The tilt term,  $T$ , indicates a negligible tilt in the data (either in the die profile, or in the measurement process) amounting to 0.0003 in/in or 1 minute of arc.

It is interesting to compare the measured profile with the nominal profile as given to Bell and Howell. The nominal profile is described by the following coefficients:

$$\begin{aligned} c &= -0.281455 \quad (R = 1/c = 3.552962) \\ k &= 0.24 \\ d &= 0.29861\text{E-}3 \\ e &= -0.48796\text{E-}3 \\ f &= 0.83165\text{E-}4 \\ g &= 0 \end{aligned}$$

The difference between this nominal profile and the actual measured profile is given in Table E-1, and a plot of the results is shown in Figure E-3

Table E-1. Difference Between Nominal and Actual Die Profile

y	$\Delta\text{SAG} (\text{DIE}_{\text{nom}} - \text{DIE}_{\text{meas}})$
0.0	-0.000050
0.1	0.000010
0.2	0.000016
0.3	-0.000036
0.4	-0.000187
0.5	-0.000424
0.6	-0.000670
0.7	-0.000848
0.8	-0.000969
0.9	-0.001206
1.0	-0.001711
1.1	-0.001870

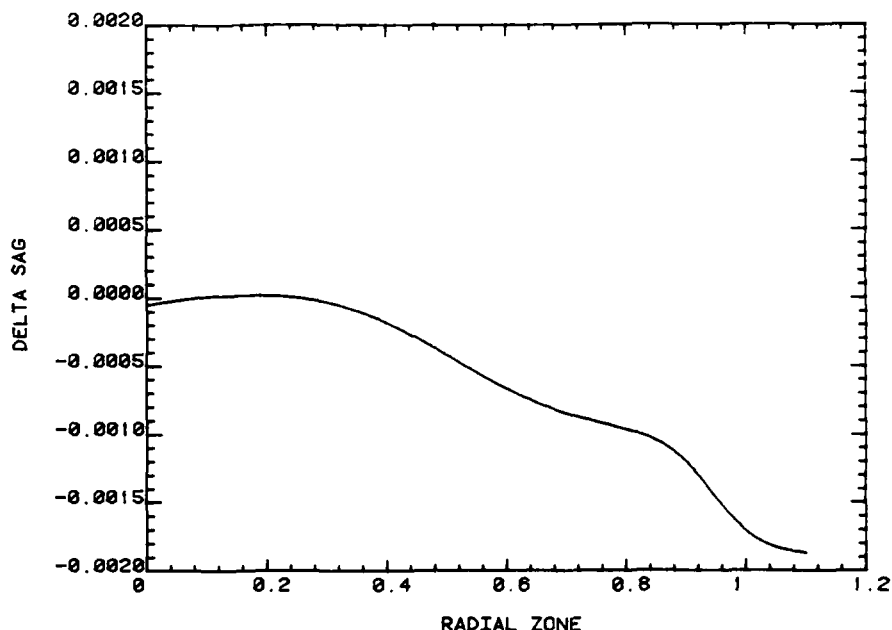


Figure E-3. Sagitta difference (Delta Sag) between nominal and measured die profile.

The results indicate a significant departure of the two curves, with the actual die profile having a stronger curvature (i.e. larger sag) than the nominal profile. The difference amounts to approximately 75 waves ( $0.6328\mu\text{m}$ ) at the edge of the die.

Several KRS-5 forged elements were also measured with this method, and a summary of the results for element number 733 are presented here. Thirty-three data points were corrected and fit with the optimization program, with the following profile resulting as the best fit asphere to the data:

$$\begin{aligned}
 c &= -0.27584 \\
 k &= 0.22580 \\
 d &= -0.28088\text{E-}1 \\
 2 &= 0.71246\text{E-}1 \\
 f &= -0.70206\text{E-}1 \\
 g &= 0.23438\text{E-}1 \\
 z_o &= 0.19978 \\
 T &= -0.28933\text{E-}2
 \end{aligned}$$

The maximum differences between the actual data points and this best fit profile were  $\pm 0.0005$ , while 70% of the data points were within  $\pm 0.0001$ ". The tilt is ten times greater for the forged element than the die, indicating a residual asymmetry in the KRS-5 profile after the forging process. The difference between the forged KRS-5 profile and that of the measured die is given in Table E-21 and a plot of the results is shown in Figure E-4.

Table E-2. Difference Between Surface of Die and Lens

y	$\Delta SAG$ ( $DIE_{meas} - KRS-5 \text{ No. } 733_{meas}$ )
0.0	0.000000
0.1	0.000015
0.2	0.000055
0.3	0.000108
0.4	0.000166
0.5	0.000236
0.6	0.000342
0.7	0.000517
0.8	0.000772
0.9	0.001062
1.0	0.001276
1.1	0.001299

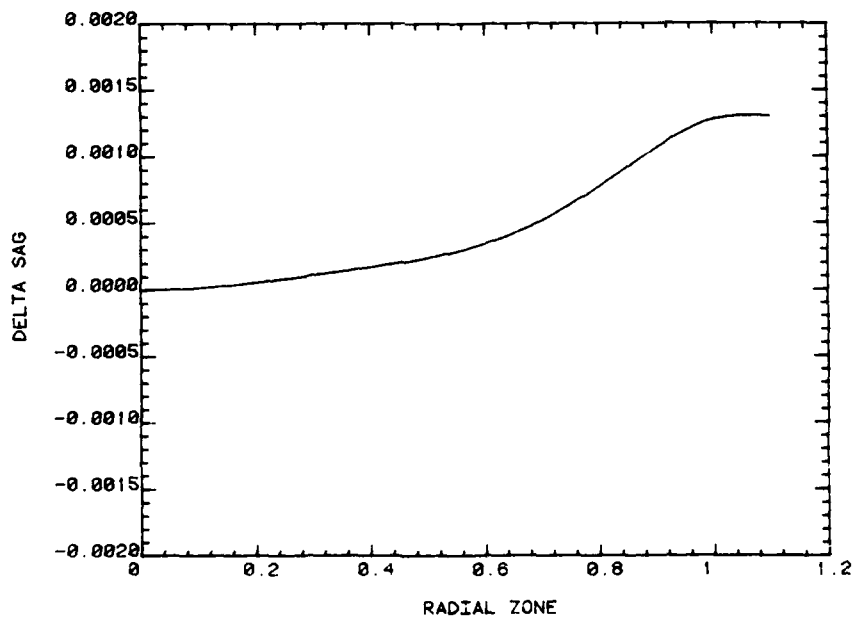


Figure E-4. Sagitta difference (Delta Sag) between KRS-5 733 and measured die profile.

The results indicate that the KRS-5 profile departs significantly from the die profile, amounting to 52 waves ( $0.6328\mu\text{m}$ ) at the edge. The KRS-5 lens is also less curved than the die, as indicated by the positive difference in sags.

A plot of the difference between nominal aspheric profile of the EOSC design, and the actual profile measured for 733 is shown in Figure E-5. Element 733 thus matches the nominal profile quite well over most of its clear aperture. The numerical results are tabulated in Table E-3.

Table E-3. Difference Between Nominal Profile and Actual Lens.

y	$\Delta\text{SAG KRS-5}$ (Nominal Design 733)
0.0	0.000000
0.1	-0.000003
0.2	-0.000012
0.3	-0.000027
0.4	-0.000046
0.5	-0.000067
0.6	-0.000084
0.7	-0.000087
0.8	-0.000064
0.9	0.000008
1.0	0.000154
1.1	0.000408

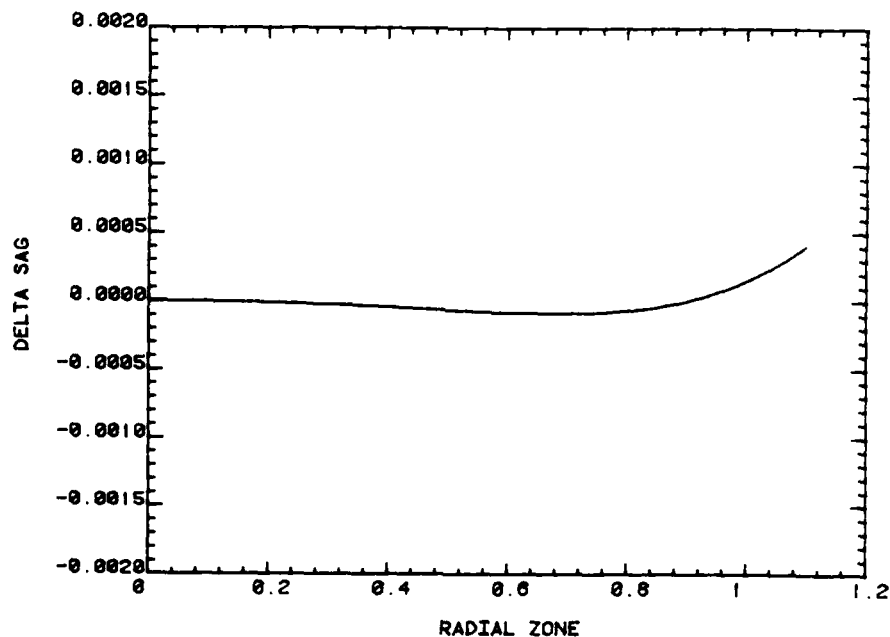


Figure E-5. Sagitta difference (Delta Sag) between nominal design and measured KRS-5 733 profile.